The Thesis Committee for Esmail Mohamed Khalil Eltahan
Certifies that this is the approved version of the following Thesis:

Uncertainty Quantification of Unconventional Reservoirs Using Assisted History Matching Methods

APPROVED BY
SUPERVISING COMMITTEE:

Kamy Sepehrnoori, Supervisor

Wei Yu

Uncertainty Quantification of Unconventional Reservoirs Using Assisted History Matching Methods

by

Esmail Mohamed Khalil Eltahan

Thesis

Presented to the Faculty of the Graduate School of

The University of Texas at Austin

in Partial Fulfillment

of the Requirements

for the Degree of

Master of Science in Engineering

The University of Texas at Austin

August 2019

Dedication

To my mother **Samia**, my father **Mohamed**, and my loving siblings.

Acknowledgements

I would like to express my deepest gratitude to Professor Kamy Sepehrnoori who I am honored to work under his supervision. Ever since I met him on my very first day in the Hildebrand department, he has been great guide and mentor. I thank him for guiding me through my research and providing endless motivation and support. I sincerely thank Dr Wei Yu for the time he spent in my training, reviewing my work and providing insightful feedback. I appreciate his motivational words that made me believe in my capabilities and yearn for more achievements.

I extend my thanks to my colleagues and friends Mauricio, Fabio, Reza, Sutthaporn, Bruno, Mehran, and Hamza. With them I had discussions that taught me a lot and helped me get through research obstacles. I sincerely appreciate the support provided by the members of the Reservoir Simulation Joint Industry Project (RSJIP). I specially acknowledge EP Energy for providing a high-performance computing unit that facilitated progress of my research. I appreciate the thoughtful comments and field knowledge I received from Erich Kerr and Jhon Hunter Drozd at EP Energy, and I cherish the discussions with Omer Alpak at Shell. These conversations sparked many topics and ideas explored in the thesis.

I am indebted to the Fulbright Commission in Egypt and the US Department of State for granting me the generous Fulbright scholarship. Without their trust and support, none of this would have been possible. I conclude the acknowledgements with honorable thankfulness to the soul of my fellow Fulbright student, roommate, and friend Hassan Abid, for his late-night tips and help in coding. May his soul rest in peace.

Abstract

Uncertainty Quantification of Unconventional Reservoirs Using Assisted History Matching Methods

Esmail Mohamed Khalil Eltahan, M.S.E

The University of Texas at Austin, 2019

Supervisor: Kamy Sepehrnoori

A hallmark of unconventional reservoirs is characterization uncertainty. Assisted History Matching (AHM) methods provide attractive means for uncertainty quantification (UQ), because they yield an ensemble of qualifying models instead of a single candidate. Here we integrate embedded discrete fracture model (EDFM), one of fractured-reservoirs modeling techniques, with a commercial AHM and optimization tool. We develop a new parameterization scheme that allows for altering individual properties of multiple wells or fracture groups. The reservoir is divided into three types of regions: formation matrix; EDFM fracture groups; and stimulated rock volume (SRV) around fracture groups. The method is developed in a sleek, stand-alone form and is composed of four main steps: (1) reading parameters exported by tool; (2) generating an EDFM instance; (3) running the instance on a simulator; and (4) calculating a pre-defined objective function.

We present two applications. First, we test the method on a hypothetical case with synthetic production data from two wells. Using 20 history-matching parameters, we compare the performance of five AHM algorithms. Two of which are based on Bayesian

approach, two are stochastic particle-swarm optimization (PSO), and one is commercial DECE algorithm. Performance is measured with metrics, such as solutions sample size, total simulation runs, marginal parameter posterior distributions, and distributions of estimated ultimate recovery (EUR). In the second application, we assess the effect of natural fractures on UQ of a single horizontal well in the middle Bakken. This is achieved by comparing four AHM scenarios with increasingly varying natural-fracture intensity.

Results of the first study show that, based on pre-set acceptance criteria, DECE fails to generate any satisfying solutions. Bayesian methods are noticeably superior to PSO, although PSO is capable to generate large number of solutions. PSO tends to be focused on narrow regions of the posteriors and seems to significantly underestimate uncertainty. Bayesian Algorithm I, a method with a proxy-based acceptance/rejection sampler, ranks first in efficiency but evidently underperforms in accuracy. Results from the second study reveal that, even though varying intensity of natural fractures cam significantly alter other model parameters, that appears not to have influence on UQ (or long-term production).

Table of Contents

List of Tables

List of Figures

BACKGROUND

Chapter 1: Introduction

The U.S. Energy Information Administration (EIA) estimated that in 2018, about 59 % of total US crude oil was produced directly from tight oil resources. Tight oil is a term describing oil accumulations in low-permeable shale, sandstone, and carbonate rock formations. Tight-oil production is chiefly backed by exploitation of shale formations, also known as unconventional reservoirs. The EIA projects further growth in the contribution of tight oil in the US crude oil production for years to come (see **Figure 1.1**). Recent technological advances in hydraulic fracturing and horizontal drilling largely enabled the growth. Access to vast low-permeability shale oil accumulations was made possible by creating conductive fracture networks, branching around a long horizontal well bore. These advances in production technology triggered an interest from the petroleum industry to thoroughly understand hydrocarbon recovery from tight, typically fractured, formations. As a consequence, reservoir simulation of fractured reservoirs has received an increasing attention. Some researchers focused on reinventing traditional modeling techniques to handle fractures. Others proposed new techniques particularly designed to fit the purpose.

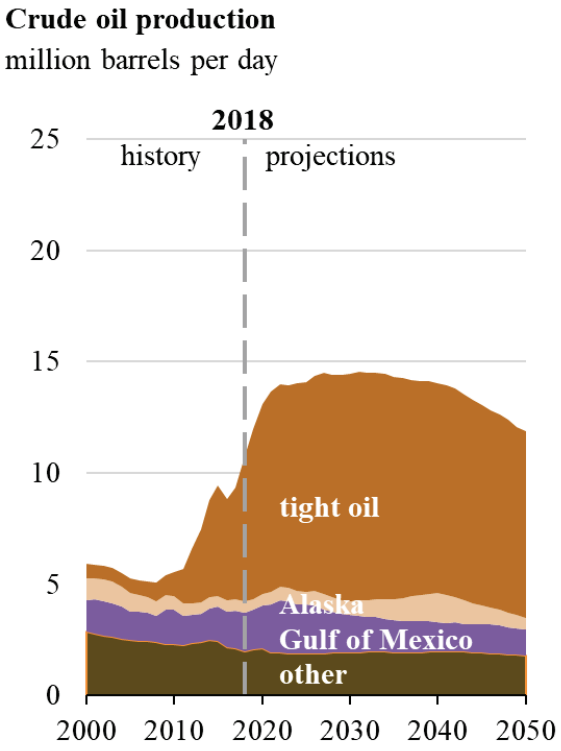

Figure 1.1 History and projections of the contribution of tight resources to total US crude oil production compared to other sources (from the EIA Annual Energy Outlook 2019)

Despite the achieved-research advances on numerous fronts, fluid recovery from unconventional reservoirs remains ill-understood. Numerous geomechanics studies are focused on studying the propagation and interactions of fractures in the subsurface. Nevertheless, accurate characterization of fracture networks in the field is still unachievable. Characterizing the fracture networks is an important step in building a representative numerical model and is crucial for subsequent reservoir management situations. Typically, the available information about the subsurface would be inadequate for the purpose of characterizing key reservoir elements. However, surface-production data

are routinely charted. One practical approach is the continuous conditioning an ill-informed reservoir-simulation model to the readily available data. The approach is routinely practiced in petroleum industry and is termed in the literature as history matching or data assimilation. Traditionally, an experienced engineer, in a trial-and-error fashion, would manually achieve history matching by fine-tuning some key model parameters. One drawback of manual history-matching is that it does not properly address uncertainty, as it often leads to producing one single solution.

Alternatively, the tedious task could be accomplished by systematic algorithms that are designed for the purpose, in a procedure known as assisted history matching (AHM). Not only does it save us the effort, AHM can also meaningfully quantify uncertainty. AHM methods are attractive as they usually produce an ensemble of equally qualified model candidates. Uncertainty, in production forecasts for instance, may be assessed by considering multiple forecasts of the ensemble individual models, as opposed to running one forecast from a single realization.

Embedded discrete fracture model (EDFM) is one class of reservoir simulation techniques, known for its efficiency and adaptability in handling fractured reservoirs. The efficiency stems from the fact that EDFM accounts for fluid-flow calculations associated with fractures in a virtual manner. In such manner, EDFM omits the computationally difficult process of placing fractures in the grid while maintaining an acceptable accuracy. Another advantage is that flow calculations are independent of phase or component. Thus, EDFM can be augmented to commercial reservoir simulators, as an external stand-alone processor, with no access requirement to the simulator's source code.

As part of this research, an in-house EDFM processor is applied in conjunction with a well-received AHM tool of a commercial simulation package. The integration allows full parameterization of natural and induced fractures in a form compatible with the third-party

software. By achieving so, we immediately enable applications beyond AHM, such as sensitivity, optimization, and Monte Carlo uncertainty-assessment studies. Inspired by real field scenarios, we adopt a modeling scheme that handles multiple wells and consists of three primary zones. In addition to the formation-matrix zone, we define distinct fracture and SRV zones around each well.

In this thesis, we develop a general-purpose optimization and AHM method for unconventional reservoirs. The thesis consists of six chapters and is arranged as follows.

In Chapter 2, we extend on the background of the work presented in the thesis. We thoroughly review the current literature on relevant topics, such as, numerical simulation of unconventional reservoirs, assisted history-matching methods, and multi-phase flow in unconventional reservoirs and its implication on the choice of relative permeability. The chapter concludes with an outline of the motives behind the work developed and described in the thesis.

Chapter 3 includes an in-detail description of the main components of the general-purpose optimization and AHM method. We introduce a fracture-design template that is intended to fit typical field cases and develop a new scheme for allocating stimulated rock volume (SRV). Later in the chapter, we highlight commercial AHM algorithms available for us to implement in practical problems.

In Chapter 4, we present a hypothetical field case with the purpose of testing the method's capabilities. The choice of generating synthetic data, rather than using real data, allows for controlling some factors that would have been otherwise uncertain in a typical field setting. The hypothetical model also serves as a reference solution for meaningful comparison of five AHM algorithms. Of special interest is one Bayesian algorithm with a proxy-based sampler. Using this method, the chapter includes an investigation of the effect of varying the history-matching period to the performance of AHM.

Chapter 5 takes the method to a real field case in the middle Bakken. The purpose of the chapter is to assess the effect of including natural fractures in the integrity of reservoir models. The effect is studied by comparing different scenarios with varying natural-fracture intensity. After achieving AHM, conclusions are drawn by comparing the ensembles of solutions obtained from each scenario.

Finally, in Chapter 6, we summarize key findings from the work. We list the limitations of the method and attempt to make recommendations for practical problems. We conclude by proposing some ideas for potential development motivated by this thesis.

Chapter 2: Literature Review

The purpose of this chapter is to review the current literature on numerical simulation of unconventional reservoirs (URs); assisted history-matching methods and their applications in URs; and multi-phase flow in URs and its implication on the choice of relative permeability. After a comprehensive survey, we conclude the chapter with outlining the motivation behind the work developed and described in the thesis.

2.1 Uncertainty In Unconventional Reservoirs

Improved hydraulic-fracturing treatments coupled with horizontal drilling technology made it possible for large-scale development of URs over the past decade (Cipolla et al. 2010). Developing methods with the capability to evaluate reservoir performance and predict estimated ultimate recovery (EUR) has been challenging. The complexity of fracture networks, often created by multi-stage stimulation techniques, makes it difficult to track fracture geometry or measure fracture conductivity. In addition, conventional decline rate analysis becomes difficult because of the complicated fluid flow behavior. Unlike conventional reservoirs, low-permeability (less than 0.1 md) URs typically exhibit prolonged period of transient flow (Luo et al. 2011). Therefore, the industry often relies on reservoir simulation as a preferable tool for predicting URs performance (Cipolla et al. 2010).

With the uncertainty inherent in URs, building representative and reliable reservoir models becomes challenging. Consequently, it is difficult to assess or quantify the amount of damage incurred to the formation by the fracture fluid after injection and shut-in periods. The invasion of water into rock matrix changes fluid-saturation profiles, which largely affect multi-phase flow. Another reason for the uncertainty is that fluid-flow, laboratory

experiments are infrequently conducted for URs. At a nanodarcy-scale permeability, conventional, core-flow tests and mercury-injection experiments are difficult and unreliable (Bostrom et al. 2014).

2.2 FRACTURE MODELING IN RESERVOIR SIMULATION

Different approaches have been proposed to simulate URs. Dual continuum models were independently developed by Kazemi et al. (1976) and Rossen (1977) to simulate naturally fractured reservoirs (NFRs). Inspired by these early developments, the same concept was extended to model URs (Ding et al. 2006; Du et al. 2010; Gong et al. 2008). In dual continuum models, fracture networks are approximated into a representative dual-porosity dual-permeability (DPDK) model. DPDK approaches generally assume homogeneous distribution of fractures, and hence, in many cases, fail to adequately describe fracture networks (Li et al. 2011; Moinfar et al. 2011). Cipolla et al. (2010) reported that explicit discretization of reservoir elements, such as matrix blocks and network fractures, most accurately describes URs. Although more rigorous than the available alternatives, discrete fracture models are still impractical for field scale applications because of their relatively large CPU time requirements (Yang et al. 2018).

Local grid refinement (LGR) models have been postulated to increase computational efficiency (Cipolla et al. 2010; Luo et al. 2011; Sun et al. 2014; Wantawin et al. 2017; Yu and Sepehrnoori 2018). In such models, an increasing number of grids around fractures results in increasing resolution of reservoir properties but also significantly increases computation time. Moreover, although dual-permeability, logarithmically spaced (DK-LS-LGR) models provide accurate-enough representation for reservoir modeling, they usually require fractures to align with the orientation of grid

(Yang et al. 2018). This is particularly limiting in the case of complex induced or natural fractures that may not necessarily be aligned in the direction of grid.

2.2.1 Embedded Discrete Fracture Model (EDFM)

Moinfar et al. (2014) introduced a more rigorous 3D embedded discrete fracture model (EDFM), which can handle fractures with arbitrary shapes and orientations. Implementing EDFM in commercial finite-difference reservoir simulators in a non-intrusive manner provides satisfactory accuracy at a considerably lower computational cost (Xu et al. 2017a, 2017b, 2018). Furthermore, EDFM is capable of handling complex fracture geometry with adequate efficiency.

As indicated earlier, discrete fracture modeling (DFM) is by far the most accurate method to simulate fluid flow in fractured reservoirs. This approach has not been widely utilized for field-scale applications. The large accuracy that DFM provides typically comes at a large computational cost. Handling discrete reservoir elements often requires some sort of unstructured gridding e.g., perpendicular bisector (PEBI) gridding. Not only laborious, such meshing techniques are but also rather inflexible. This disadvantage severely limits further applications such as uncertainty quantification and history-matching studies.

EDFM describes fractures as discrete elements while maintaining an orthogonally structured grid. EDFM treatment is similar, in concept, to dual-continuum methods. This treatment portrays each control volume, defined by the intersection of a fracture with a gridblock, as a new fracture cell. This fracture cell will then connect to the cells corresponding to intersecting matrix and fractures through non-neighboring connections (NNCs). These NNCs are created such that the simulator can account for three new fluid-flow interfaces: between matrix and a fracture segment; between two intersecting fracture segments; and between two segments of an individual fracture.

New cells designated for fractures and their accompanying connections are incrementally added in the computation domain. This is visually illustrated in **Figure 2.1**. Such arrangement enables flow interactions between cells that may not be necessarily connected in the physical domain while maintaining a structured grid. In addition to the NNCs discussed above, flow between a fracture and an intersecting well is governed by an effective well index that resembles Peaceman's work (1978). The calculated connection factors and indices depend only on the geometry and conductivity of rock matrix and fractures. In other words, the NNCs are independent of phases or components, allowing EDFM to be non-intrusive method that can be implemented in any connection-based, finite-difference reservoir simulator.

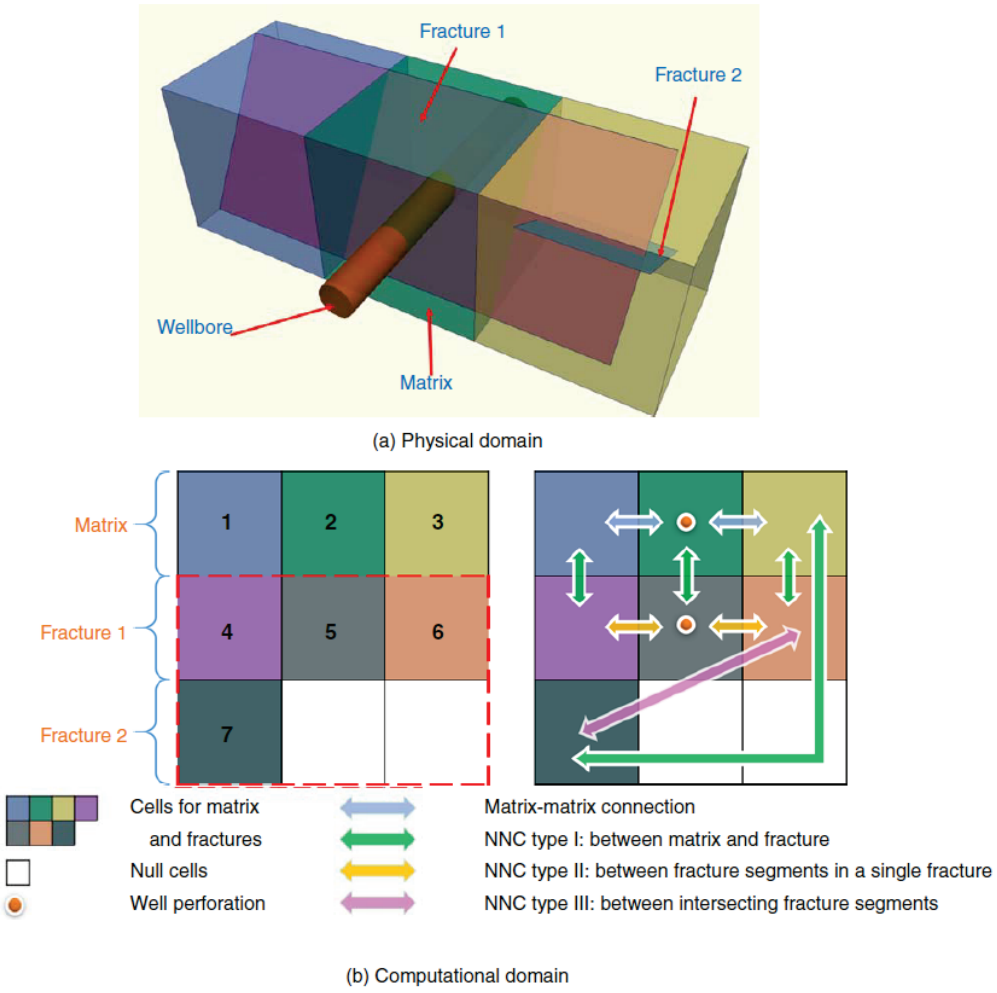

Figure 2.1 Illustration of cells and connections made in EDFM: (a) a simple case of 3 gridblocks that include a wellblock and 2 intersecting fractures, and (b) the corresponding cells and connections established in the computational domain (After Xu et al. 2017a).

Characterizing the dynamic behavior of natural fractures and hydraulically induced fractures is a critical component when optimizing well development, such as when analyzing well communication, optimal well or cluster spacing, or the impacts of the existing fracture framework. For this reason, EDFM is often utilized for its proven ability

to efficiently describe fluid flow and clearly indicate reserve distribution in URs where these uncertain fracture conditions exist. EDFM has been applied to model complicated field-case problems such as inter-well fracture interference (Fiallos et al. 2019a, 2019b) and CO_2 Huff-n-Puff (Yu et al. 2019).

2.3 ASSISTED HISTORY MATCHING (AHM)

History matching and uncertainty quantification are key components in reservoir simulation. They are essential components that normally proceed any main decision-making activities such as reservoir management, production forecasting and economic assessment. History matching involves the continuous updating of a current model, which is constructed based on prior information, to match observations, such as production history or time-lapse seismic. Conventionally, such a task would be delegated to an experienced engineer who would try numerous manual runs. For each run, the engineer alters some key model parameters in an attempt to reduce the misfit between simulation results after adjusting a few model parameters. This trial-and-error task comes to an end only when a tuned model achieves satisfactory match to observed history.

Over the past two decades, assisted history matching (AHM) has been picking up attention as an attractive alternative for conventional manual history matching (Oliver and Chen 2011). History matching is almost always a non-linear inverse problem that should have many non-unique solutions. In addition to being tedious, manual history matching leads to a single solution that does not properly address that uncertainty (Tavassoli et al. 2004). These limitations gave rise to employing computational power to assist in finding an ensemble of representative models. Predicting performance of the obtained ensemble allows for meaningful quantification of uncertainty.

Many sampling algorithms have been proposed in the literature to solve the problem and many are still under development. Methods can be based on various classes of algorithms, such as gradient-based optimization, stochastic and evolutionary algorithms. Given the problem-specific nature of history matching, each sampling algorithm will have its own limitation. The limitation often encountered is unaffordable computations required for running prohibitively large number of simulations. For that reason, many efforts are focused on minimizing the number of required simulations, for example by introducing design of experiment techniques; replacing simulations with streamlines; supporting sampling with proxies; or using ensemble Kalman filtering (Araujo et al., 2019). The interested reader may find a comprehensive review of AHM methods in Oliver and Chen (2011).

2.3.1 AHM Sampling Methods

Traditionally, AHM algorithms often employed a gradient-based optimization approach to minimize the objective function (see, e.g., Gomez et al. 2001; and Ding 2011). New distributed Gauss-Newton (DGN) methods were developed in conjunction with the increasing accessibility of parallel computing (Gao et al. 2016; Gao et al. 2018).

Derivative-free approaches gained popularity to achieve history matching. Stochastic techniques, which employ a random element in the search, have been applied in the literature for history-matching problems. These methods include: genetic algorithms (e.g., Romero et al. 2000; Carter and Ballester 2004); ant colony optimization algorithms (e.g., Razavi and Jalali-Farahani 2008; Hajizadeh et al. 2009a); differential evolution algorithms (e.g., Hajizadeh et al. 2009b; Hamdi et al. 2015); particle-swarm optimization (e.g., Mohamed et al. 2010; Vazquez et al. 2015); and the neighborhood algorithm (e.g., Christie et al. 2002; Subbey et al. 2004). The use of ensemble Kalman filter (EnKF) for

history-matching problems increased in popularity because of its simple implementation and computational efficiency. A comprehensive review on EnKF applications in reservoir simulation is available in Aanonsen et al. (2009).

Many of the methods mentioned above are attractive because they produce multiple history-matched models. A wide range of solutions is one meaningful way of quantifying uncertainty. However, there remains doubt whether the obtained sample accurately characterizes the underlying "true" uncertainty. In other words, the obtained sample of solutions might not correctly describe the posterior probability density function (PDF).

Bayesian statistics is a straightforward approach of describing and quantifying uncertainty. Baye's theorem is a statistical rule that describes probability based on prior information. History-matching inverse problems can be formulated in the Bayesian form

$$P(\boldsymbol{d}|\theta, M) \times P(\theta|M) = P(\theta|\boldsymbol{d}, M) \times P(\boldsymbol{d}|M)$$

$$likelihood \times prior = posterior \times evidence$$

where P denotes probability density, $\boldsymbol{d}$ is a vector of measured data, θ is a vector of uncertain parameters, and M is the basic model with fixed properties and parameters. The objective of a Bayesian-inference AHM method is to compute the PDF for the parameters exactly or approximately based on the available data and prior information (Tarantola 2005). In this approach, uncertainty characterization is achieved by sampling from the posterior (PDF) of model parameters.

If measurement and modelling errors are assumed to follow a multi-variate Gaussian distribution, the Bayesian formulation of the posterior PDF can be written as (Ma et al. 2008, Slotte and Smorgrav 2008):

$$p(\theta|\boldsymbol{d}) = c\, p(\theta) \exp\big(-F(\theta)\big)$$

where θ is an n-dimensional vector that contains all uncertain parameters, $\boldsymbol{d}$ is the measured data, $p(\theta|\boldsymbol{d})$ is the posterior PDF for the model given data, c is an unknown

constant, $p(\theta)$ is the prior PDF, and $F(\theta)$ is the objective function, may be defined by the simplified least-squares form:

$$F(\theta) = \frac{1}{2}\sum_{\mathrm{i,j}} \left(\frac{d_{i,j}^{obs} - d_{i,j}^{sim}(\theta)}{\sigma_{i,j}} \right)^2$$

where $d_{i,j}^{obs}$ is an element of an observation-data vector $\boldsymbol{d}$ for a data type i at time j, $d_{i,j}^{sim}(\theta)$ is the corresponding simulation output, and $\sigma_{i,j}$ is the standard deviation of uncorrelated data errors.

The randomized maximum likelihood (RML) is a method proposed by Oliver (1996) to sample from the posterior. By definition, RML is proven to accurately sample the posterior when the relationship between the parameters and the likelihood is linear. However, since a non-linear relationship prevails in many practical problems, efforts have been made to improve RML sampling for non-linear problems (e.g., Stordal and Nævdal 2018).

Markov Chain Monte Carlo (MCMC) is a class of algorithms designed to create samples form a target distribution. The sample space is exploited by Markov chains with equilibrium distribution equals a target function. These Markov chains start at some random initial points, and then they take random steps, or "walks", governed by some probabilistic rules. As the number of walks increases, a closer match is achieved between the obtained and the desired distributions. MCMC was introduced by Metropolis et al. (1953). Hastings (1970) refined the modest Metropolis algorithm and introduced the Metropolis–Hastings MCMC algorithm, a variant that has been adopted in numerous applications since. Other variations of MCMC sampling algorithms have emerged. The list includes Gibbs sampling, slice sampling, multiple-try Metropolis, reversible-jump sampling and Hamiltonian MCMC.

Standard MCMC algorithms are theoretically guaranteed to converge to accurate PDF sampling conditional to production data (Ripley 1987). However, convergence of an MCMC algorithm typically requires large number of iterations (in the order of hundreds of thousands or millions of iterations for high-dimension inverse problems). **Figure 2.2** shows an example of MCMC convergence as the number of iterations increases. For each iteration, a forward reservoir simulation is required to calculate the likelihood exactly. Therefore, for typical reservoir simulation problems, standard implementations of MCMC are often infeasible.

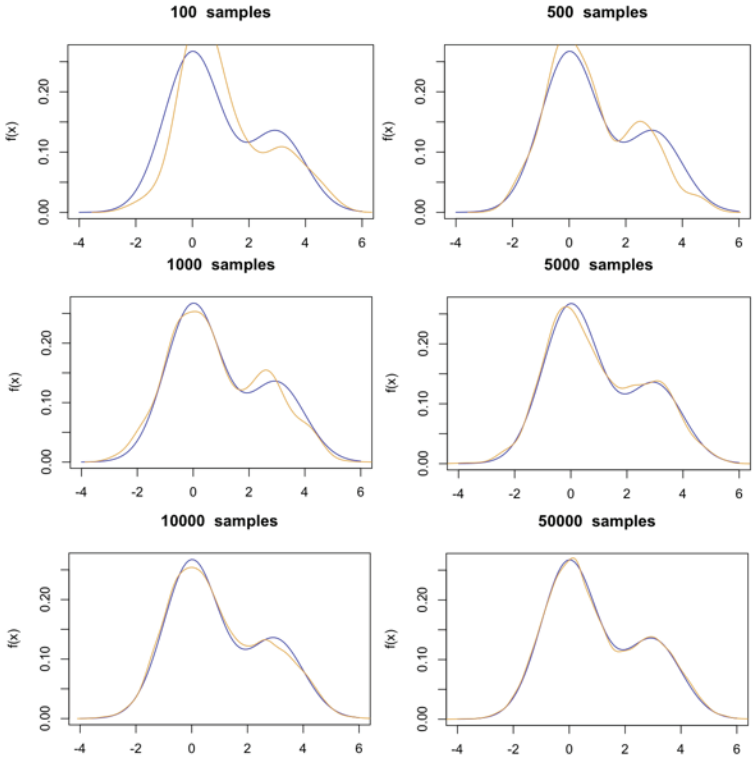

Figure 2.2 Example of the convergence of the Metropolis-Hastings algorithm. MCMC distribution is shown in blue in an attempt to sample the orange distribution.

To overcome the limitation of MCMC computational requirement, significant research has been made in an effort to minimize the number of expensive simulations. Maucec et al. (2007) implemented fast streamline simulation to replace the slower full-scale simulations. Another approach is using two steps in each iteration: in the first step, a fast simulation for a coarse-grid model is run; and in the second step, a fine-grid simulation is only run if the coarse-grid results satisfy certain criteria (e.g., Ma et al. 2008). Emerick and Reynolds (2012) combined EnKF with MCMC to obtain a relatively efficient sampling algorithm. Other researchers have been looking into assisting the algorithms with some kind of a proxy that approximates either the likelihood or the posterior. Wantawin et al.

(2017a, 2017b) combined a polynomial-model proxy with MCMC to perform history matching for shale gas wells. Yu et al. (2018) and Tripoppoom et al. (2019) presented applications of a method that combines k-nearest neighbor (KNN) proxy with MCMC. Dachanuwattana et al. (2019) made a comparison of polynomial-, KNN- and kriging-based proxies. They found that kriging is relatively more predictive although computationally most expensive. For that reason, they recommended the use of KNN as it presents a balance between accuracy and efficiency.

Neural networks (NN) could be promising solutions to approximate the non-linear relationship between the likelihood and the parameters. Although not many, there are some published applications of NN in Bayesian-inference methods. Yang et al. (2015) introduced a NN proxy that consists of a fast radial-basis function (RBF). Based on a Proxy-based Acceptance/Rejection (PAR) criterion, model states are either accepted or rejected. Before performing forward simulations for a possible model, an approximation of its posterior is first estimated by a trained NN proxy. Simulations are only run for those model candidates that satisfy the acceptance criteria.

Another type of robust Bayesian-inference methods is nested sampling (Skilling 2004). In nested sampling, the goal of the sampling algorithm is to calculate the evidence, also known as the marginal likelihood. In such algorithms, the posterior samples are obtained as a secondary product of the evidence calculation. Ramirez et al. (2017) successfully applied MultiNest, a variant of nested sampling, to reservoir simulation. Araujo et al. (2019) demonstrated that MultiNest is nearly as robust as MCMC to accurately sample the posterior. In their benchmarking study, they showed that MultiNest also requires large number of simulation-runs to fully converge. Still that number is far lower than what MCMC requires. Hence, MultiNest is more attractive for practical

application, particularly to small-scale simple reservoir models or when high-performance parallel computing is available.

2.3.2 AHM in Unconventional Reservoirs

Although EDFM is regarded in the literature as one of the most robust modeling methods because of its efficiency and flexibility when incorporating fractures, the EDFM integration still requires significant trail-and-error time to perform manual history matching and subsequent forecast or management of field reservoirs.

Most field-scale models involve large uncertainty in geological characterization and fracture geometry. The larger the number of uncertain parameters, the more difficult it is to perform manual history matching. Manual history matching will often result in a less-than-optimal single solution disregarding the non-uniqueness of all the viable solutions. AHM in URs has been performed using LGR models using proxy-based techniques or using time-consuming simulation-based techniques (Wantawin et al. 2017a, 2017b). In these LGR models, uncertain parameters such as fracture half-length and fracture height may only vary at a discrete level that is often dependent on grid size. In contrast, in the case of EDFM, those parameters can vary at a continuous level within a pre-defined range. For this reason, and since EDFM models are noticeably more efficient and flexible than LGR models, there is an obvious benefit for AHM using EDFM.

EDFM has been applied in an in-house AHM workflow (Dachanuwattana et al. 2018a, 2018b; Yu et al. 2018; Tripoppoom et al. 2019). Eltahan et al. (2019) made integration between EDFM and commercial algorithms available in third-party simulation packages, where full parameterization on the natural and induced fractures can be possible. By achieving such integration, we immediately enable applications beyond AHM, such as sensitivity, optimization, and Monte Carlo uncertainty-assessment studies.

2.4 MULTI-PHASE FLOW INSIDE AND AROUND PROPPED FRACTURES

Achieving a good history match does not guarantee reliable future predictions. Therefore, the more realistic and detailed the model is, the more reliable it becomes. For simulating multi-phase flow, a model must incorporate water-saturation profiles that are representative of the initial production condition. In addition, the relative permeability models selected for the model are crucial for multi-phase production-history matching.

Simulating multi-phase fluid flow in URs requires an accurate realization of relative permeability models, both in matrix and fractures. Measurement of permeability for the small-permeability shales is an experimentally challenging task. Moreover, typical shale reservoirs exhibit large degree of heterogeneity and contain both hydrophilic and hydrophobic pores (Bostrom et al. 2014). Upscaling the experimental findings to reservoir-scale models is challenging simply because the core plug-scale samples may not be representative of the reservoir scale. A core-plug sample may fail to comprise elements, such as heterogeneity, mixed-wetting behavior and the presence of micro-fractures.

2.4.1 Water Blocks in Tight Formations

The amount of water recovered from production after a hydraulic fracturing treatment is usually smaller than the total amount of water injected (Longoria et al. 2017). The remaining portion must be either trapped within the complex fracture network or leaked off to the adjacent matrix. Trapping could occur in secondary fractures after losing connection with the main fracture networks (Fan et al. 2010). Inside the main fractures, water could be bypassed by the favorable mobility of hydrocarbons or gravity segregation (Parmar et al. 2014; Agrawal and Sharma 2013). The large contrast between the formation

and fracture capillary pressure keeps driving the water into the formation, particularly during shut-in (Makhanov et al. 2014).

The invasion of water into tight gas sandstones causes mobility reduction, known as water block (Abrams and Vinegar 1985). Longoria et al. (2017) demonstrated that discontinuity in capillary pressure at the fracture face significantly decreases gas relative permeability. They related this blocking behavior to the Rapoport-Leas number (N_{RL}) (Rapoport and Leas 1953), $N_{RL} = \mu u L/\sigma$, which is a ratio of the viscous to capillary forces for a core length L. The simplest definition of the Rapoport-Leas Number is proportional to the ratio of the pressure drop across flow length versus the capillary pressure, $\Delta P/P_c$ (Lake et al. 2015).

Figure 2.3 illustrates the relationship mentioned above: water block seems to occur when $\Delta P/P_c$ is smaller than a certain value. Note that using surfactant formulation increases that ratio by three factors as it significantly decreases interfacial tension (IFT). Although the authors conducted these core experiments for a low-permeability conventional sandstone core, they claimed that the water block/Rapoport-Leas number (represented by $\Delta P/P_c$) correlation would remain true for URs. Production from URs occurs at large capillary forces conditions, typically at a small $\Delta P/P_c$ ratio that ranges from 0.1 to 10, and therefore should suffer from relative permeability reduction (Longoria et al. 2017).

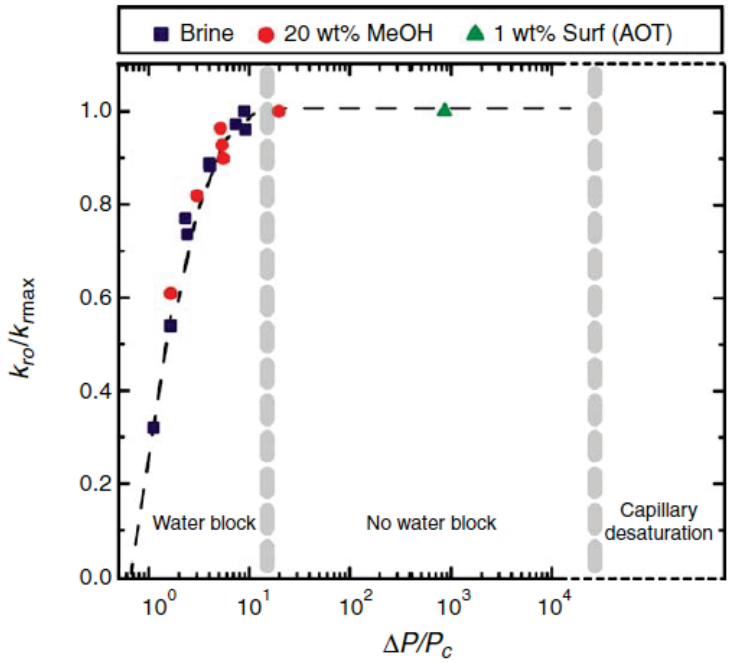

Figure 2.3 Gas relative permeability measurements for a conventional, low-permeability core during flowback of different fracturing-fluid types (from Longoria et al. 2017).

At field conditions, the drawdown pressure ΔP is usually limited by production conditions. Therefore, any effective production-improvement remedy must involve the capillary forces (here, represented by P_c). One remedy is to reduce the IFT by adding surfactant formulations to the fracturing fluids. Another is to shut-in the well after the fracturing treatment. During shut-in, the water slowly imbibes into the formation because of the capillary pressure gradient caused by the non-uniform, water-saturation profiles. The resulting new fluid distribution will have smaller water volumes accumulating at the fracture face, and therefore results in larger hydrocarbon relative permeability. Longoria et al. (2017) observed an improvement in hydrocarbon relative permeability after shutting in

the core. Furthermore, no flowback of water was measured after resuming the flow, supporting that the enhancements are caused by fluid redistribution inside the core.

Although insightful, the conventional rock core-flow experiments discussed above are still not representative of unconventional shale plays. Measuring permeability of shale rock is challenging because steady-state flow conditions are almost unachievable at such small permeability. Pulse-decay gas permeability is the most reliable method to measure the permeability of small-permeability plugs (smaller than 0.1 md) (Jones 1997). Bostrom et al. (2014) investigated the change in permeability over time associated with water imbibition by running pulse-decay experiments to samples from different shale plays. As summarized in **Figure 2.4**, the experimental observations agree with the previously established theory that permeability is recovered over soaking time because of the continued redistribution of the water block. The rate at which the permeability recovers; however, appears to be rock dependent.

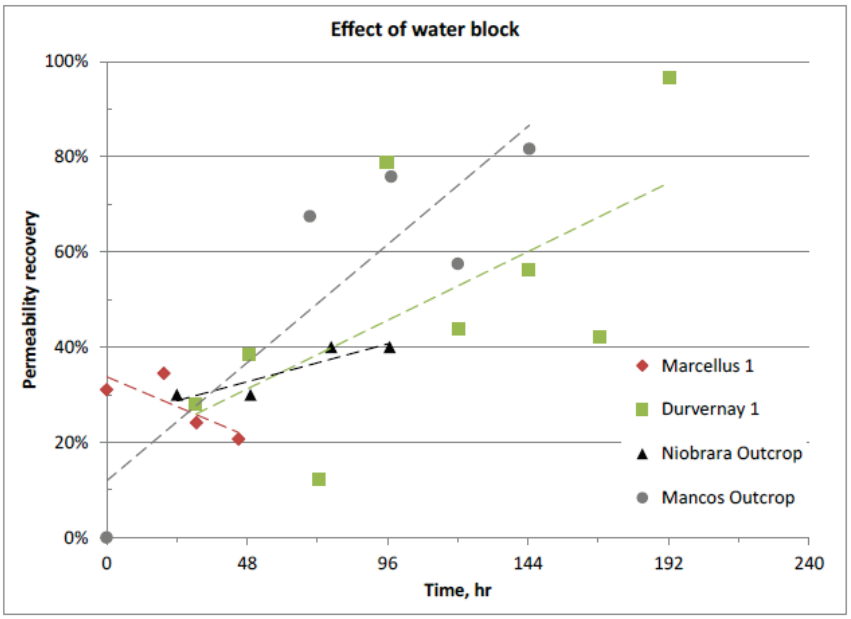

Figure 2.4 Permeability variation for the samples with respect to soaking time. Although initially sharp, the drop in permeability was recovered to a large extent for most of the samples (from Bostrom et al. 2014).

2.4.2 Well Soaking After Fracturing: A Mobility Reducer or Production Improver

Field observations seem to contradict the theory of relative-permeability reduction caused by water invasion, particularly for gas shale plays. Hydrocarbon productivity has been reported to be unaffected in many cases and even to be enhanced in some cases after shutting in wells for long time periods (Cheng 2012; Bertoncello et al. 2014). Deng and King (2018) explained that the production enhancement might be a result of the counter-current flow of gas as the water is imbibed into the formation. **Figure 2.5** shows how the spontaneous imbibition of water could remarkably act as a production mechanism. As explained earlier, gravity assists the segregation of the two phases inside the fractures, particularly in case of gas in large-conductivity fractures. As a consequence, the area

available for water imbibition shrinks over time resulting in a declining rate of gas counter flow. Another implication is that large volume of hydrocarbons will tend to accumulate within fractures over soaking time, resulting in favored relative permeability for hydrocarbons. Given the extensive stimulated rock volume of a typical hydraulic fracturing treatment, those hydrocarbon accumulations could significantly add to production.

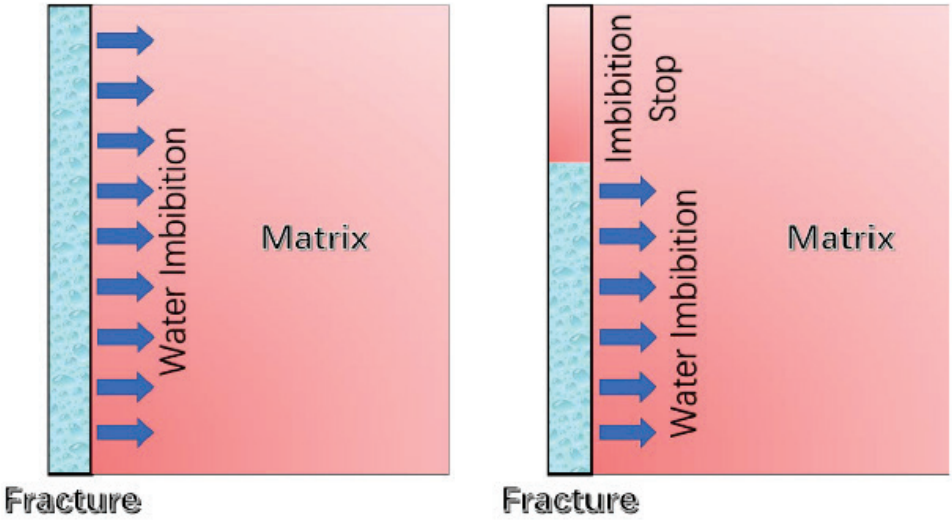

Figure 2.5 Schematic illustrating the gravity-assisted counter-current flow from matrix to fracture associated with spontaneous imbibition of water (from Deng and King 2018).

2.4.3 Relative Permeability Model inside Fractures

We attempt to conduct a reservoir-simulation experiment to evaluate the significance of relative permeability curves inside fractures by considering two different arbitrary curves (shown in Error! Reference source not found.) in production from a shale oil well. We consider comparing between the oil-rate responses for three cases: Case (1)–using Curve 1 in both matrix and fracture blocks; Case (2)–using Curve 1 in matrix blocks

and Curve 2 in fracture blocks; and Case (3)–using Curve 2 in both matrix and fracture blocks.

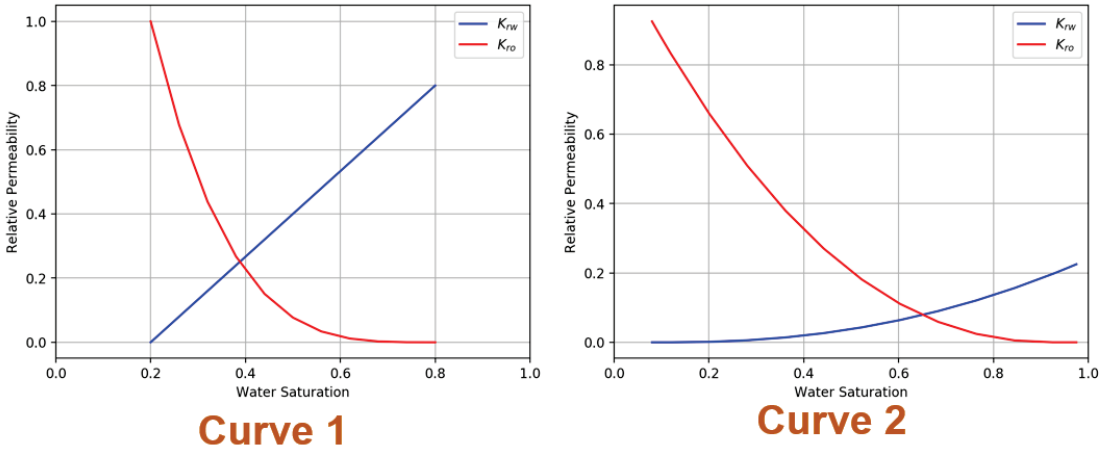

Figure 2.6 Two arbitrary relative permeability curves used in simulation setup.

Simulation results indicate that the changing the relative permeability curve inside fractures has the most substantial effect on the production profile (see **Figure 2.7**). This is because of the large contrast between conductivity inside matrix and fractures–any changes in properties inside fractures become more dominant in governing fluid flow. Although important as demonstrated, relative permeability curves inside the fractures have not been well-studied in the literature. Some studies used a straight-line relative permeability models for multi-phase flow inside fractures (Mattar et al. 2008; Hersandi 2013), whereas other studies implemented curvature in the curves and accounted for end-point saturations (Khoshghadam et al. 2015; Argawal and Sharma 2013). The majority of simulation studies, however, do not touch on justification for the relative-permeability model chosen for either the matrix or the fracture.

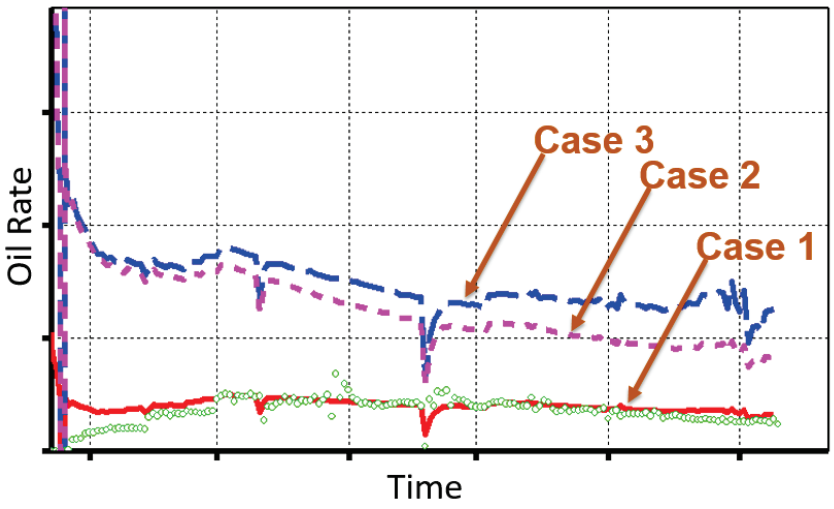

Figure 2.7 Simulation oil-rate results showing that Case (2) (where relative permeability changes only in fractures) has the most significant influence on the response.

The propped porous media created by hydraulic fracturing is entirely different than the shale matrix. This implies a distinct relative permeability inside the fractures that should allow for significantly less-restricted flow for the two phases. Still, a straight-line realization seems not plausible because, even though propped fracture volumes are highly conductive, they undergo compaction, imposing capillarity-caused restrictions on fluid flow.

It appears that relative permeability inside the matrix and fracture cells will remain uncertain to a certain degree. Therefore, uncertainty assessment and probabilistic, history-matching methods may be specifically applied for every field case to assist in determining proper realizations.

2.5 MOTIVATION FOR THE MODELING APPROACH DEVELOPED IN THESIS

As demonstrated, the water distribution within the fracture and the matrix at the start of production is crucial for any numerical simulation. Conventional finite-difference models would not be capable to handle the immense injection flow rate, associated with hydraulic-fracturing treatments, because of the large pressure build up that will be encountered. For that reason, a geomechanics-based simulator that incorporates poroelastic effects would be superior. An ideal implementation would be simulating the hydraulic fracture treatment, followed by soaking period and finally followed by production. By the time the well is put on production, the simulator would have calculated the saturation profiles at every cell based on the fluid-flow physics. However, one limitation is that this modeling technique is computationally expensive and its application to field-scale studies could be limited.

To simplify the problem, one implementation could be to: ignore the first phase of creating the fractures; start with fully saturated fracture cells; and simulate the next steps of soaking and production. In the case of large uncertainties or if the above methods are not suitable, further simplification could be done by dividing the reservoir into three zones: fracture cells; stimulated rock volume (SRV) cells; and formation matrix cells. Each group of cells will be assigned an uncertain saturation and possibly uncertain relative permeability. The uncertainty could then be quantified by conditioning the model to observed history.

In this thesis, we adopt a modeling scheme that consists of the three aforementioned zones. Using that scheme, we extend Eltahan et al.'s (2019) integration to multi-well AHM in an attempt to make the procedure more compact. We define distinct fracture and SRV

zones around each well. This setting allows us to investigate well-interference effects we observe on the surface production and achieve optimization on a multi-well scheme.

METHOD

Chapter 3: Method – Multi-Well AHM

The integration of EDFM with available commercial simulators was made possible because EDFM calculations run in an external environment independent of the simulator's source code. With that stated, further integration of EDFM into commercial optimization and uncertainty quantification tools has not been previously achieved. To achieve this, the pre-run EDFM calculations must be controlled and run in an automatic manner while the optimizer is re-arranging parameters. Essentially, making that integration allows for full parameterization and sensitivity analysis of fracture characteristics. This allows EDFM's modeling capabilities to become more powerful, such that various fracture configurations can be investigated at once.

In this chapter, we develop an automated optimization and assisted history-matching workflow by integrating EDFM with an optimization tool available in a commercial simulation package. First, an overview of the method is described. Then, an in-detail description of the main components of the general-purpose workflow will follow.

3.1 OVERVIEW OF THE METHOD

In this work, we are particularly interested in automatically matching production-history data while simultaneously integrating full parameterization of EDFM fractures (and their respective features), which can dominate model-performance results. The main steps for the general-purpose optimization workflow are shown in **Figure 3.1**. In the first step, we parameterize general fracture attributes such as fracture half-length, height, aperture, and conductivity. Additional parameters can also include other reservoir properties, such as matrix permeability, relative permeability endpoints and exponents, and initial

saturations. Other configurations, e.g., varying cluster spacing or frequency, can be also exploited in a categorical manner. All these parameters can be defined in an optional manner; if a parameter is identified as uncertain, and then it can be activated to vary either between categories or within number ranges based on prior assessment.

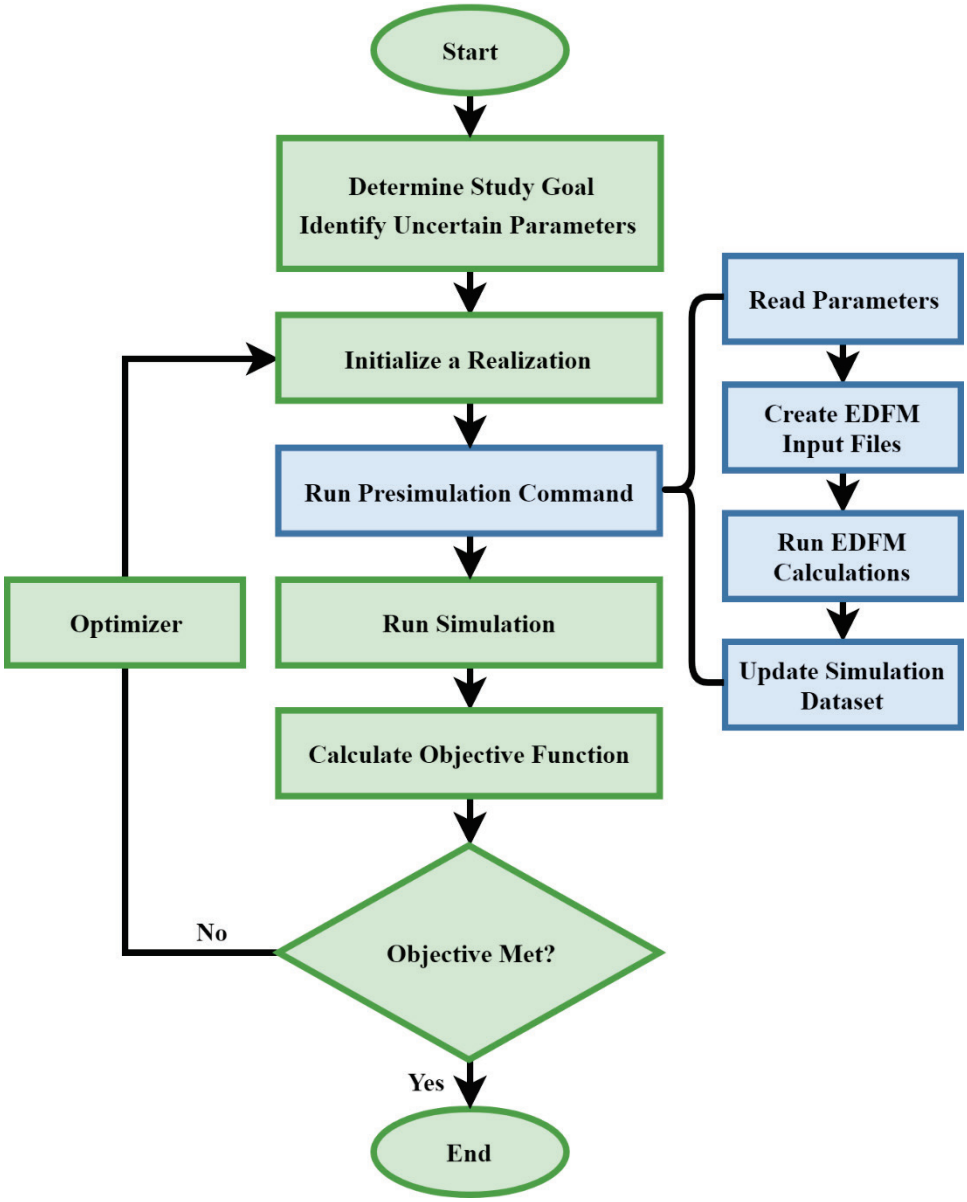

Figure 3.1 Flowchart of the proposed history matching and optimization method.

In the next step, the parameter set generated by the optimizer is exported to an external environment. Then, a presimulation command starts running in the background. It is designed to read the parameters and generate an EDFM input accordingly. For each

model state, the presimulation command starts up EDFM calculations, upon which it updates the simulation dataset with the new non-neighboring blocks and their associated connections.

Finally, the produced numerical model is then run on a simulator, and the predefined objective function is calculated, e.g., history matching misfit error. It is worth noting that the computation time required for a study is mostly spent between the EDFM preprocessing and simulation runs. The computation time required for the rest of the steps is relatively insignificant.

$$t_{study} \approx N(t_{sim} + t_{EDFM})$$

where, N is the total number of simulation runs, t_{EDFM} is the average computation time required for the EDFM non-neighboring connections calculations, and t_{sim} is the average computational time required for a single simulation run.

3.2 PARAMETERIZATION

This work is primarily focused on modeling production from unconventional reservoirs, e.g. shales. As learned from a long history of trials at the Barnett Shale (Martineau 2007), oil and gas recovery from tight and shale rocks is now predominantly achieved by initiating hundreds of hydraulic fractures along a horizontal wellbore. As discussed previously, many attributes that describe the shape, intensity and conductivity of hydraulic fractures remain uncertain to a large extent after hydraulic-fracturing treatments. Taking that uncertainty as well as the typical variability of scope into account, we designed a parameterization scheme to be both flexible and robust.

On one hand, the scheme is flexible such that each attribute for each individual fracture can be tuned as an uncertain parameter. On the other hand, for practical purposes, there is an often need to reduce the number of uncertain parameters. As such, the

parameterization scheme allows for congregating individual fractures into *fracture groups* that share the same properties. Simplifications, such as grouping the fractures, which are part of a single stage, or along the whole lateral, are conceivable. In these scenarios, each property for each fracture group is uniformly assigned by a single parameter.

3.2.1 Fracture Template

To achieve the above-stated capabilities, it is necessary to develop a template that creates EDFM fractures based on intended-for-purpose keywords. All natural and hydraulic fractures are represented by two-dimensional, bi-wing planes. However, the way they are constructed varies depending on a predefined type. Here, any fracture group can either be classified type 0, 1 or 2. This classification is motivated by the practical field applications.

For type 0, fracture positions are assumed at equal distances from each other along an *initiation line* defined by two points in space. The coordinates of such fractures in the grid are calculated such that they are symmetrically positioned around node points. The nodes are equally spaced points positioned along the initiation lines. A summary of the keywords that are available to describe Type 0 fracture groups is presented in **Table 3.1**. Note that some keywords have default values, and hence are not essential requirement for the template.

Keyword	Default	Description
Point1	-	The coordinates of one end of the initiation line
Point2	-	The coordinates of the other end of the initiation line
Nodes	-	The number of nodes along the initiation line. Each node is the center point to a single fracture or a cluster of fractures.
Freq	1	The number of fractures per each node
Sep	0	The distance between fractures corresponding to each node
Angle	90	The azimuth angle of the fracture plane measured anti-clockwise with respect to the initiation line
LRatio	0.5	The proportion of the left-wing length to the total length of the fracture
HRatio	0.5	The proportion of the height propagation in upward direction to the total height of the fracture
HLength	-	Fracture half length (x_f)
Height	-	Fracture height
Perm	-	Fracture permeability (md)
Apert	-	Fracture aperture
Active	1	Determines whether the set of fractures are active or not (1 = active, 0 = inactive)
Dip	90	Dipping angle of the fracture plane (90 = vertical)

Table 3.1 List of the keywords allowed for fracture group Type 0.

Type 1 fractures have the same attributes as Type 0 except for one difference: node points are explicitly defined by their coordinates. This gives room for flexibility to suit conditions

such as when the well trajectory is not assumed linear or when the fracture stages/clusters cannot be assumed uniformly spaced. **Table 3.2** describes a list of keywords that define fracture group Type 1. Type 2 fracture groups are implemented for single fractures defined by a single point and have the same attributes as Type 0 and Type 1. Such classification would be more suitable for the representation of natural faults or long inter-well induced fractures.

Keyword	Default	Description
Points	-	The coordinates of fracture nodes
Freq	1	The number of fractures per each node
Sep	0	The distance between fractures at each node
Angle	90	The azimuth angle of the fracture plane measured anti-clockwise corresponding to the initiation line.
LRatio	0.5	The proportion of the left-wing length to the total length of the fracture
HRatio	0.5	The proportion of the height propagation in upward direction to the total height of the fracture
HLength	-	Fracture half length (x_f)
Height	-	Fracture height
Perm	-	Fracture permeability (md)
Apert	-	Fracture aperture
Active	1	Determines whether the set of fractures are active or not. (1 = active, 0 = inactive)
Dip	90	Dipping angle of the fracture plane (90 = vertical)

Table 3.2 List of the keywords allowed for fracture group Type 1.

3.2.2 Uncertain Parameters

A fracture template is first created for the base case with current understanding of the model. Once a parameter is recognized as uncertain, it can be passed along to the code in the format "{fracture group}_{keyword}". For example, if the half-length for fracture

group Well-1 is doomed uncertain, it should be represented by the parameter "Well-1_HLenght".

Each uncertain parameter may follow a prior distribution described by a probability-density function (PDF). The prior distributions are usually determined based on expertise and knowledge. The prior PDF could be uniform, triangular, normal or lognormal. The prior distribution may also be discretely customized by manually entering parameter intervals and their respective weights. Parameters can take any value from a continuous real range between upper and lower bounds. Alternatively, parameters could be defined as discrete integers that vary on given levels. Another option is switching between complete lines of texts. This option allows the alternation between different possible scenarios or categories.

Effectively, all the aforementioned fracture keywords can be passed on as uncertain parameters. If used as uncertain parameters, a combination of these keywords allows full control over position, frequency, geometry and conductivity of a fracture group. Of special interest are fracture height, aperture, half-length and permeability. As discussed in the literature review, characterization of these attributes is inherently uncertain and sensitivity of simulation output with regards to them is substantial. Therefore, they are often included as main tuning parameters in history matching studies (e.g., Wantawin et al. 2017a; Tripoppoom et al. 2019).

Other notable uncertain properties are permeability of the formation in the region surrounding fractures. As reservoir pressure drops with depletion, the formation undergoes compaction that may cause permeability hindrance. In this work, we describe the relationship between permeability decline and pressure drop as exponential, motivated by recent experimental results (Mokhtari et al., 2013).

$$k = k_i e^{-c(p_i - p)}$$

Where k_i and p_i are the initial permeability (in md) and reservoir pressure (in MPa), respectively, k is the calculated permeability at pressure p, and c is the compaction coefficient. **Figure 3.2** is an illustration of a hypothetical permeability decline scenario. Following the same manner, compaction coefficient would be an optional tuning parameter in the assumption of a pressure-dependent permeability. By default, permeability is assumed constant unless a compaction coefficient is defined by the keyword "ctablekh".

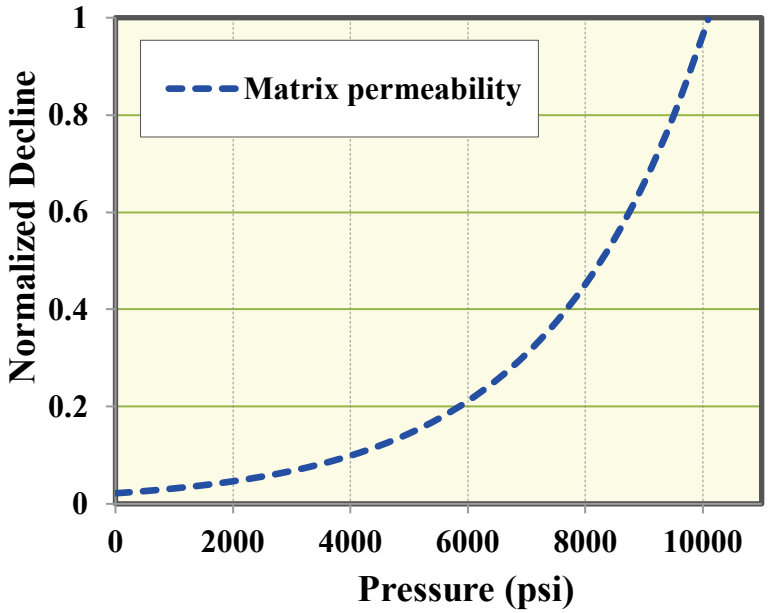

Figure 3.2 Decline of permeability normalized to its initial value plotted against pressure with 10095 psi initial pressure and 0.055 compaction coefficient.

Considering the heterogeneity of shale and the water injection during hydraulic fracturing, initial fluid saturations and relative permeability would have large degrees of uncertainty, as was discussed in the literature review chapter. They become decisive history-matching tuning parameters, particularly to match water- and gas-production rates. In our method, relative permeability is modified on the basis of Brooks-Corey model (Corey 1954). Saturation endpoints and power-law exponents are the main tuning parameters to relative permeability model. In our implementation, different regions of the reservoir may or may not be tagged with the same relative permeability model. In essence, every single fracture group and stimulated rock volume (SRV) region can individually be described by a unique relative permeability model. Alternatively, with the purpose of simplifying the problem, different reservoir regions can be collectively marked with the same relative permeability model.

Relative permeability curves are constructed based on 14 keyword modifiers defined in **Table 3.3**.

Keyword	Default	Description
swcon	0	Connate water saturation
Iswcrit	-	Incremental critical water saturation $S_{wcritical} = swcon + Iswcrit$
soirw	0	Irreducible oil saturation in an oil/water system
Isorw	0	Incremental residual oil saturation for an oil/water system $S_{orw} = soirw + Isorw$
krocw	1	Oil relative permeability at connate water saturation
krwiro	1	Water relative permeability at irreducible oil saturation
nw	-	Water-curve exponent for Brooks-Corey functions
no	-	Oil-curve exponent for Brooks-Corey functions
soirg	0	Irreducible oil saturation in an oil/gas system. Connate liquid saturation $S_{lc} = swcon + soirg$
Isorg	0	Incremental residual oil saturation for an oil/gas system $S_{org} = soirg + Isorg$
sgcrit	-	Critical gas saturation
krgcl	1	Gas relative permeability at connate liquid saturation
nog	-	Oil-curve exponent for Brooks-Corey functions
ng	-	Gas-curve exponent for Brooks-Corey functions

Table 3.3 List of the keywords allowed for defining Brooks-Corey relative permeability curves.

3.2.3 Introducing SRV

Here we evaluate the SRV volume around an individual fracture as the volume enclosed between three polygons in 3D: one polygon around the center line of a fracture (i.e., the depth at which fracture was initiated); and two around the top and bottom ends of the fracture height. **Figure 3.3** is a schematic showing how SRV is constructed around a fracture plane. Note that the areas of the polygons intersecting the top and the bottom edges are identical in size and are smaller than the center-polygon area. In addition, there is asymmetry in size along fracture length. SRV area is wider at the center than at the tip of the fracture.

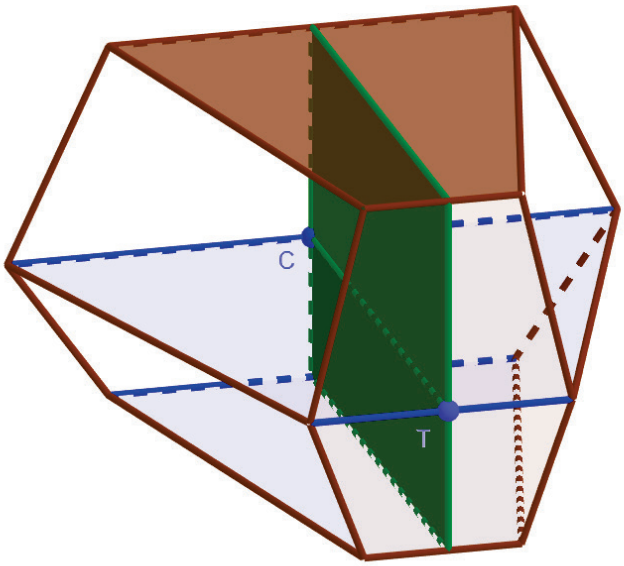

Figure 3.3 Schematic illustrating SRV around half wing of a fracture (shown in green). **C** is the point at the center of fracture whereas at well location, whereas **T** is at located at the fracture's tip on the same level.

SRV region dimensions around each fracture group are defined by modifiers listed in **Table 3.4**. **Figure 3.4** demonstrates the dimensions used to construct SRV around the same hypothetical fracture half wing as in **Figure 3.3** viewed from above. It is worth noting that if "srvctr" is the solely defined keyword, the SRV volume will be assumed cuboid with regular sides. If none of the keywords is defined, there will be no SRV around a fracture group.

Keyword	Default	Description
srvctr	-	Length of SRV central-polygon half side at the center of fracture at the level of fracture initiation (at the well depth)
srvtip	srvctr	Length of SRV central-polygon half side at the tip of fracture at the level of fracture initiation (It is assumed to be the same as srvctr if not given)
srvgradv	1	The ratio of the polygon-side lengths at the initiation line of a fracture to the lengths at the bottom and top edges (e.g., a value of 2 means $(srvctr)_{initiation}/ (srvctr)_{edge} = 2$)
srvcutoff	0.25	A cut-off volume fraction based on which a grid block is selected as part of the SRV blocks group

Table 3.4 List of the keywords allowed for defining SRV.

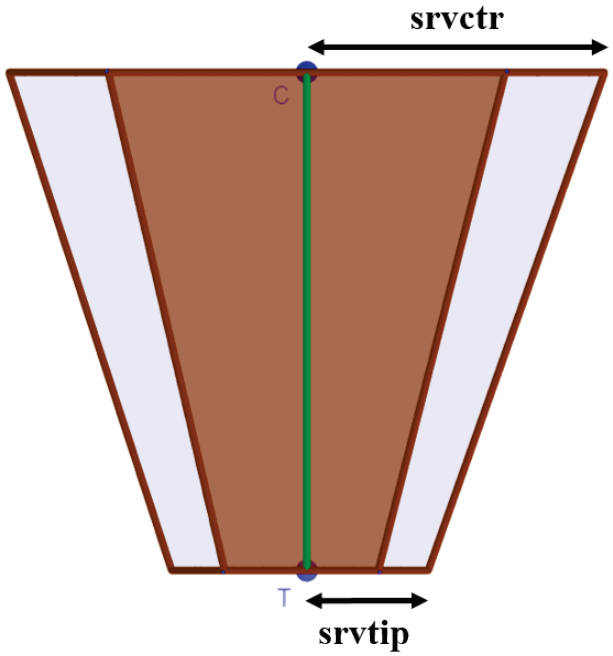

Figure 3.4 Plan view schematic illustrating SRV dimensions around half wing of a fracture (shown in green). Dark brown area represents the SRV polygon at the top edge, whereas the lighter-colored area represents the widest SRV section.

Consider an orthogonal grid that has n_i, n_j and n_k grid blocks in i, j and k directions respectively. Each fracture group may have a fraction of grid blocks classified as its SRV region. A fracture group may consist of N fractures. To determine the SRV gridblocks associated with a fracture group, there are to be N iterative steps.

Initialize SRV list;

Repeat for fractures $F = 1, 2, \dots, N$**:**

Repeat for grid layers $k = 1, 2, \dots, n_k$**:**

Calculate SRV polygon dimensions around fracture F **in** k **plane;**

Draw a polygon after determining its vertices;

Repeat for grid blocks $i = 1,2, \dots, n_i$**:**

For $j = 1,2, \dots, n_j$**:**

If a grid block (i, j) **lies entirely inside polygon then:**

Increment grid block (i, j) **to SRV list;**

If $A_{int(i,j)}/A_{gridblock(i,j)} > C_{SRV}$ **then:**

Increment grid block (i, j) **to SRV list.**

A_{int} denotes the intersection area between SRV polygon and a gridblock, $A_{gridblock}$ is the area of the gridblock, and C_{SRV} is a cutoff value defined by the practitioner. As described above, the procedure we adopted is limited to orthogonal grids. Therefore, our method is not suitable for more complicated grids such as corner-point grids. The decision of whether to include a grid block in SRV or not is based on an arbitrary rule. Preferably, the defining threshold should be based on the volume ratio of region intersected by grid block and SRV shape and the volume of the grid block. Although, we adopt simpler implementation by only performing area calculations over 2-D layers, we allow a room for flexibility for the deciding criterion. Besides being able to control the shape and extension of the imaginary SRV volume, the user is able to control the deciding criterion by modifying the cutoff value.

Figure 3.5, **Figure 3.6**, and **Figure 3.7** are sample illustrations of different cases the code is programmed to produce. Each shows a snapshot of a created polygon at some layer k enclosing the selected SRV grid blocks.

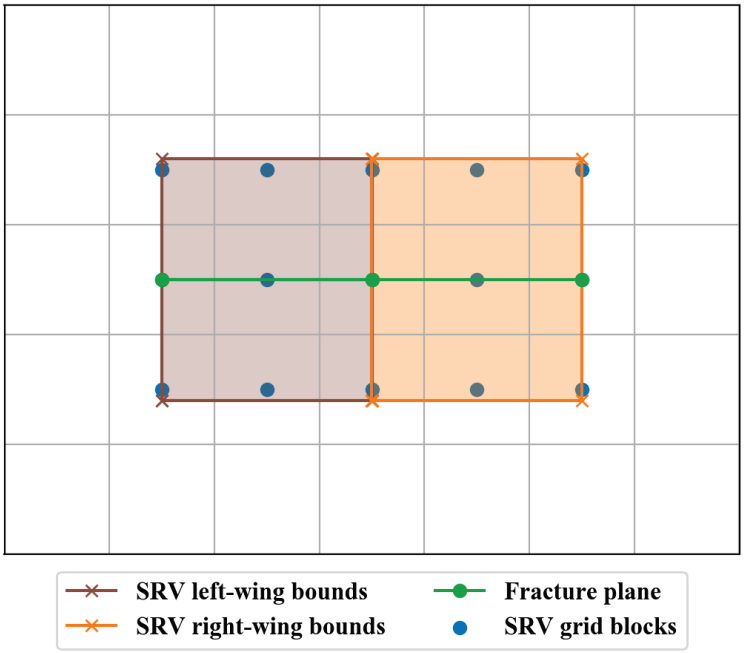

Figure 3.5 Illustration of a simple case of SRV polygon around a symmetrical fracture plane, constructed with the same dimension at the tip as at the center (srvtip = srvctr), and with default cut-off modifier (srvcutoff = 0.25).

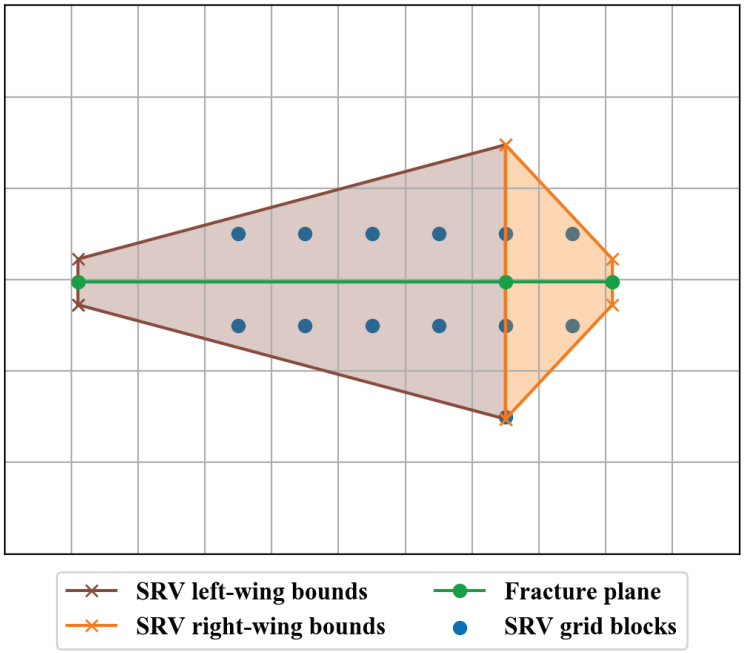

Figure 3.6 Illustration of an SRV polygon around an asymmetrical fracture plane, constructed with 6/1 ratio between srvctr and srvtip, and with cut-off modifier srvcutoff = 0.5.

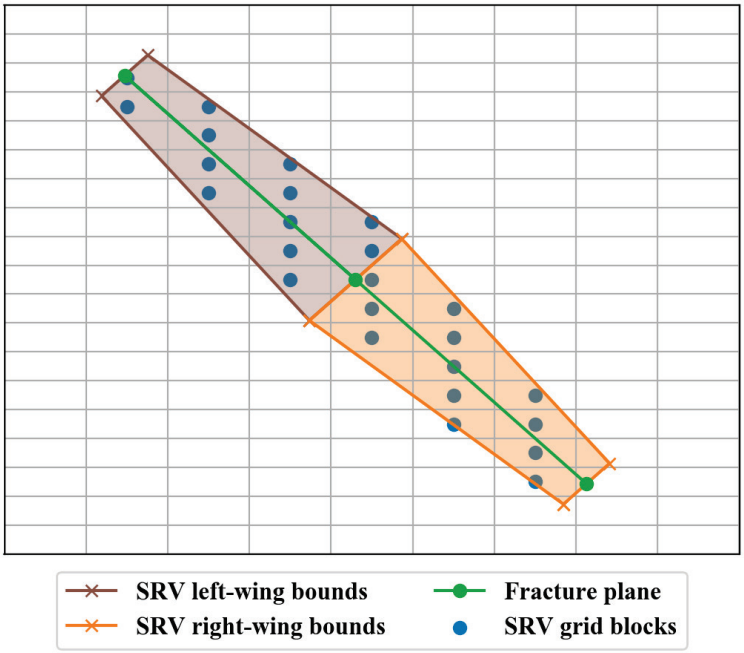

Figure 3.7 Illustration of an SRV polygon around a fracture plane that is not orthogonal in relation to the grid, constructed with 2/1 ratio between srvctr and srvtip, and with cut-off modifier srvcutoff = 0.5.

The variation in SRV at different height levels is exemplified in **Figure 3.8**. In this example, the fracture plane intersects layers $k = 2, 3$ and 4 of the grid. Layer $k = 3$ lies closest to the center of the fracture plane, and hence corresponds to the broadest SRV bounds. Whereas layers $k = 2$ and $k = 4$ are positioned towards the top and bottom edges of the fracture, and as such the SRV bounds are narrower.

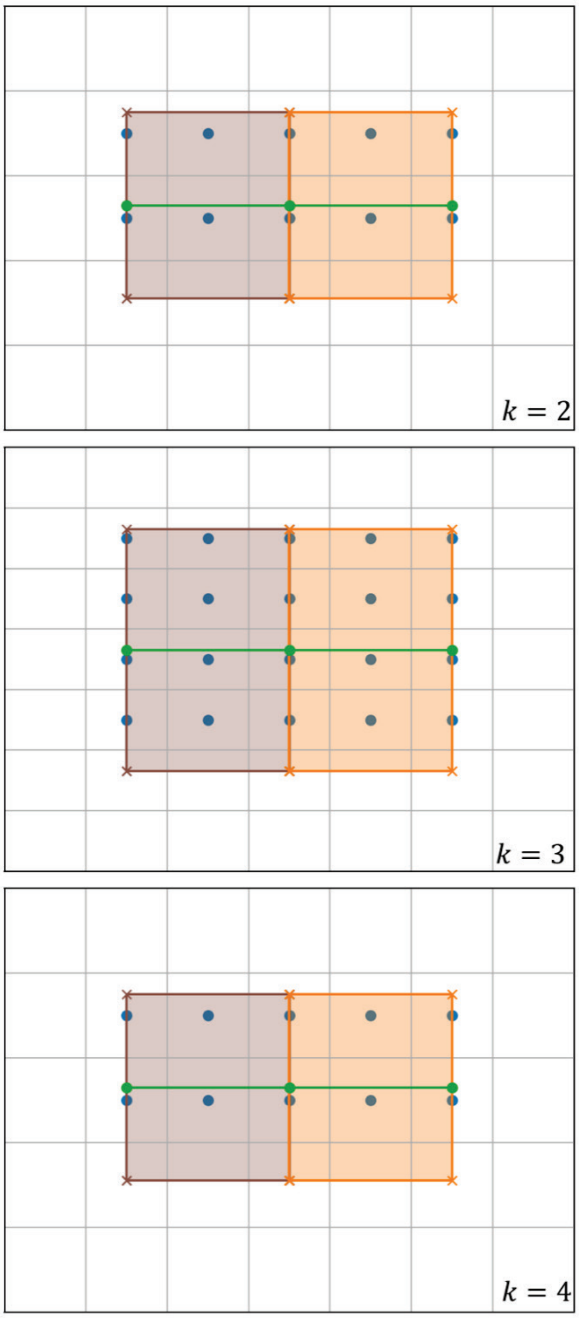

Figure 3.8 SRV polygon around a fracture plane at different layer levels, constructed with ratio between center and edge dimensions srvgradv = 4.

The script is designed to automatically run all fracture groups and divide grid blocks into fracture (FRAC) groups and SRV groups. The method is limited, however, to orthogonal grids with variable grid size. Once the SRV blocks are identified, properties such as initial saturations, permeability and relative permeability models, may be assigned to them using the fracture template. By adding the affix "SRV" to a keyword, one can deploy a certain feature exclusively for the SRV blocks. For example, one may describe initial water saturation for SRV blocks by using the keyword "swiSRV".

Similarly, a feature can be assigned individually to fracture blocks by adding the affix "FRAC" to its keyword. Any of these group-specific parameters can be passed as uncertain parameters in the format "{fracture group}_{keyword}". For example, consider a case where the Corey-relative-permeability exponent for the water curve n_w was uncertain in the SRV region bounding fracture group "Well-2". This uncertainty can be passed using parameter name "Well-2_nwSRV".

3.3 OBJECTIVE FUNCTION

The method can be used in optimization or to assist history matching. When used for optimization, the goal is often to maximize recovery or economic benefit. Besides estimated ultimate recovery (EUR), economic metrics such as net present value (NPV) and rate of return (IRR) may be employed as objective functions. When the purpose is to achieve history matching, the goal would be to minimize the misfit error between simulation results and observed data. All applications presented in this thesis are focused on history matching, and therefore it is worth elaborating on history matching error.

History-matching error is calculated in a way that reflects data significance and quality; and normalizes the error to the scale of data-points magnitude. The error Q_i is

averaged from different data types for each well and is reported as a percentage according to the following equation (CMG-CMOST 2017):

$$Q_i = \frac{1}{\sum_{j=1}^{N(i)} tw_{i,j}} \times \sum_{j=1}^{N(i)} \frac{\sqrt{\frac{\sum_{t=1}^{T(i,j)} \left(mw_{i,j,t}^{m}\right)^2 \left(Y_{i,j,t}^{s} - Y_{i,j,t}^{m}\right)^2}{\sum_{t=1}^{T(i,j)} \left(mw_{i,j,t}^{m}\right)^2}}}{Scale_{i,j}} \times 100\% \times tw_{i,j}$$

where i, j, t subscripts denote well, production data type, and time respectively. $N(i)$ is the total number of production data types for well i. $T(i,j)$ is the total number of measured data points for a data type j. tw and mw are the term weights for production data type, and for each measured data point respectively. Y^s and Y^m are simulation output- and measured-data points respectively.

3.4 AHM ALGORITHMS IMPLEMENTED

The commercial simulation package provides a diverse suite of optimization engines available for use including particle-swarm optimizer (PSO), Bayesian and differential evolution methods. For exploring the parameter space, these methods apply techniques from experimental design theory in an effort to reduce the number of effective parameters. A good experimental design shall minimize the correlation between the selected parameter vectors, i.e., orthogonal design, and shall cover the parameter space, i.e., space-filling design (CMG-CMOST 2017).

3.4.1 Bayesian Algorithm I

To practically apply Bayesian inference to field-scale AHM problems, Yang et al. (2015) introduced a proxy-based acceptance-rejection method (PAR). The method applies a fast radial-basis neural-network proxy to approximate the posterior. As such, expensive reservoir simulations are only run for a certain model only if its proxy-estimated posterior is accepted.

A flowchart summarizing the main steps of the algorithm is summarized in **Figure 3.9**. In the first iteration, a number of models is generated using a Latin Hypercube design that ensures orthogonality and space-filling. Once the initial batch of models completes running, an initial proxy-model will be trained with the output of that initial design. This proxy can be used to approximate the posterior PDF for any parameter-combination candidate.

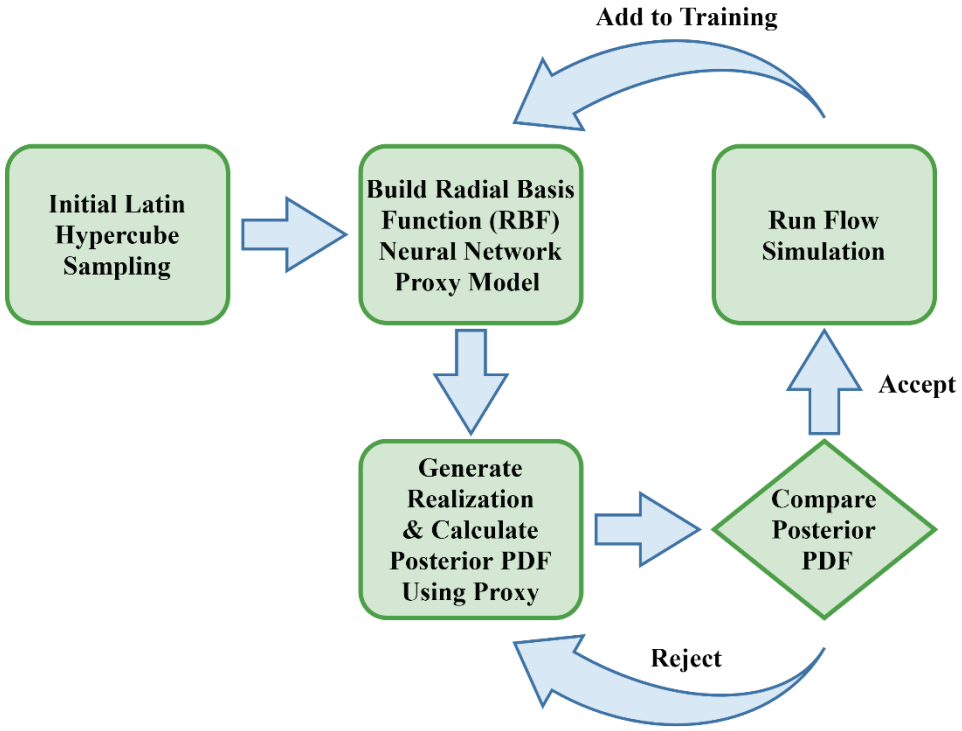

Figure 3.9 Flowchart highlighting the main steps of the Bayesian-inversion algorithm with a proxy-based acceptance/repentance (PAR) sampler.

In the following stage, a new candidate is generated at each following iteration. For a certain candidate to be accepted, its posterior should satisfy the criterion:

$$p_{candidate} \geq rand(0,1) \times p_{best}$$

where $p_{candidate}$ is the estimated posterior of the current candidate, p_{best} is the posterior for the best model, and $rand(0,1)$ is a random number drawn from a uniform distribution with 0 and 1 bounds. If the posterior is smaller, another random candidate is picked, and the comparison is reevaluated. If the posterior is larger, then the current candidate is

accepted and is run on a simulator. Simulation result for the new model is used to enhance the proxy's quality and p_{best} is updated accordingly.

3.4.2 Bayesian Algorithm II

Metropolis-Hastings Markov Chain Monte Carlo (MCMC) is an algorithm that performs a random walk to sample from probability distributions (Metropolis et al. 1953; Hastings 1970). A probabilistic rule allowing some moves to be accepted and others to be rejected regulate the random walk. Metropolis-Hastings MCMC is known to converge to the exact posterior, but at a prohibitively large number of iterations.

The commercial simulator package offers another Bayesian method based on the Metropolis-Hastings MCMC algorithm. Instead of the hundred thousands or millions of runs required by standard MCMC algorithms, this implementation requires relatively smaller number of simulations (usually a few thousand runs for problems consisting of 20 or more parameters). Sampling here differs from that of the standard Metropolis-Hastings. Significant weight is assigned to sampling from the peak of the posterior and its vicinity. Whereas the tails of the posterior are almost disregarded. Hence, unlike standard MCMC samplers, this variant does not guarantee convergence on the posterior, and of course does not correctly calculate the evidence. Moreover, Metropolis-Hastings samplers are known to have convergence issues particularly in the case of multimodal distributions. The Markov chains may get trapped in local minima in the likelihood space.

3.4.3 DECE Algorithm

DECE engine is a commercial iterative optimizer that runs in cycles to search for history-matching solutions. Each cycle consists of two stages: a designed-exploration stage and a controlled-evolution stage (CMG-CMOST 2017). In the first stage, experimental

design and Tabu search techniques are applied to carefully design an exploratory set of simulation datasets. This preliminary set allows us to gather as much information as possible about the solution space. In the second stage, the optimization algorithm statistically analyzes the results and excludes the values of parameters that result in divergence. This narrows down the search space for the next exploration stage. The algorithm routinely checks the rejected values to avoid getting trapped in local minima. This method allows early sampling of the full range of possible results/outcomes and then converges toward the defined goal, which in our cases, is to reduce the history match error.

3.4.4 Particle Swarm Optimization (PSO) Algorithm

Particle swarm optimization (PSO) is a derivative-free stochastic optimization algorithm inspired by the movement of individuals in a bird flock or fish school (Kennedy and Eberhart 1995). This method formulates a swarm (population) of dynamic particles (solution candidates). As the algorithm progresses, the particles keep switching their positions in the swarm in pursuit of finding better solutions. In every iteration, each particle is assigned a velocity that is calculated based on a few formulae.

Let S be the number of population of particles, each with an initial position $x_i \in \mathbb{R}_n$ in the parameter space b and a velocity $v_i \in \mathbb{R}_n$. Let p_i be the best-known position of particle i and let g be the best-known position of the entire swarm. The following steps summarize PSO algorithm:

For each particle $i = 1, \ldots, S$**:**

Initialize $x_i \sim \mathrm{U}(b_{lo}, b_{up})$ **with a random uniform distribution**

Set the particle's best-known position to its initial position: $p_i \leftarrow x_i$

If $f(p_i) < f(g)$ **then:**

Update the swarm's best-known position: $g \leftarrow p_i$

Initialize $v_i \sim \mathrm{U}(-|b_{up} - b_{lo}|, |b_{up} - b_{lo}|)$

While a termination criterion is not met:

For each particle $i = 1, \ldots, S$**:**

For each dimension $d = 1, \ldots, n$**:**

Generate random numbers $r_p, r_g \sim U(0,1)$

Update the particle's velocity

$$v_{i,d} \leftarrow \omega\, v_{i,d} + \varphi_p\, r_p\, (p_{i,d} - x_{i,d}) + \varphi_g\, r_g\, (g_d - x_{i,d})$$

Update the particle's position: $x_i \leftarrow x_i + v_i$

If $f(x_i) < f(p_i)$ **then:**

Update the particle's best-known position: $p_i \leftarrow x_i$

If $f(p_i) < f(g)$ **then:**

Update the swarm's best-known position: $g \leftarrow p_i$

In the above algorithm, ω is an inertia term that controls the convergence of the algorithm. φ_p is a weighting factor known as the cognition component, which tunes the linear attraction of the velocity towards the best position of a particle. φ_g is another weighting factor known as the social component, which tunes the linear attraction towards the global best particle.

PSO is relatively easy to implement and efficient to run and it has been successfully applied for AHM inverse problems (e.g., Mohamed et al. 2010; Vazquez et al. 2015). One obvious limitation, however, is its dependence on the manual setting. The choice of PSO

algorithm terms has a major impact on the optimization performance, and the ideal choice can vary depending on the problem itself. Determining the best choices for PSO settings is beyond the scope of this thesis, although has been addressed elsewhere in the literature (e.g., Mohamed et al. 2010).

APPLICATIONS

Chapter 4: Method Testing and Algorithms Benchmarking – A Synthetic Case

4.1 MOTIVATION

Before we take the method to field applications, we first attempt to apply history matching and sensitivity analysis for a synthetic case. The synthetic case is based on a modeling scenario with known properties i.e., truth model. Synthetic field data are produced from the output that results from running the truth model on a reservoir simulator. This approach excludes other uncertainties such as the quality and reliability of acquired field data and the inherent ambiguity of background model information. Hence, we are able to test the validity of the method while controlling some factors that would have been otherwise uncertain in a typical field setting. By implementing the workflow on a hypothetical case with synthetic data, we can make meaningful comparisons of the available commercial AHM algorithms.

In this chapter, we first describe the numerical experiment; list the conditions; define the objectives of the study; and outline the implemented AHM algorithms. Next, we attempt the first AHM experiment with Bayesian Algorithm I, which is of special interest. After presenting detailed results, we examine the effect of using time periods of different lengths on the performance of AHM, using the same algorithm. Later in the chapter, we repeat the same experiment with four other commercially available AHM algorithms. Finally, we compare between the different methods; draw conclusions; and attempt to make recommendations.

4.2 SIMULATION SETUP

We take advantage of the code's multi-well handling capabilities by applying it to a case that consists of two producing horizontal wells. Likewise, we take an advantage of EDFM to create hydraulic fractures along the wells that are not necessarily aligned with the grid's orientation. A 3D visualization of the test case is presented in **Figure 4.1**. As shown in the figure, there are two fracture groups i.e., LH1 and LH2. Each fracture group is constructed with two stages of fractures. Although it represents only a small portion of a typical unconventional well, this simplistic design is adopted here to reduce the computational time per simulation.

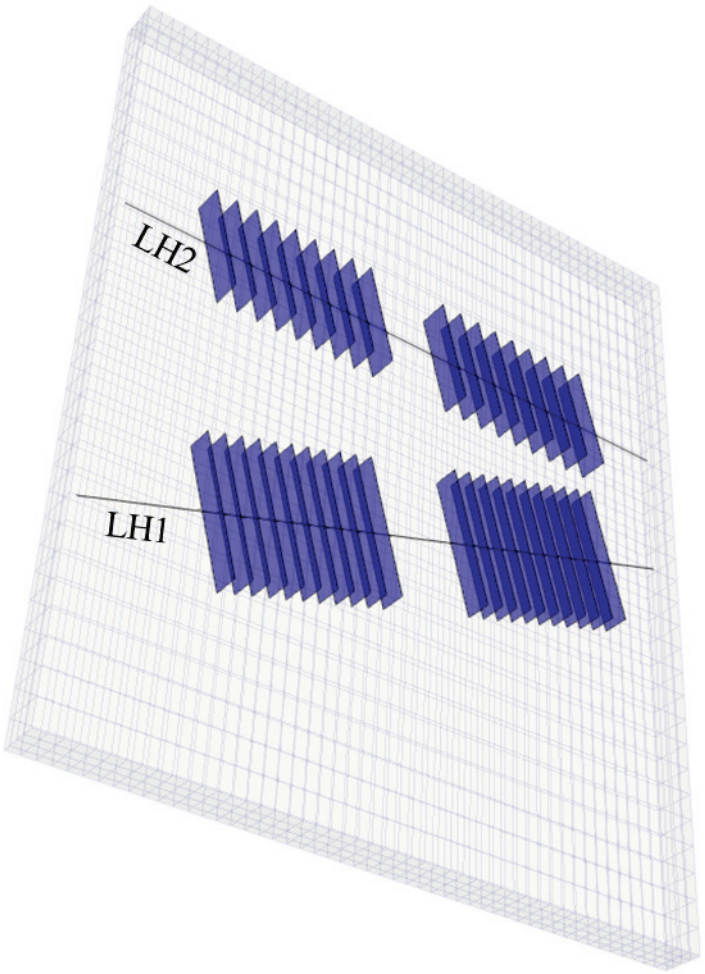

Figure 4.1 3D Visualization of the truth model showing two wells and two fracture groups LH1 and LH2.

The numerical-model configuration has main properties listed in **Table 4.1**. We use a commercial black-oil simulator for running all the constructed models. Relative permeability for flow in matrix blocks is adopted from Birdsell et al. (2015). Curves are constructed using the parameters reported for low-permeability shale oil in Table 1 in their paper and are graphically represented in **Figure 4.2**.

Parameter	Value	Unit
Model dimensions ($x \times y \times z$)	1800 × 1500 × 100	ft
Number of gridblocks ($nx \times ny \times nz$)	50 × 30 × 4	-
Depth to top layer	7500	ft
Layer thickness (layers 1, 2, 3, 4)	28, 26, 26, 20	ft
Porosity (layers 1,2 ,3, 4)	4.5, 7.0, 8.0, 8.5	%
Permeability (layers 1,2 ,3, 4)	200, 450, 750, 650	nD
Bubblepoint pressure	2398	psi
Oil density	50.86	lbm/ft^3
Gas density	0.92	-
Initial water saturation	0.25	-
Initial reservoir pressure	5500 psi	psi
Reservoir temperature	240	^oF

Table 4.1 Base matrix properties and reservoir conditions for the truth simulation setup.

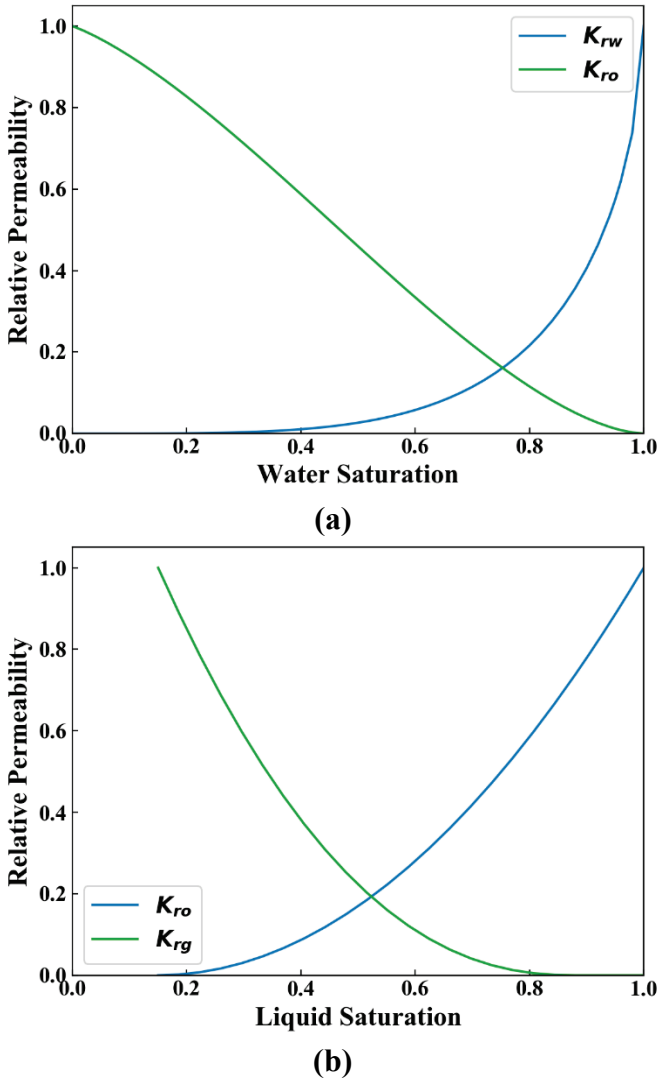

Figure 4.2 Formation-matrix relative permeability for (a) oil/water and (b) liquid/gas.

Formation matrix is not capable of mobilizing water at initial conditions unless initial water saturation is modified (compare the initial water saturation with the critical water saturation in **Figure 4.2.a**). In reality, hydraulic fracturing treatments significantly alter water saturations, particularly in the vicinity of the fractures. Assuming a constant initial water saturation for all the reservoir blocks is not ideal, particularly when the purpose

is matching multi-phase flow rates during flow-back period. For these characteristics, we omit over-simplification and, instead, divide the reservoir into 5 regions: formation matrix blocks; LH1 EDFM fractures (FRAC) blocks; LH1 SRV blocks; LH2 FRAC blocks; and LH2 SRV blocks. The properties for each of these groups are described for the truth model in the following section.

4.2.2 Truth Model

To generate synthetic data, a truth model is first built to run using the simulator. **Table 4.2** summarizes the configuration for the fracture template of the truth model. Note that LH2 fractures are not aligned perpendicularly with respects to the well. Instead, they have the same orientation (or azimuth angle) as LH1 fractures. LH2 is modeled with smaller number of fractures per stage and larger separation distance between fractures.

LH1		LH2	
Keyword	**Value**	**Keyword**	**Value**
Point1	(500, 650, 60)	Point1	(450, 1250, 60)
Point2	(1100, 830, 60)	Point2	(1050, 830, 60)
Nodes	2	Nodes	2
Freq	11	Freq	9
Sep	40 ft	Sep	50 ft
Angle	90°	Angle	73.3°
LRatio	0.5	LRatio	0.5
HRatio	0.6	HRatio	0.6
HLength	160 ft	HLength	120 ft
Height	65 ft	Height	75 ft
Perm	5000 md	Perm	10000 md
Apert	0.01 ft	Apert	0.01 ft
Active	1	Active	1
Dip	90	Dip	90

Table 4.2 Fracture template attributes for truth simulation setup.

Here, we implement the SRV concept we discussed in-detail in the previous chapter. An SRV region with non-symmetrical dimensions is created around each individual fracture with the properties listed in **Table 4.3**. Note that initial saturations, for SRV and FRAC groups, are different than these for the formation matrix.

LH1		LH2	
Keyword	**Value**	**Keyword**	**Value**
srvctr	40 ft	srvctr	40 ft
srvtip	20 ft	srvtip	20 ft
srvgradv	2	srvgradv	2
permiSRV	0.001 md	permiSRV	0.005 md
swiSRV	0.40	swiSRV	0.40
swiFRAC	0.45	swiFRAC	0.5

Table 4.3 SRV region dimensions and initial saturation and permeability for SRV and FRAC blocks.

Relative permeability models are assumed the same for FRAC and SRV blocks for both wells, and are different than the formation-matrix relative permeability (See **Figure 4.3** for the relative permeability curves). Truth-values for the constructed Corey-type relative- permeability models are listed in **Table 4.4**.

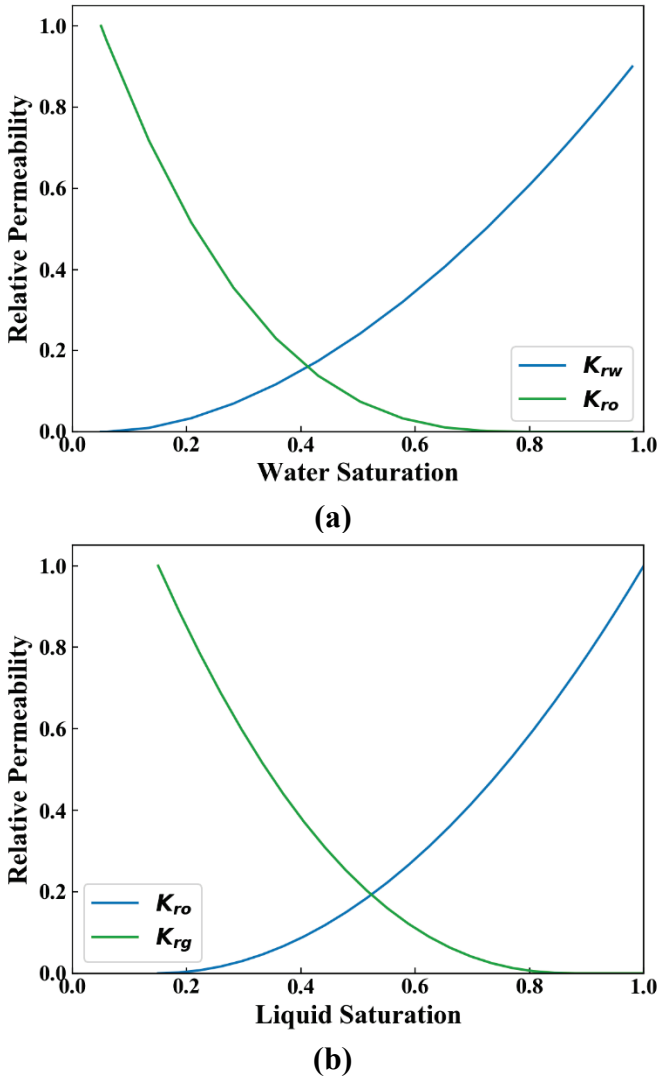

Figure 4.3 Truth SRV and fracture blocks relative permeability for (a) oil/water and (b) liquid/gas.

Keyword	Value	Keyword	Value
swcon	0.05	no	2.8
Iswcrit	0.01	soirg	0.1
soirw	0.02	Isorg	0.0
Isorw	0.18	sgcrit	0.12
krocw	1.0	krgcl	1.0
krwiro	0.9	nog	2.0
nw	1.8	ng	2.3

Table 4.4 Truth-values for parameters used to construct Corey-type oil/water and gas/liquid relative permeability curves.

4.2.3 Synthetic Data

We run the truth reservoir model described in the previous section to obtain synthetic data. The simulation is run for a period of 1375 day (i.e., 3 years and 9 months) with produced-oil rates enforced as the primary production constraint. Production decline follows typical trends from Eagle Ford shale, prorated to the size of the sector considered here (**Figure 4.4**). From the results of this simulation, a total of 1375 daily data points are collected for bottom-hole pressure (BHP), gas- and water-production rates.

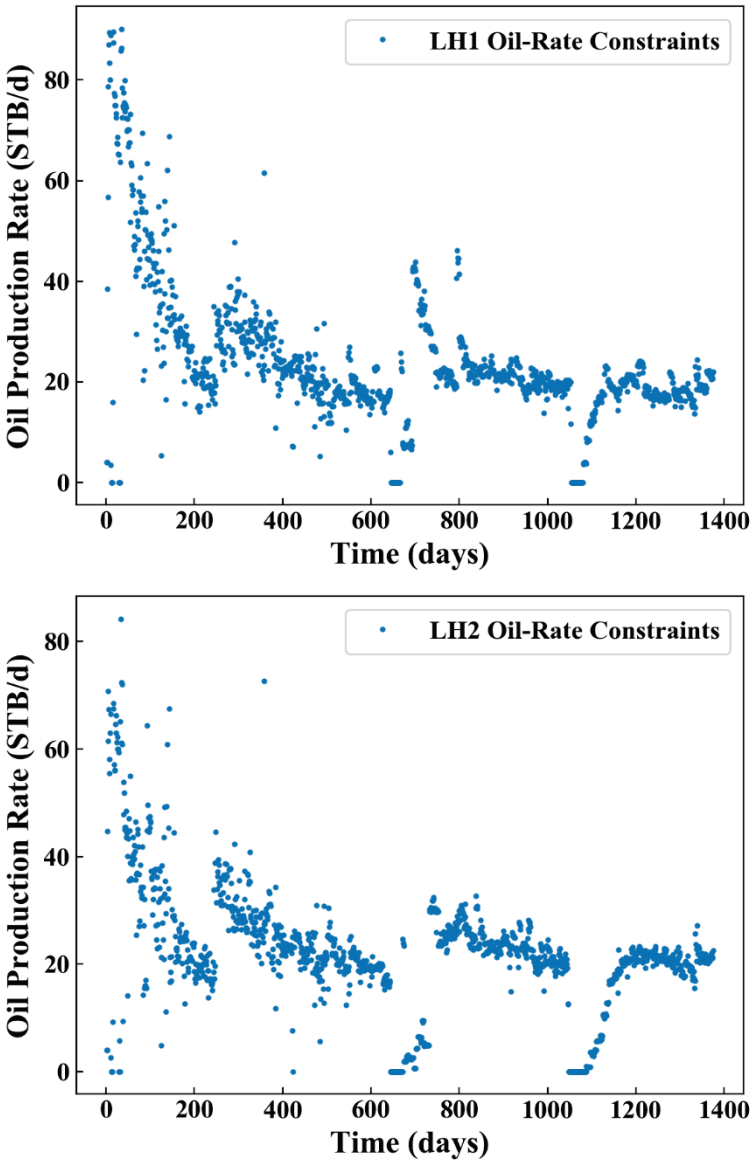

Figure 4.4 Produced-oil rate constraints for simulating production from wells LH1 and LH2.

Adding uncorrelated Gaussian random noise to the true-data points generates synthetic-data points. The noise has zero mean and a standard deviation of 1% of the true

data-point value. An example of a plot of the generated synthetic data against the true simulation output is shown in **Figure 4.5**.

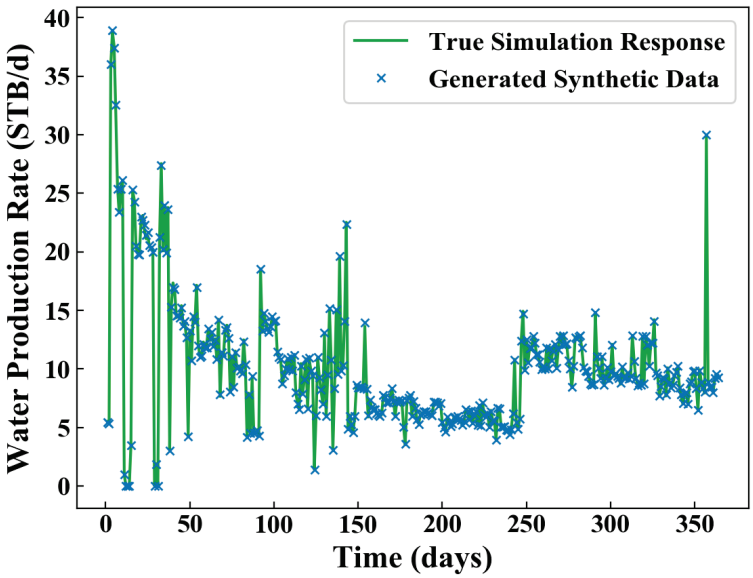

Figure 4.5 True vs Synthetic first-year data for LH2 water production.

4.3 HISTORY-MATCHING STUDY DESIGN

This section describes the conditions and objectives of the history-matching study. The conditions include the choice of history-matching parameters and their assessed prior. We also formulate the misfit-error objective function and define the selection criteria.

4.3.1 Uncertain Parameters

In this study, we use 20 uncertain parameters for the history-matching problem. Fracture geometries are assumed to be exactly known as prior information. Uncertainty is assumed to lie only in SRV permeability and initial saturation of SRV and FRAC regions. In addition to 6 parameters that describe absolute permeability and initial saturation (**Table 4.5**), 14 other parameters are set up to tune the relative permeability curves for FRAC and

SRV regions (**Table 4.6**). These parameters are used to construct the two-phase relative permeability curves for water/oil and oil/gas. All the 20 parameters may vary in a continuous manner on a prior real-number range. The prior probability density function (PDF) is uniform, which is often the case for practical problems with limited available information.

Uncertain parameter	Unit	Base Case	Minimum	Maximum
LH1 SRV permeability	md	0.0008	0.0005	0.01
LH1 SRV initial water saturation	-	0.3	0.25	0.5
LH1 FRAC initial water saturation	-	0.3	0.25	0.6
LH2 SRV permeability	md	0.0008	0.0005	0.01
LH2 SRV initial water saturation	-	0.3	0.25	0.5
LH2 FRAC initial water saturation	-	0.3	0.25	0.6

Table 4.5 Primary uncertain parameters for the synthetic problem. Each parameter varies continuously within a uniform prior distribution.

Keyword	Base	Min	Max	Keyword	Base	Min	Max
swcon	0.0	0.0	0.1	no	2.0	1.0	4.0
Iswcrit	0.35	0.0	0.4	soirg	0.0	0.0	0.1
soirw	0.0	0.0	0.1	Isorg	0.0	0.0	0.1
Isorw	0.02	0.0	0.2	sgcrit	0.2	0.0	0.2
krocw	1.0	0.8	1.0	krgcl	1.0	0.8	1.0
krwiro	1.0	0.8	1.0	nog	2.0	1.0	4.0
nw	3.0	1.0	4.0	ng	3.0	1.0	4.0

Table 4.6 Set of secondary uncertain parameters used to vary relative permeability for SRV and FRAC regions. All parameters have uniform priors.

4.3.2 Study Objective

The starting point is an uninformed base-case model that produces substantial mismatch to the observed synthetic data. The goal is to run an AHM study with the objective of minimizing a global history-matching error. The global history-matching error is calculated by averaging the errors for bottom-hole pressure, cumulative-gas and -oil productions for wells LH1 and LH2. Observed oil rates are enforced as the simulation constraints. For global error calculation, each error type is weighted equally.

History-matching errors are only calculated for the first year of production (365 days of history). From all the generated parameter states, a candidate must satisfy the following criteria for it to be selected:

- Bottom-hole pressure relative error < 5%
- Produced-cumulative water relative error < 5%
- Produced-cumulative gas relative error < 1%

4.3.3 Choice of Sampling Algorithms

The same history-matching study with the same objectives is repeated five times, each with a different sampling algorithm. For comparison, we implement two Bayesian-inversion methods, in addition to DECE method, and two settings of PSO. The first Bayesian sampler is based on building a proxy, based on which, only certain candidates are run on a simulator. The second Bayesian sampler is based on Metropolis-Hastings MCMC method.

We are interested in comparing the performance of different algorithms for this particular case. The following metrics could be useful to quantify the performance of different methods:

- Total number of simulation-runs
- The number of accepted models per number of runs
- Marginal posterior parameter distribution
- Distribution and range of production forecasts

To reduce the errors that may arise from random artifacts, the same random seed (6232019) was used for all the generators for all numerical experiments presented in the chapter.

4.4 RESULTS AND DISCUSSION

In this section we present and discuss results from all the numerical experiments. We first present detailed AHM study with Bayesian Algorithm I using different controlled history-matching periods. We follow with results from three other algorithms. Finally, we conclude with a benchmarking-comparison of all AHM algorithms.

4.4.1 Bayesian Algorithm I

Now we present and discuss history-matching results obtained by using Bayesian Algorithm I. This method is of special interest to us, and thus, its results are described in more detail.

4.4.1.1 History-Matching Quality Results

With the total number of full numerical simulations limited to 810, this method generates 68 models that satisfy the selection criteria (**Figure 4.6**). The selected models have a global relative error ranging from 1.3% to 3.3%. Provided that the original data includes random noise, it is not surprising a global error smaller than 1% is not achieved.

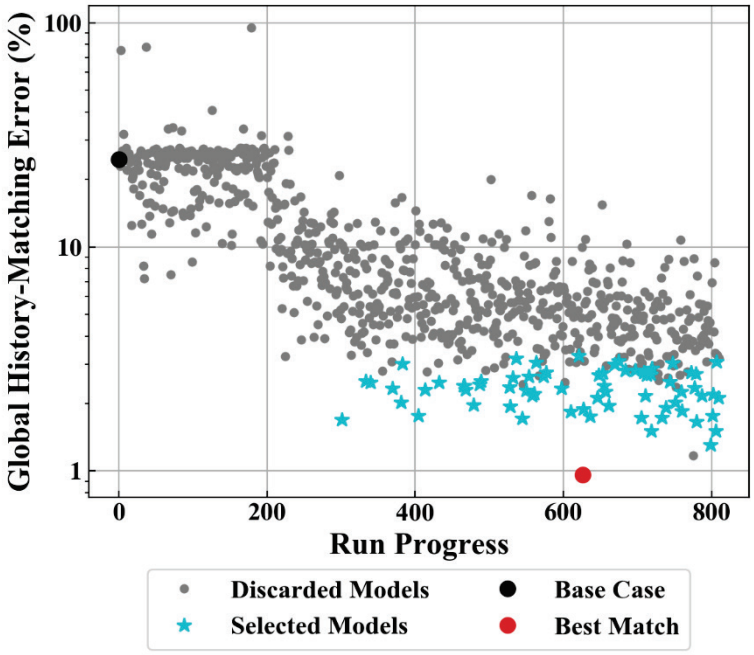

Figure 4.6 History-matching quality progress vs runs sequence for the Bayesian method 1 with PAR covering first 1 year of observed data.

Results suggest that, even with relatively large number of parameters and a multi-level objective function, the method is capable of producing adequate history-matching quality. **Figure 4.7** and **Figure 4.8** contain series of plots of pressure and rates against simulation times for the two wells. In this experiment, only first-year data points contribute to formulating the objective function. A visual inspection of the plots indicates that the selected ensemble closely matches the observed data.

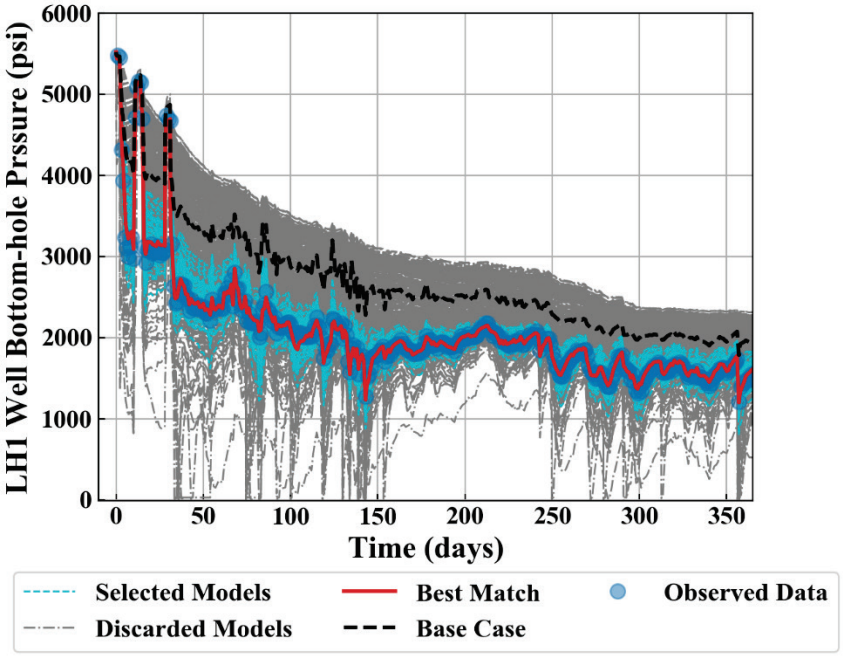

(a)

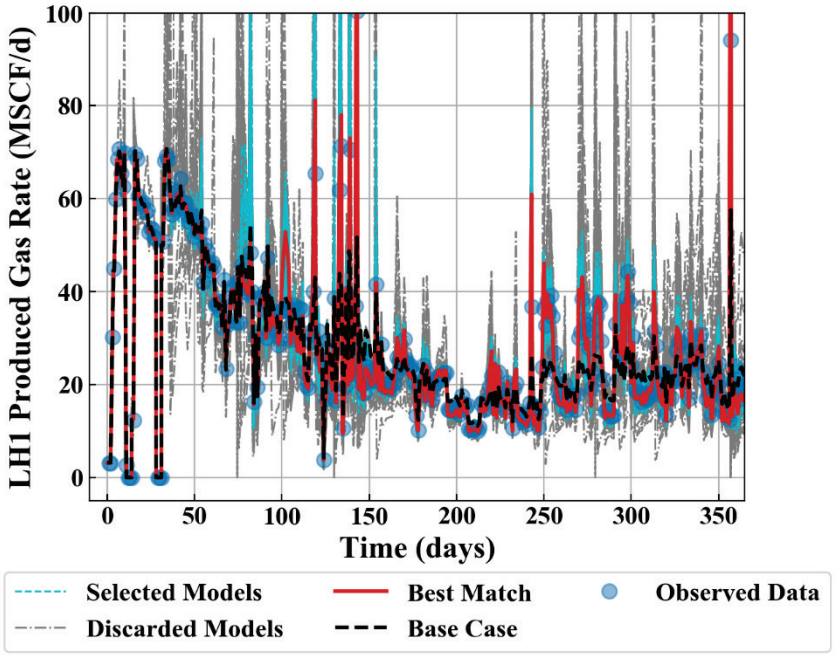

(b)

Figure 4.7: Continued next page.

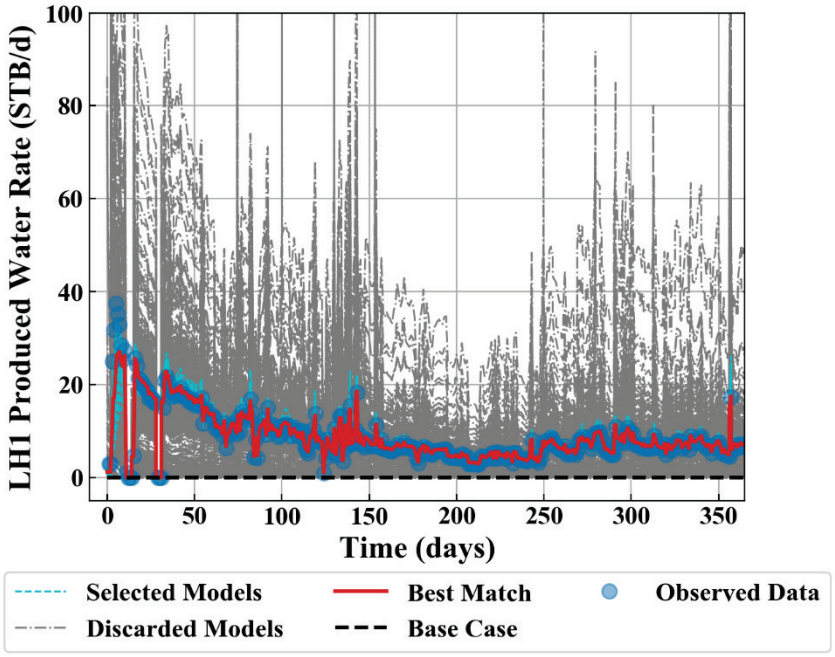

(c)

Figure 4.7 Well LH1 history-matching results for (a) bottom-hole pressure, (b) produced-gas rate, and (c) produced-water rate. History matching is performed for the earliest 365 data-points.

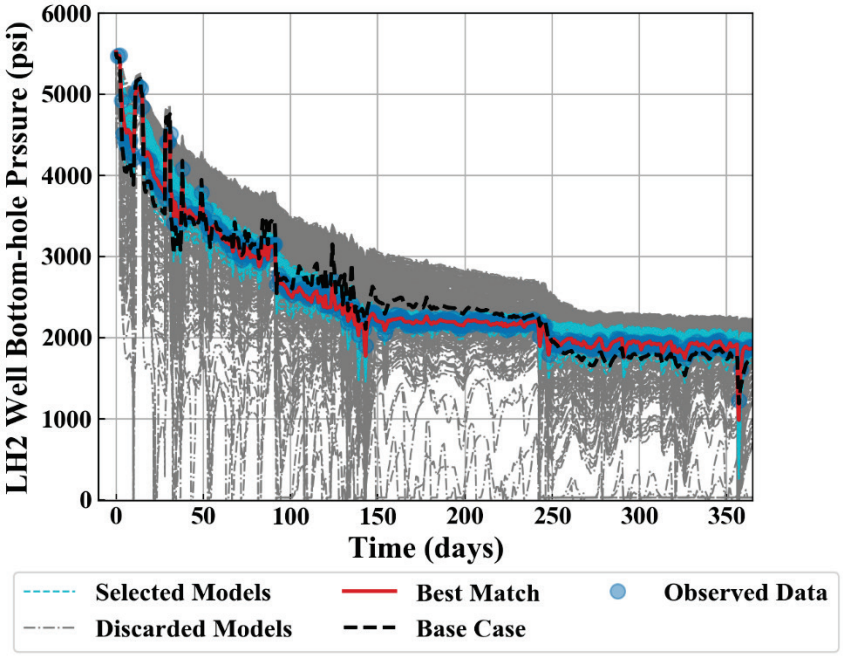

(a)

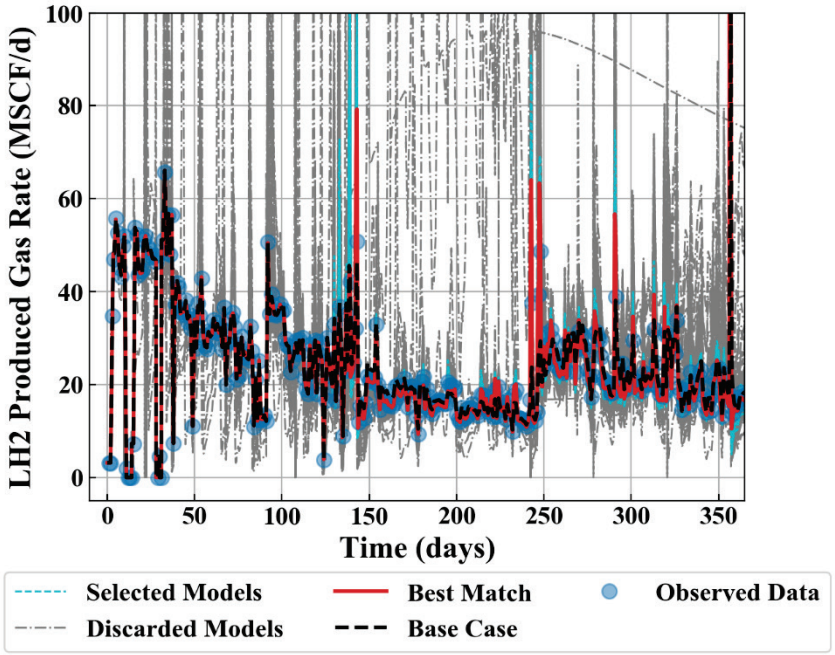

(b)

Figure 4.8: Continued next page.

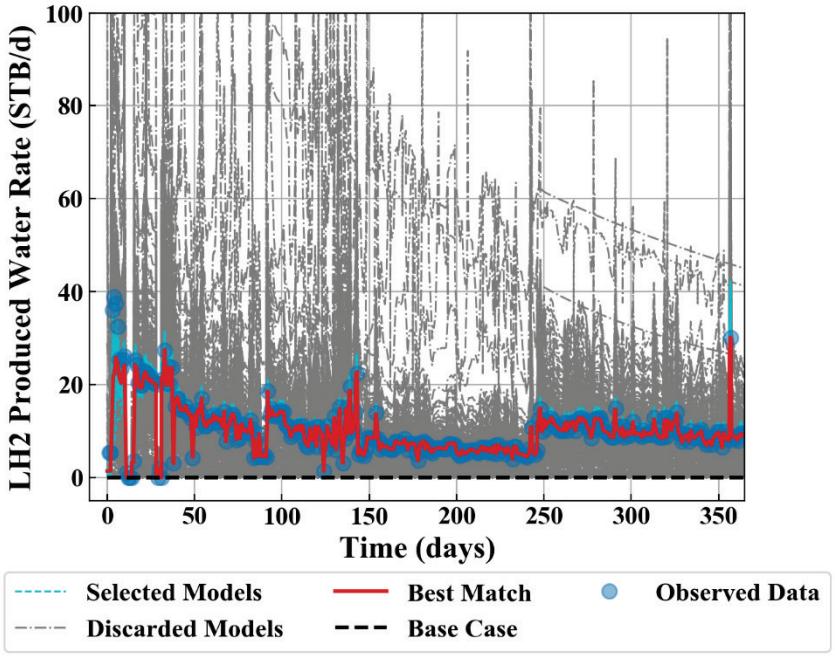

(c)

Figure 4.8 Well LH2 history-matching results for (a) bottom-hole pressure, (b) produced-gas rate, and (c) produced-water rate. History matching is performed for the earliest 365 data-points.

4.4.1.2 Validation beyond History-Matching Period

The decision of selecting only the first year of data as history-matching period is intentional. This practice would allow us to assess the performance of the AHM-obtained models to predict observations beyond history-matching period, especially, since real field history matching is often practiced over green fields with less than few years of history. **Figure 4.9** and **Figure 4.10** display plots of the pressure, gas and water productions extending over the entire observable period for the previously presented results.

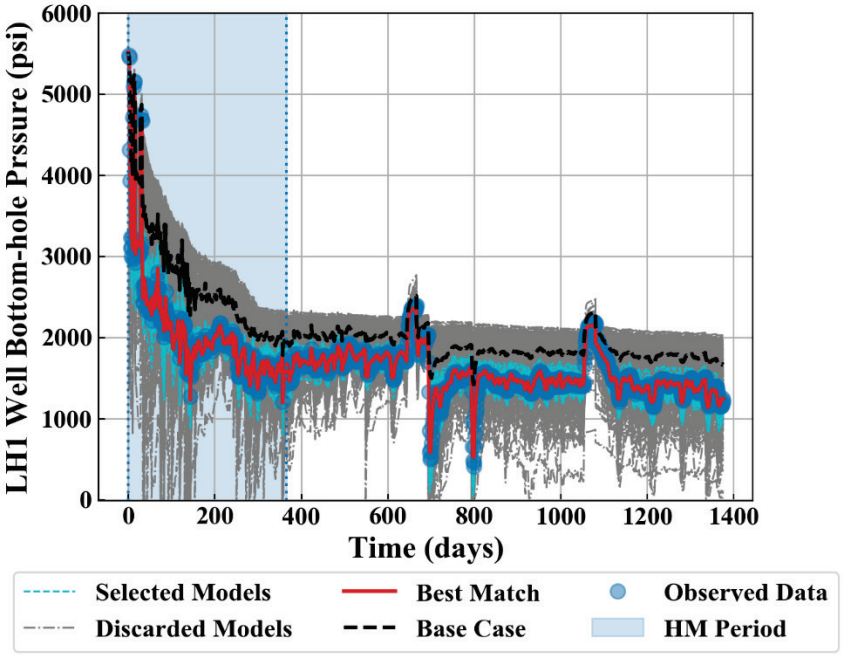

(a)

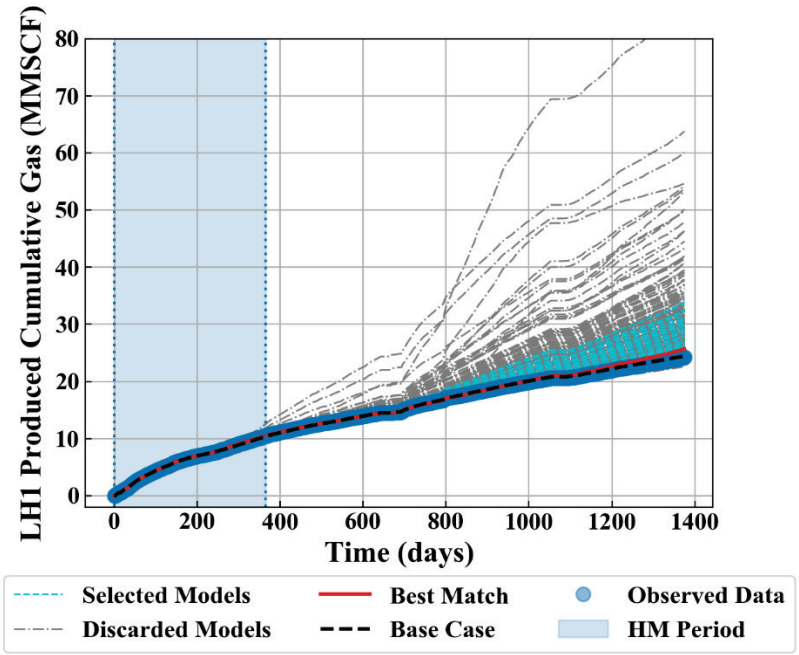

(b)

Figure 4.9: Continued next page.

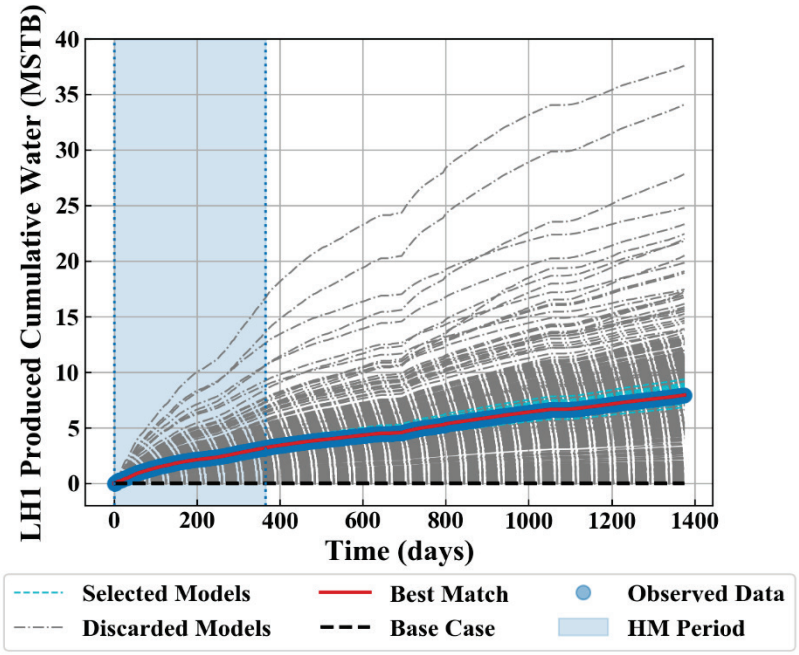

(c)

Figure 4.9 Extending well LH1 history-matching results beyond history-matching period for (a) bottom-hole pressure, (b) produced cumulative gas, and (c) produced cumulative water.

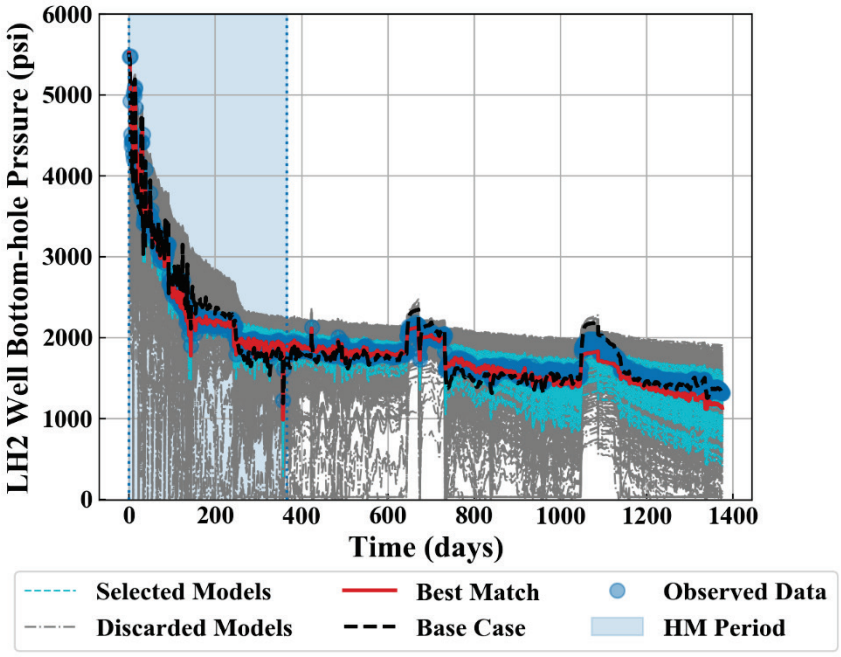

(a)

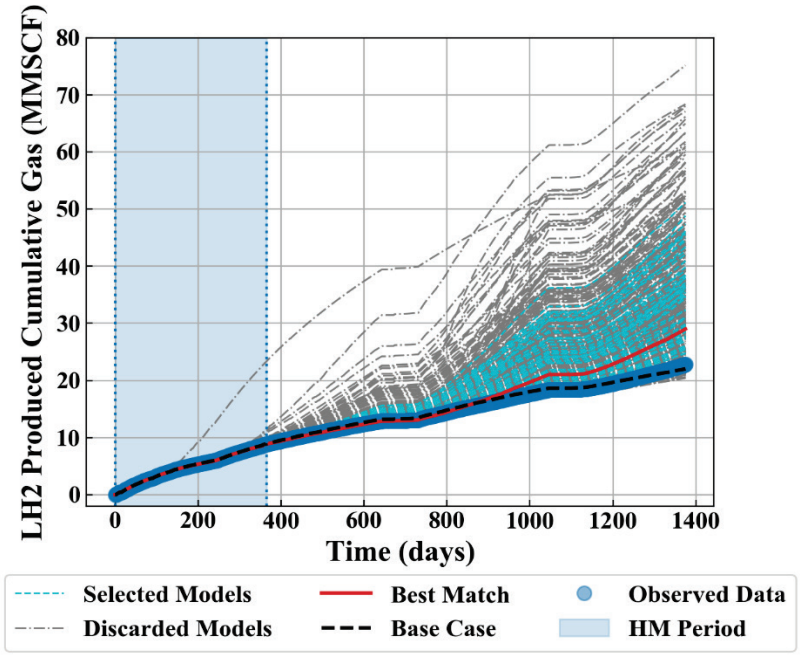

(b)

Figure 4.10: Continued next page.

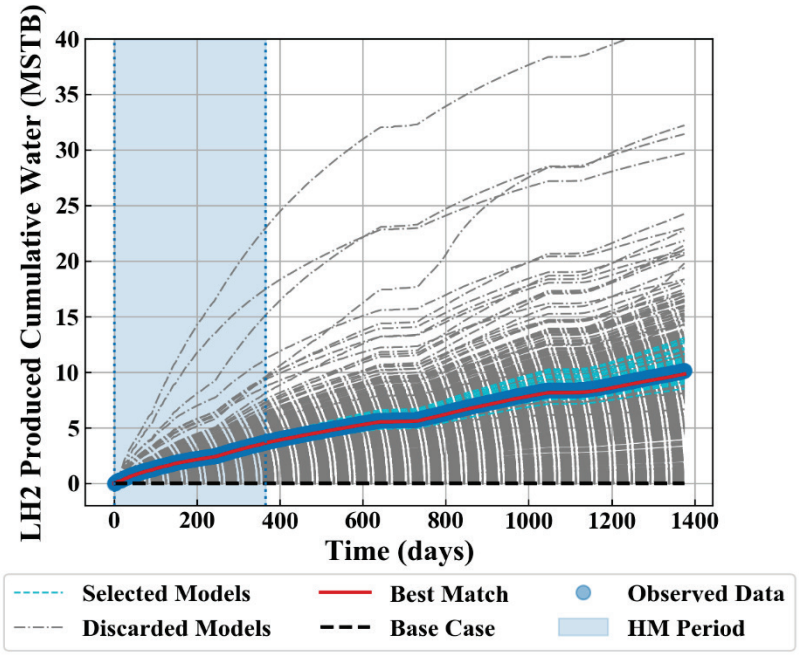

(c)

Figure 4.10 Extending well LH2 history-matching results beyond history-matching period for (a) bottom-hole pressure, (b) produced cumulative gas, and (c) produced cumulative water.

One observation is that gas production diverges substantially from the truth, whereas pressures and water rates don't change as much. Additionally, results show larger deviation from the truth for LH2 results than for LH1 results. The reason for that might relate to the fact that the objective function is a global average of the errors calculated for each well for each data type. However, from inspecting a breakdown of the errors, we find no strong bias or compromise towards one specific error type (**Figure 4.11**). In fact, errors recorded for LH2 appear to be smaller in magnitude than for LH1.

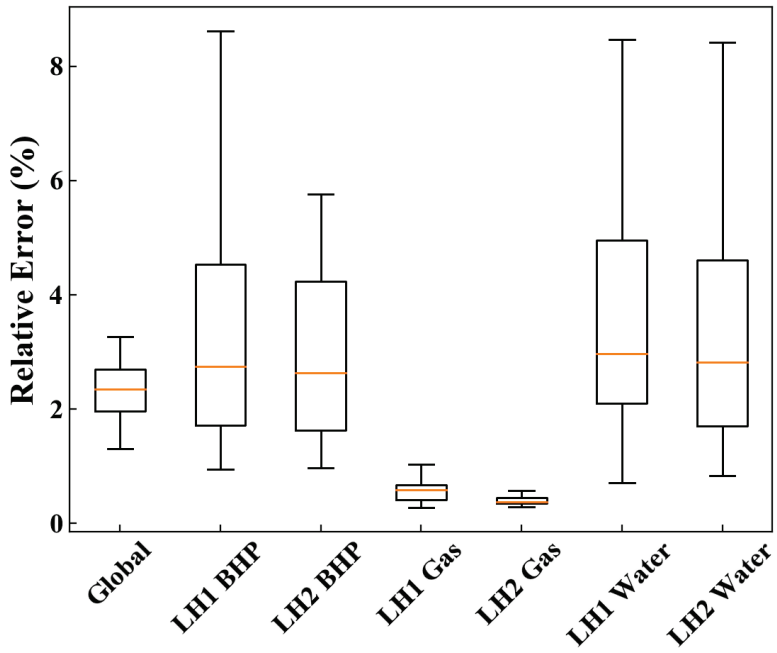

Figure 4.11 Boxplots showing the distribution of individual errors for the selected sample of models. Global error is fragmented into individual relative errors; each corresponding to a specific well and data type.

Another more likeable explanation could be that some influential parameters, such as SRV permeability and gas relative permeability, might have wider posterior distribution for LH2 than for LH1. A wide range of SRV permeability might, in this case, produce a quality match for the history-matching period. However, such a large band of values may also cause large deviations in the longer term, especially after reservoir becomes under saturated. In the next section we present and analyze the marginal posterior distribution for uncertain parameters.

4.4.1.3 Parameter Marginal Posterior Distributions

The distribution for uncertain parameters of the selected models is presented here in **Figure 4.12**, **Figure 4.13**, **Figure 4.14**, and **Figure 4.15**. In all figures, the y-axis is automatically scaled to the largest probability. The range of x-axis for each distribution is the same as the prior bounds for the corresponding parameter. The more influential a parameter is, the narrower its posterior distribution becomes. If a parameter has negligible influence on the likelihood, a Bayesian algorithm should converge to the prior if it is allowed to run infinitely. Therefore, we can infer the sensitivity of each parameter by examining the shape of its posterior.

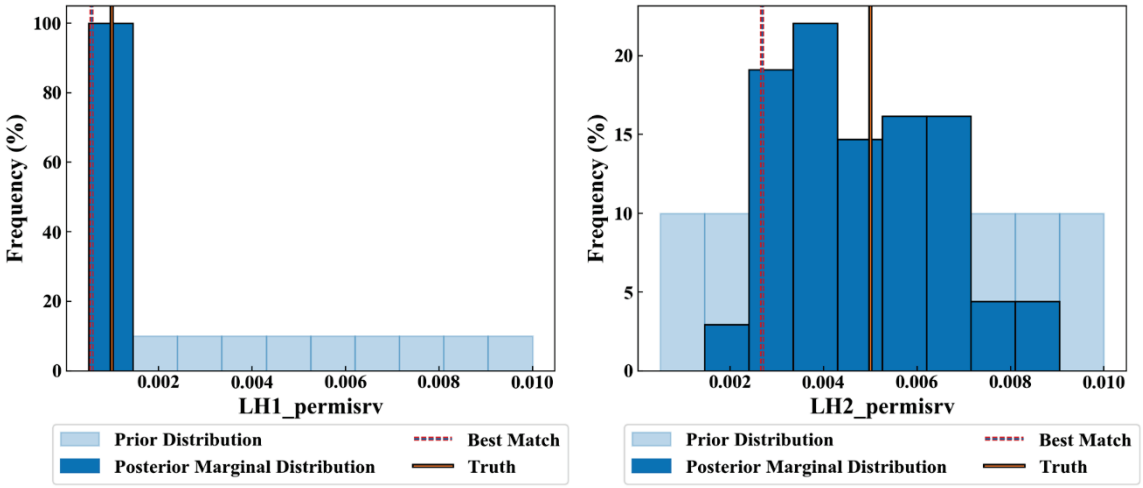

Figure 4.12 Marginal posterior distribution for SRV permeability for well LH1 (left) and LH2 (right).

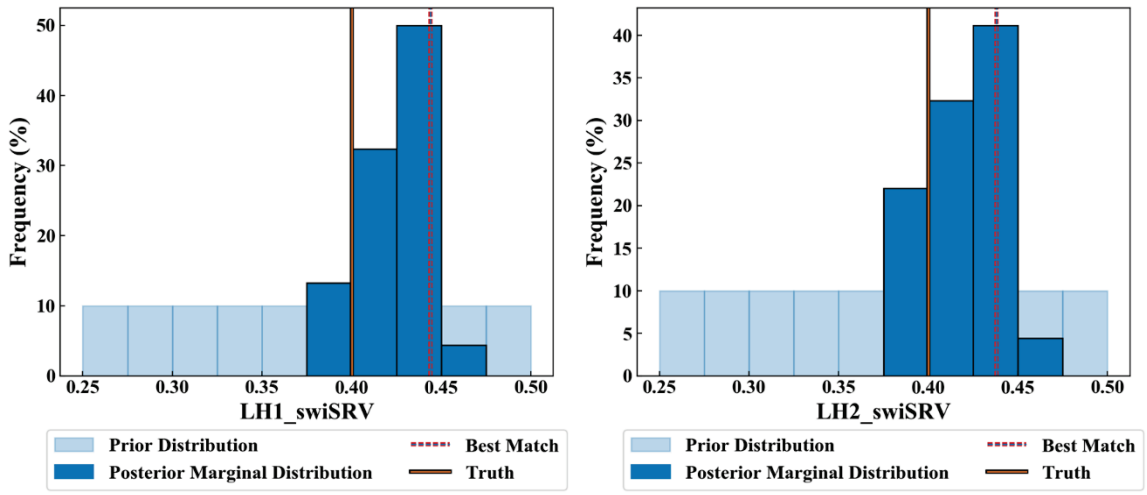

Figure 4.13 Marginal posterior distribution for SRV initial water saturation for well LH1 (left) and LH2 (right).

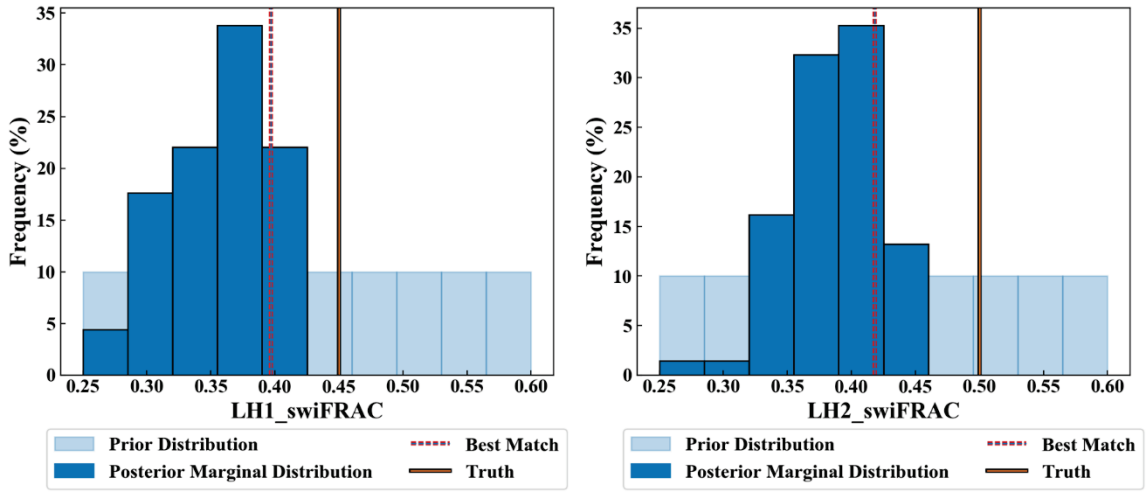

Figure 4.14 Marginal posterior distribution for SRV initial water saturation for well LH1 (left) and LH2 (right).

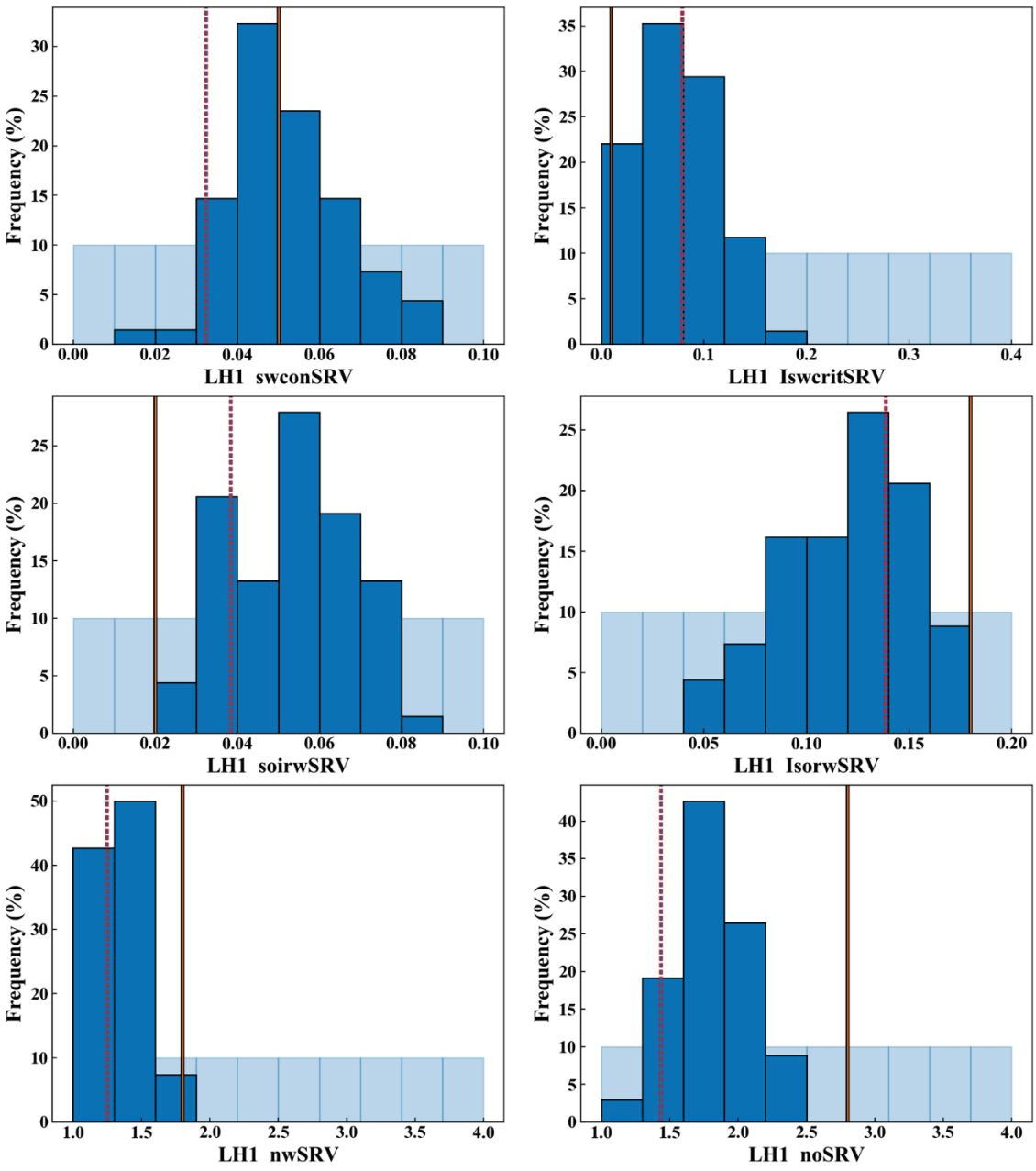

Figure 4.15 Marginal posterior distribution for SRV and FRAC relative permeability parameters (I).

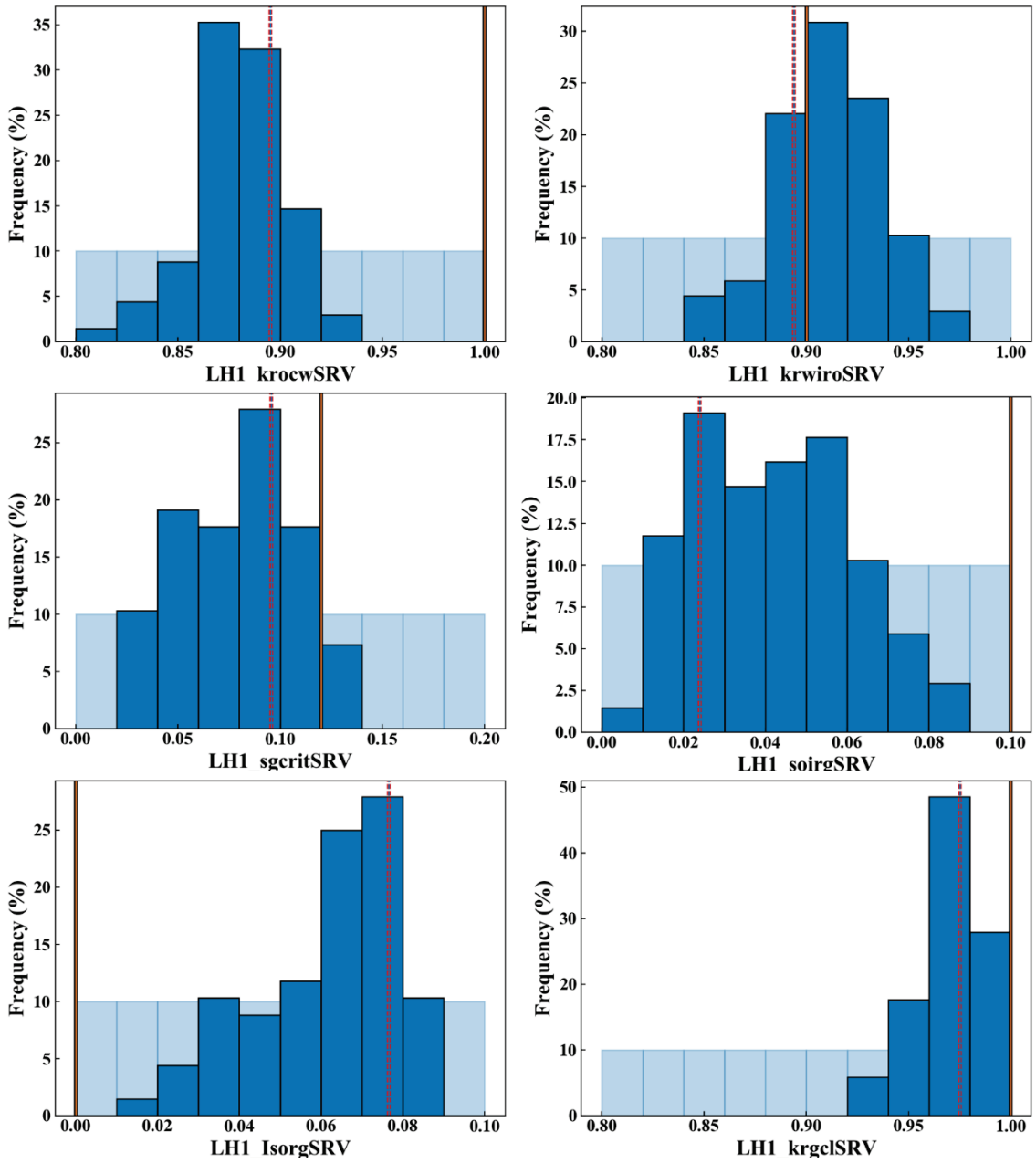

Figure 4.16 Marginal posterior distribution for SRV and FRAC relative permeability parameters (II).

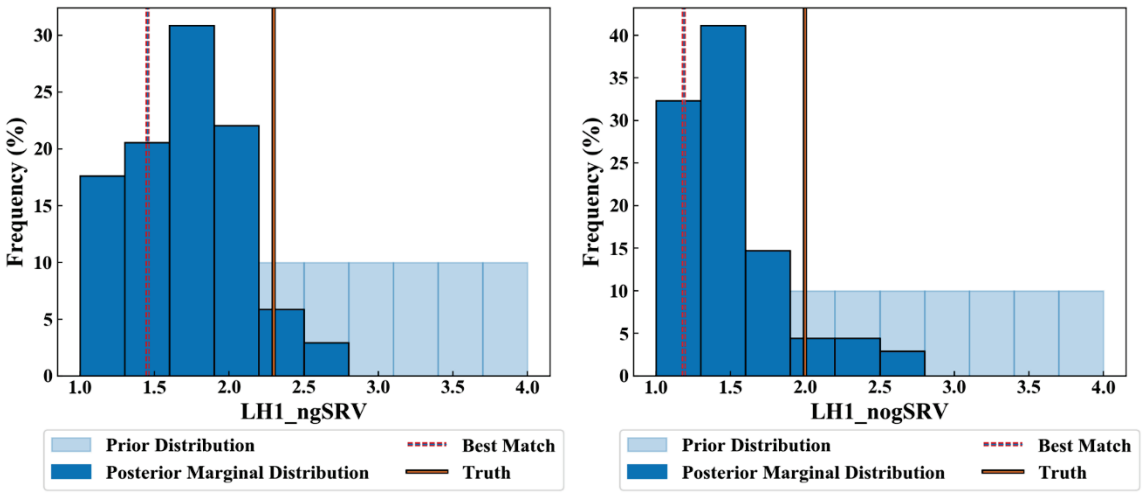

Figure 4.17 Marginal posterior distribution for SRV and FRAC relative permeability parameters (III).

LH1 SRV permeability appears to be very influential to the likelihood, whereas LH2 SRV permeability effect is more subtle (see **Figure 4.12**). P10 and P90 for LH1 SRV permeability are 0.0005 and 0.0009 md respectively. The gap between P10 and P90 is larger for LH2 SRV permeability and ranges from 0.0029 to 0.007 md. Although not affecting history-matching quality, such large variation in SRV permeability is a potential cause of the larger discrepancies in the prolonged model validation period (compare **Figure 4.9.a** and **Figure 4.9.b** with **Figure 4.10.a** and **Figure 4.10.b**).

As expected, initial saturations arise as important history-matching parameters. SRV posterior saturations have narrower ranges than the FRAC's, suggesting that SRV volume is more influential to the likelihood than FRAC volume (compare **Figure 4.13** to **Figure 4.14**). One observation is that the posterior FRAC initial saturation does not enclose the truth and skews to smaller values in the range (**Figure 4.14**). However, the general trend of smaller-than-truth FRAC saturations seems to be offset by another general

trend of larger-than-truth SRV saturations (compare between the posterior range and the truth in **Figure 4.13**). This finding highlights the non-linearity nature of the problem. The likelihood seems to be more sensitive to the interaction among the SRV, FRAC saturations (and possibly relative permeability curves) than to each individual saturation. A good modeling practice, perhaps, might be to assume the same initial water saturation in a fracture block and its adjacent SRV.

Similarly, the posteriors for several relative-permeability parameters exhibit separation from the truth. In some cases, the posterior distribution does not even enclose the truth (e.g., n_o in **Figure 4.17**). The difference could be produced by the problem's non-linearity, although it could also be a random sampling artifact. If some of the parameters are combined into "principal parameters", the resulting distribution could get narrower and closer to the truth. For example, connate water saturation (swcon) can be added to incremental water saturation (Iswcrit) to form the critical water saturation (swcrit). Likewise, residual oil saturation (sorw) can be calculated by summing soirw and Isorw. The resulting posteriors are significantly narrower than those of their constituent parameters (**Figure 4.18**).

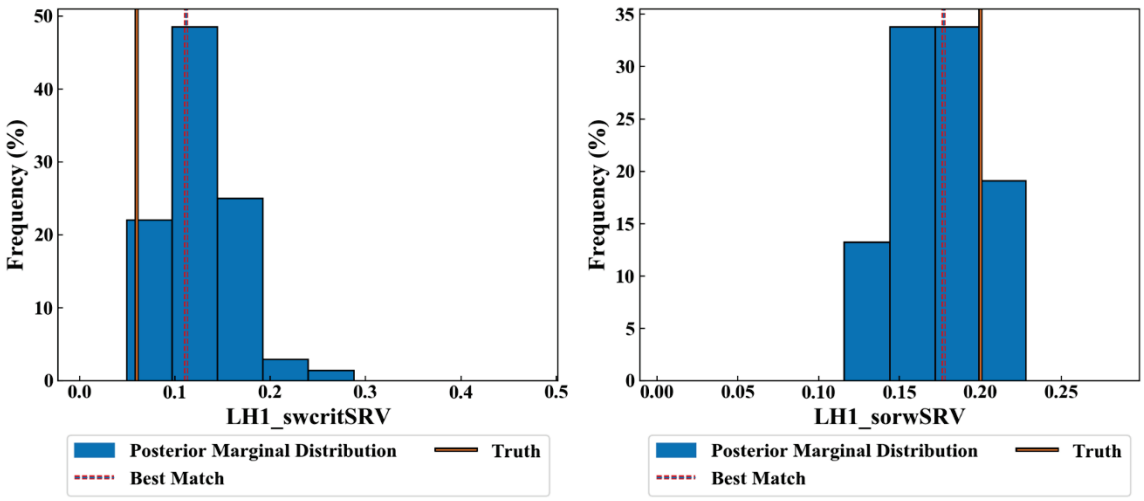

Figure 4.18 Marginal posterior distribution of end point saturations (critical water and residual oil). y-axis is scaled to the largest probability and x-axis is scaled to the full range of the priors.

Remarkably, the dissimilarity between the posterior and the truth is smaller for the keywords that define Brooks-Corey water-phase curve (e.g., contrast between n_o and n_w in **Figure 4.15**, and between K_{rocw} and K_{rwiro} in **Figure 4.16**). This might be because of the fact that the water curve has larger influence on the likelihood than all the other curves. During history-matching period, fluid flow is dominantly two-phase with oil rates controlled by simulation constraints. Hence, water-phase relative permeability is key for matching observed water-phase rates.

In essence, the noticeable variance in relative-permeability parameters reflects the fact that there is a stack of multiple relative-permeability curves that achieve high-quality history matching. The resulting stack of acceptable curves is shown in **Figure 4.19**. It is important to note that each curve of the selected set is not standalone. Each curve becomes

valid only when paired with the right combination of other parameters. The non-linear interaction between relative permeability and other uncertain parameters, particularly initial saturations, is important. Among all the curves, the water curves establish closest match to the truth. This further supports the finding that water relative permeability is an important contributor to the likelihood for this problem.

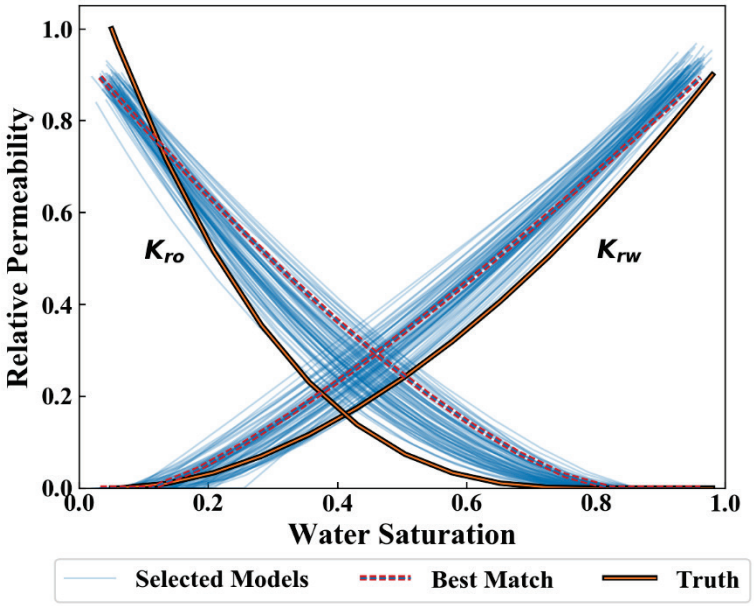

(a)

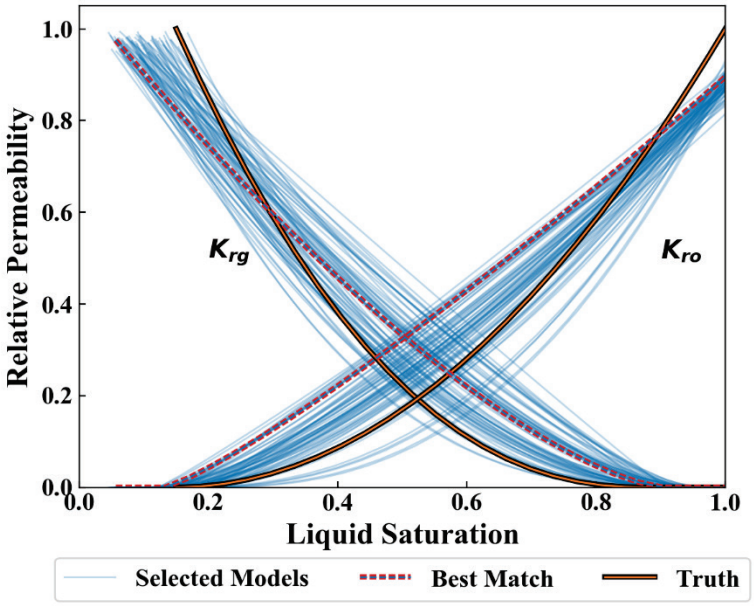

(b)

Figure 4.19 Relative permeability curves for selected models vs truth for (a) oil/water system and (b) gas/liquid system.

4.4.1.4 Production Forecasting

Production forecasting for the selected models is probabilistically estimated over a total period of 30 years. After the initial period of 1375 days, the simulations are switched to the forecasting constraints: 25 STB/d maximum oil-production rate and 800 psi minimum bottom-hole flowing pressure, for both wells. Oil and gas production forecasts are plotted in **Figure 4.20** and **Figure 4.21**. Here, the estimated ultimate recovery (EUR) is equivalent to the cumulative oil production after 30 years. Recall that in our case, we consider only a portion of two long horizontal laterals. Hence, EUR values here represent only a portion of what the reader would predict from typical wells in a real field scenario. However, the EUR values presented here are scalable to the size of the whole laterals and are indeed useful for comparisons.

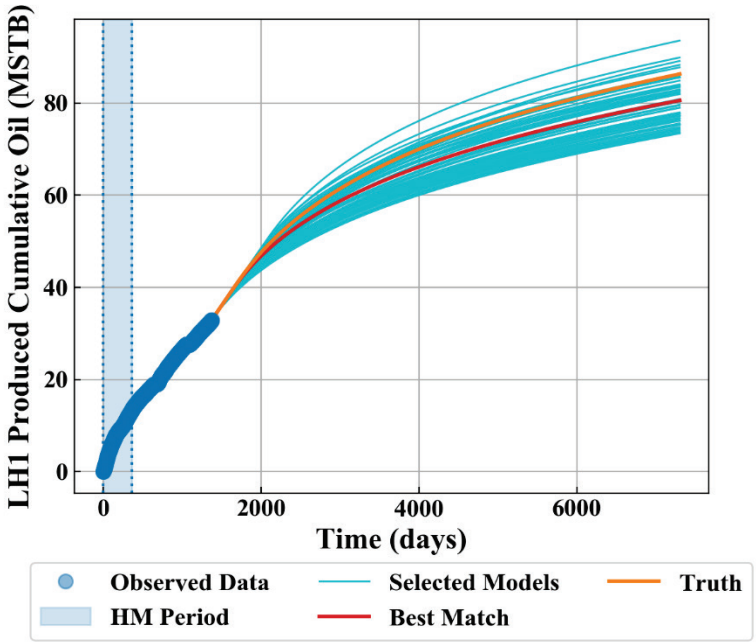

(a)

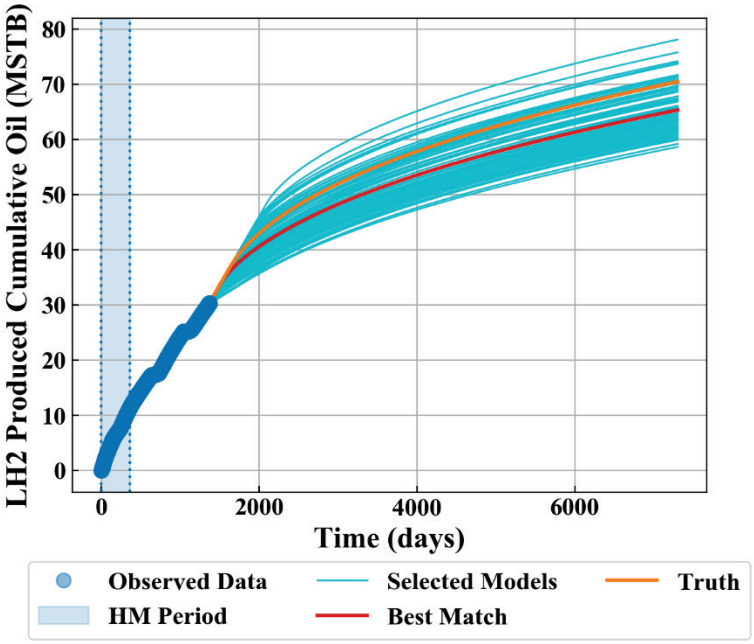

(b)

Figure 4.20 Probabilistic Forecast of oil production for 68 selected models for the two wells.

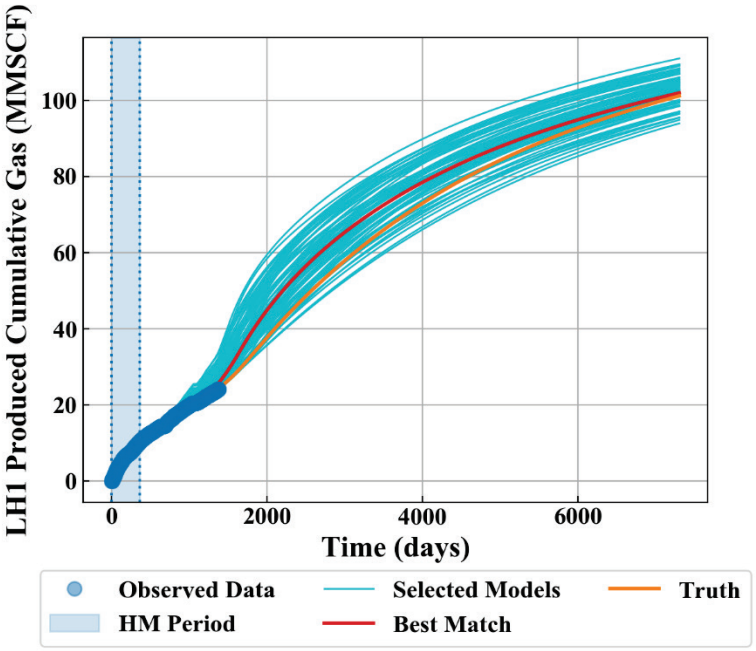

(a)

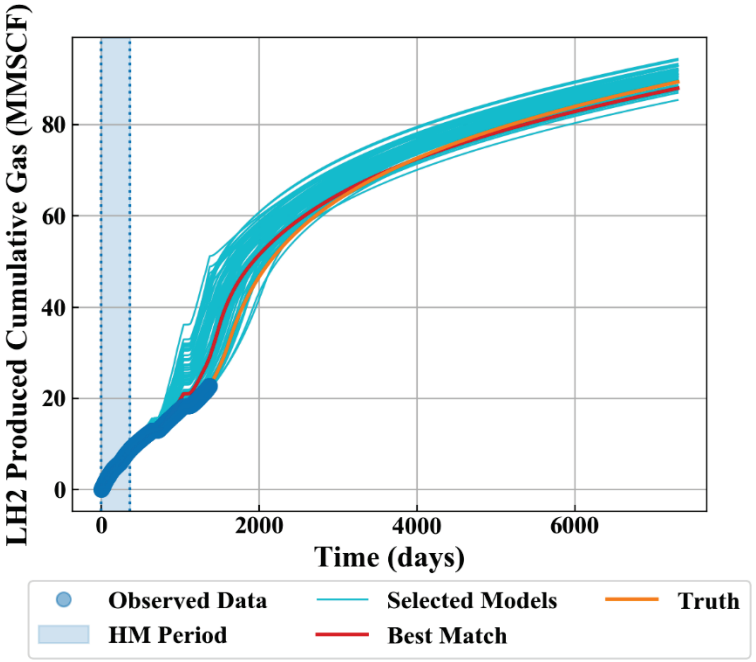

(b)

Figure 4.21 Probabilistic Forecast of gas production for 68 selected models for the two wells.

The distribution of the forecasted EUR can be compared with the truth's EUR. Note that, since the problem is entirely synthetic, the prior and the likelihood are well known. For a real field problem, the associated modeling inadequacies and information uncertainty would affect the likelihood and prior. Therefore, here we are able to use the EUR for the truth as a benchmark to assess the method's efficiency.

The truth's EUR falls within the algorithm-predicted uncertainty range for the two wells. For both wells, it appears that the forecast is slightly pessimistic, with a larger portion of the distribution below the truth's EUR. Results for cumulative water production are not presented here but they show the opposite trend.

4.4.2 Extending History-Matching Period

Motivated by the noticed deviation of rates and pressure at times beyond history-matching period, we run two additional experiments: one covering the first two years of observed data (Case-2); and another covering the first 3-year period (Case-3). For both studies, the selection criteria of solution are the same as the 1-year study (Case-1). It is important to note that the calculated objective function is automatically scaled to the range of data and averaged over the quantity of data. This scaling method guarantees production of relative errors that are comparable, although not 100% equivalent (see one comparison in **Table 4.7**). Thus, adopting the same selection criteria over different sets of data might jeopardize fair comparisons.

Study	Relative Error (%)			
	Global	**BHP**	**Cum Gas**	**Cum Water**
One-year data assimilation	24.52	9.93	0.64	62.99
Two-year data assimilation	24.96	7.00	0.83	67.03
Three-year data assimilation	23.82	6.40	0.96	64.09

Table 4.7 Comparison of scaled global and individual errors calculated for the base case based on the mismatch to three data sets with varying time span.

4.4.2.2 Run Progress

Case-2 yields 38 models that satisfy the criteria, a smaller number than for Case-1 (**Figure 4.20**). This time, the lowest achievable objective-function record is still larger than the previously established records, with a 1.49% relative error recorded for the best match case.

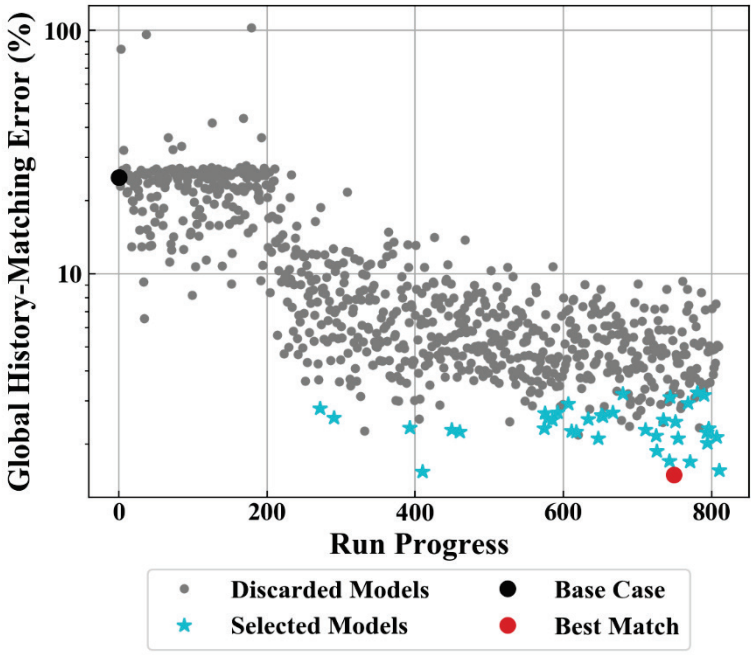

Figure 4.22 History-matching quality progress vs runs sequence for the Bayesian Algorithm I with PAR covering first 2 year of observed data.

Case-3 yields 65 models that satisfy the criteria (**Figure 4.21**). This number is comparable to the number of solutions obtained by Case-1, with 0.86% relative error recorded for the best match case. Note, in **Table 4.7**, Case-2 has the largest relative error for its base case, and thus we are not surprised to find that it also has the largest minimum achievable error compared to all cases. Next, we plot the simulated results against data for the selected models.

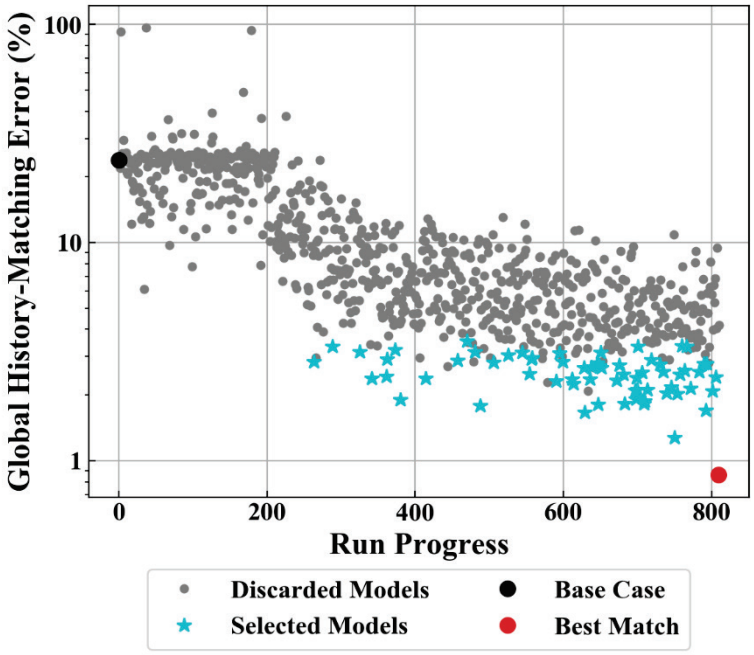

Figure 4.23 History-matching quality progress vs runs sequence for the Bayesian Algorithm I with PAR covering first 3 year of observed data.

4.4.2.3 History-Matching Quality Results

Plots of simulated results against data for one well are summarized in **Figure 4.22** and **Figure 4.23** for Case-2 and Case-3 respectively. Beyond history-matching period, we report smaller deviations from the truth when longer time periods are considered. This finding is particularly pronounced for produced cumulative gas results (contrast **Figure 4.22.b** and **Figure 4.23.b** to **Figure 4.10.b**). This may result from the fact that, during the first year, the reservoir pressure has been mostly larger than bubble-point. Before reaching the bubble-point pressure, fluid flow in the subsurface occurs in two phases, i.e. water and oil. Gas relative permeability would not be important at such fluid-flow condition. However, when longer time periods are considered, the reservoir is allowed to reach

saturation. At saturation condition, the gas phase start to evolve, and flow in the subsurface occurs in three phases. Only then, the gas-phase relative permeability arises as an important history-matching influencer.

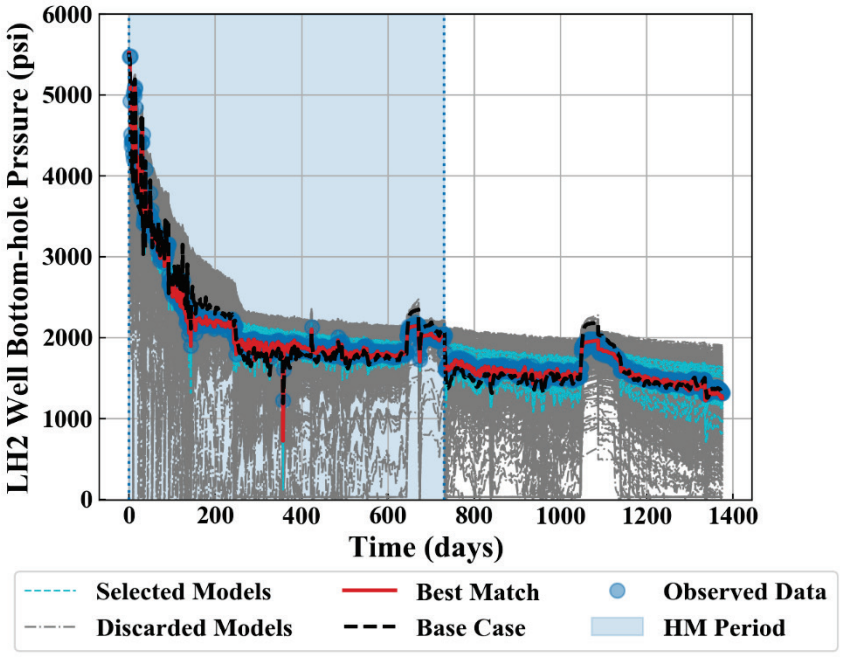

(a)

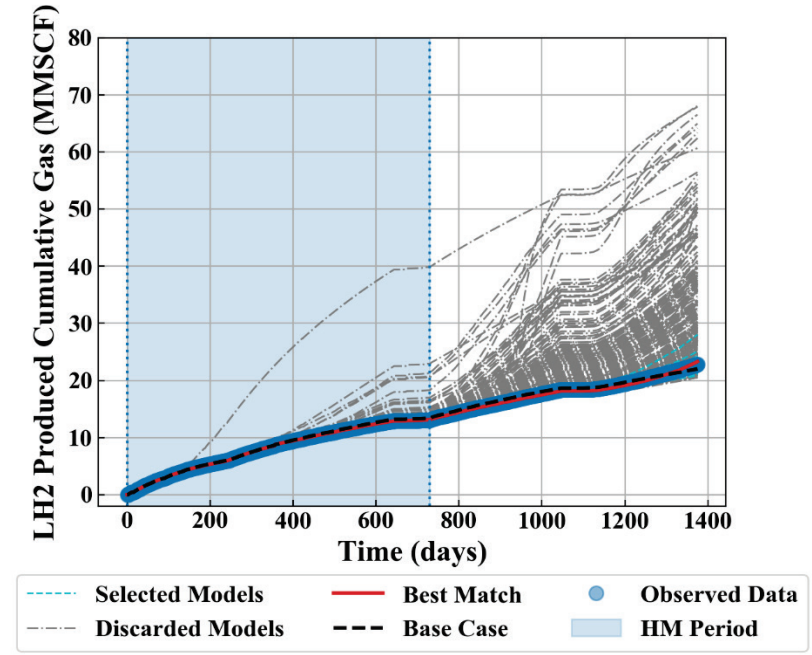

(b)

Figure 4.24: Continued next page.

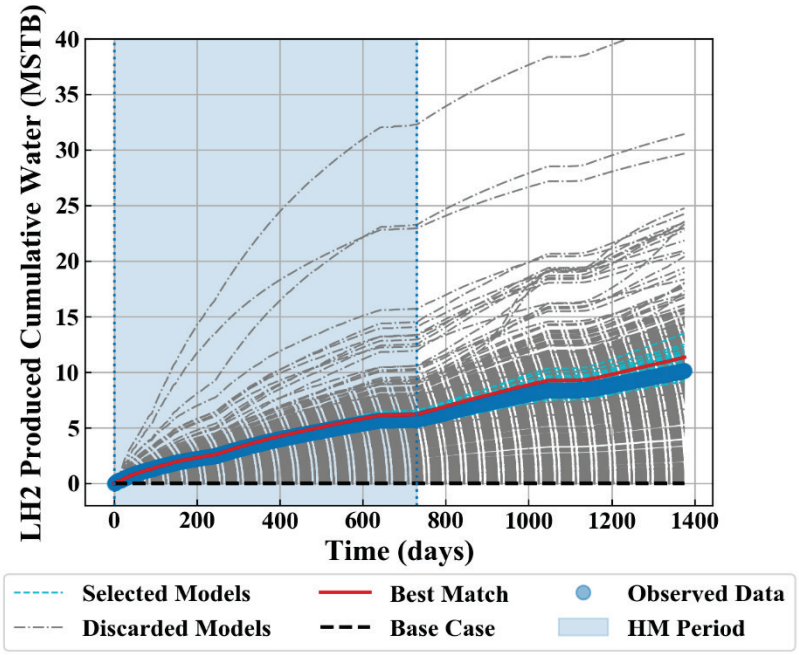

(c)

Figure 4.24 LH2 history-matching results for 2-year data sets of (a) bottom-hole pressure, (b) produced cumulative gas, and (c) produced cumulative water. There are 38 models selected from a total of 810.

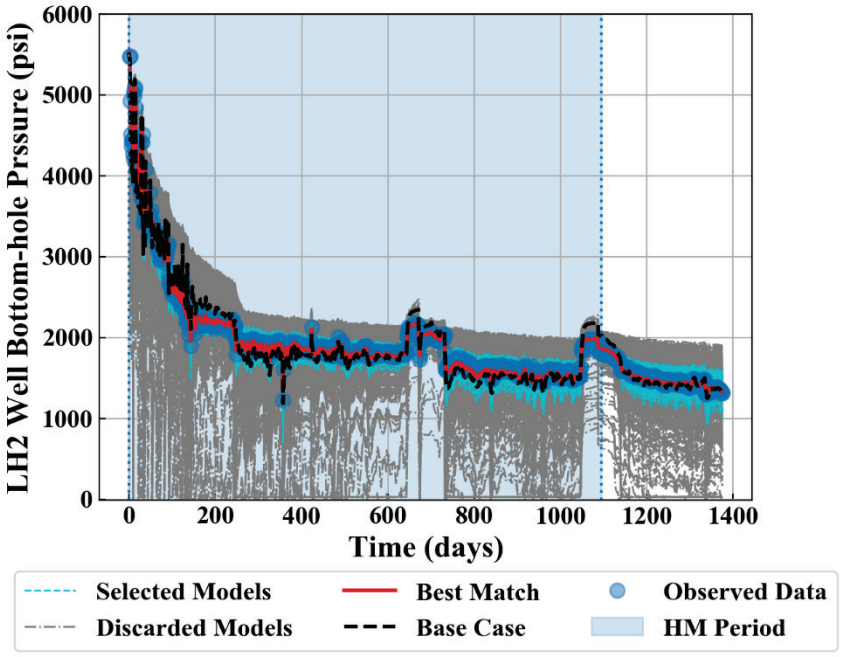

(a)

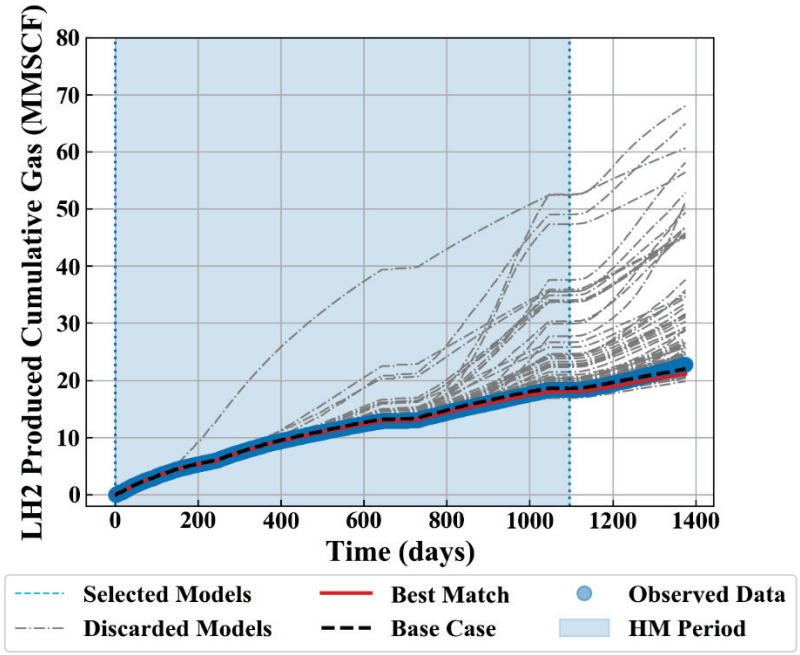

(b)

Figure 4.25: Continued next page.

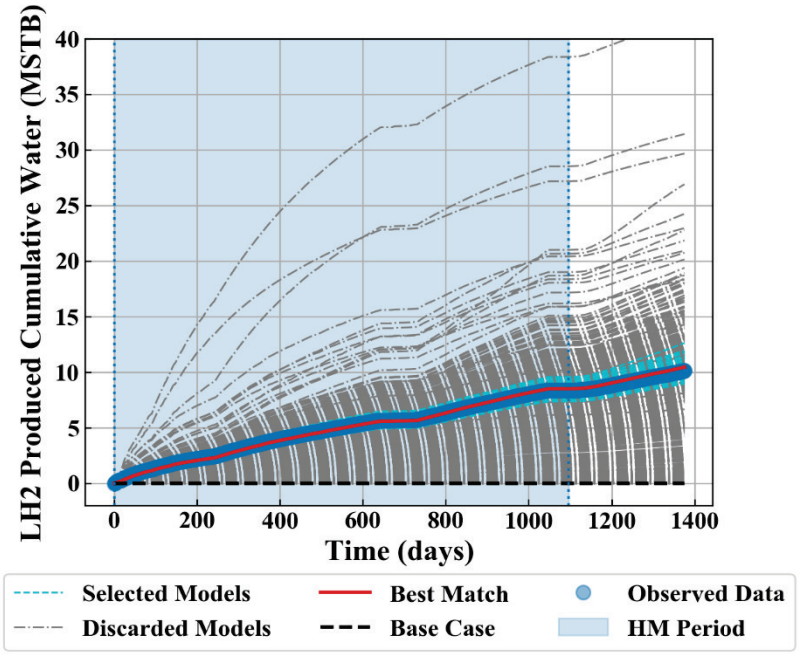

(c)

Figure 4.25 LH2 history-matching results for 3-year data sets of (a) bottom-hole pressure, (b) produced cumulative gas, and (c) produced cumulative water. There are 65 models selected from a total of 810.

4.4.2.4 Parameter Marginal Posterior Distributions

A comparison of the final marginal distribution of the problem's parameters can be summarized in boxplots form (**Figure 4.24**, **Figure 4.25**, and **Figure 4.26**). In these plots, error bars designate the minimum and maximum values, boxes designate the P25-P75 range, and orange lines designate the P50 values. Once again, the x-axis scale is set to the prior range. The comparison shows that considering longer periods of data does not bring the posteriors closer towards the truth. For some parameters, the posterior diverges even further from the truth (e.g., SRV saturations in **Figure 4.24**). When longer time durations are considered, the distribution for LH2 SRV permeability gets narrower. More noticeable

is significant alteration in gas/liquid relative-permeability curve parameters (notice the shift for exponents and end-point saturations in **Figure 4.26**). This highlights the argument that gas relative permeability curve becomes key only after a specific time of the simulation.

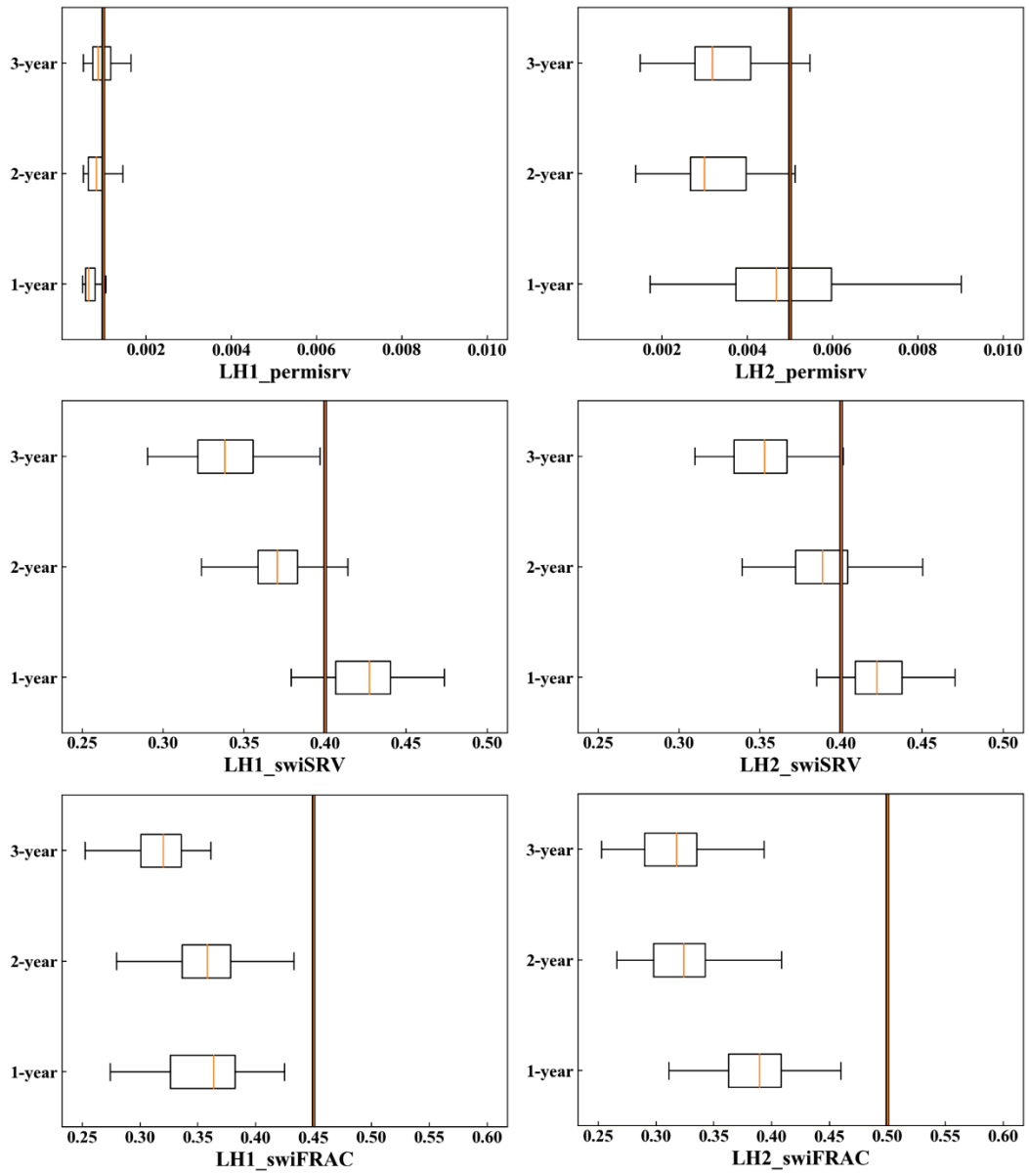

Figure 4.26 Comparison of marginal posterior distributions for the uncertainty parameters for three cases (I).

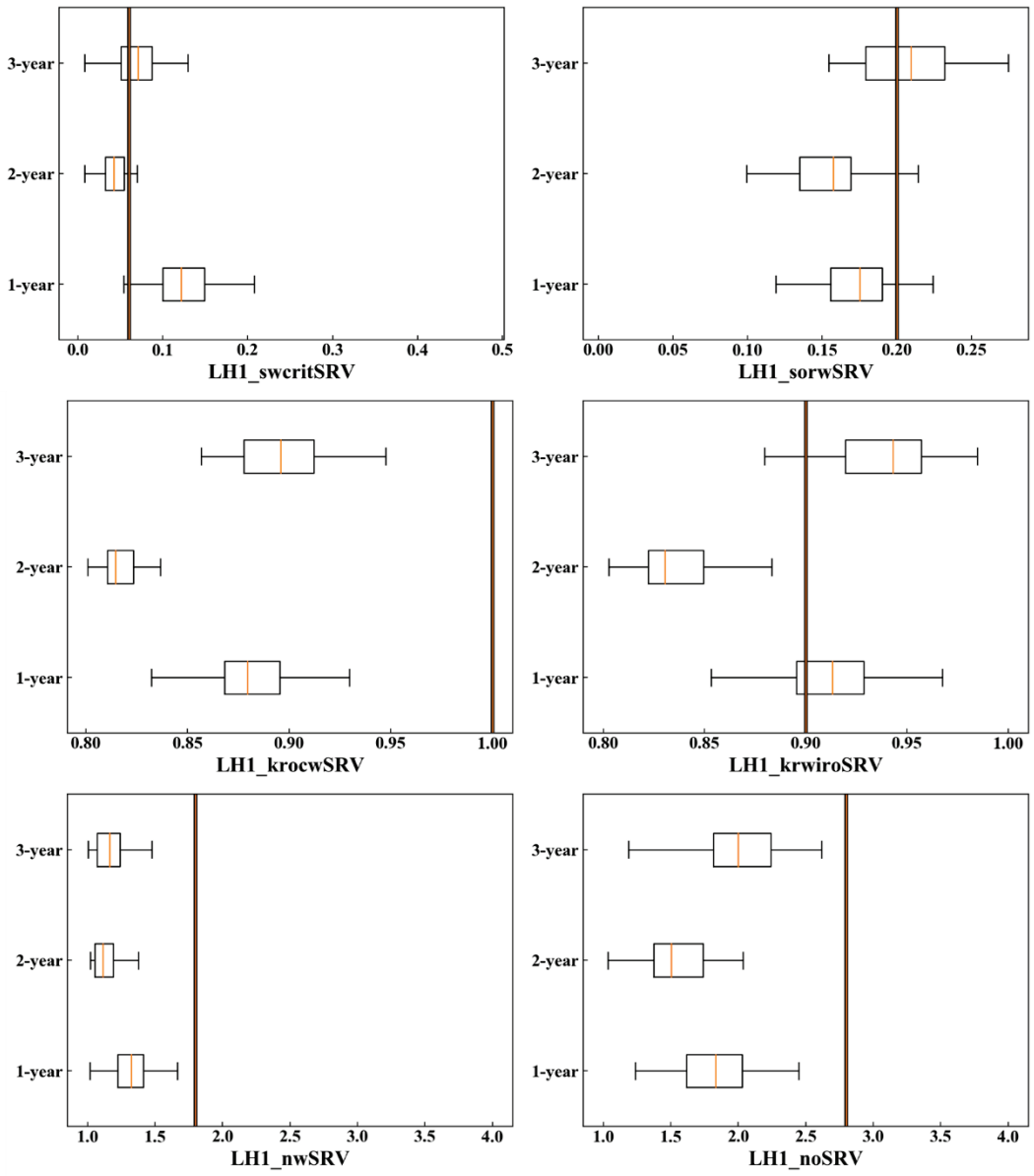

Figure 4.27 Comparison of marginal posterior distributions for the uncertainty parameters for three cases (II).

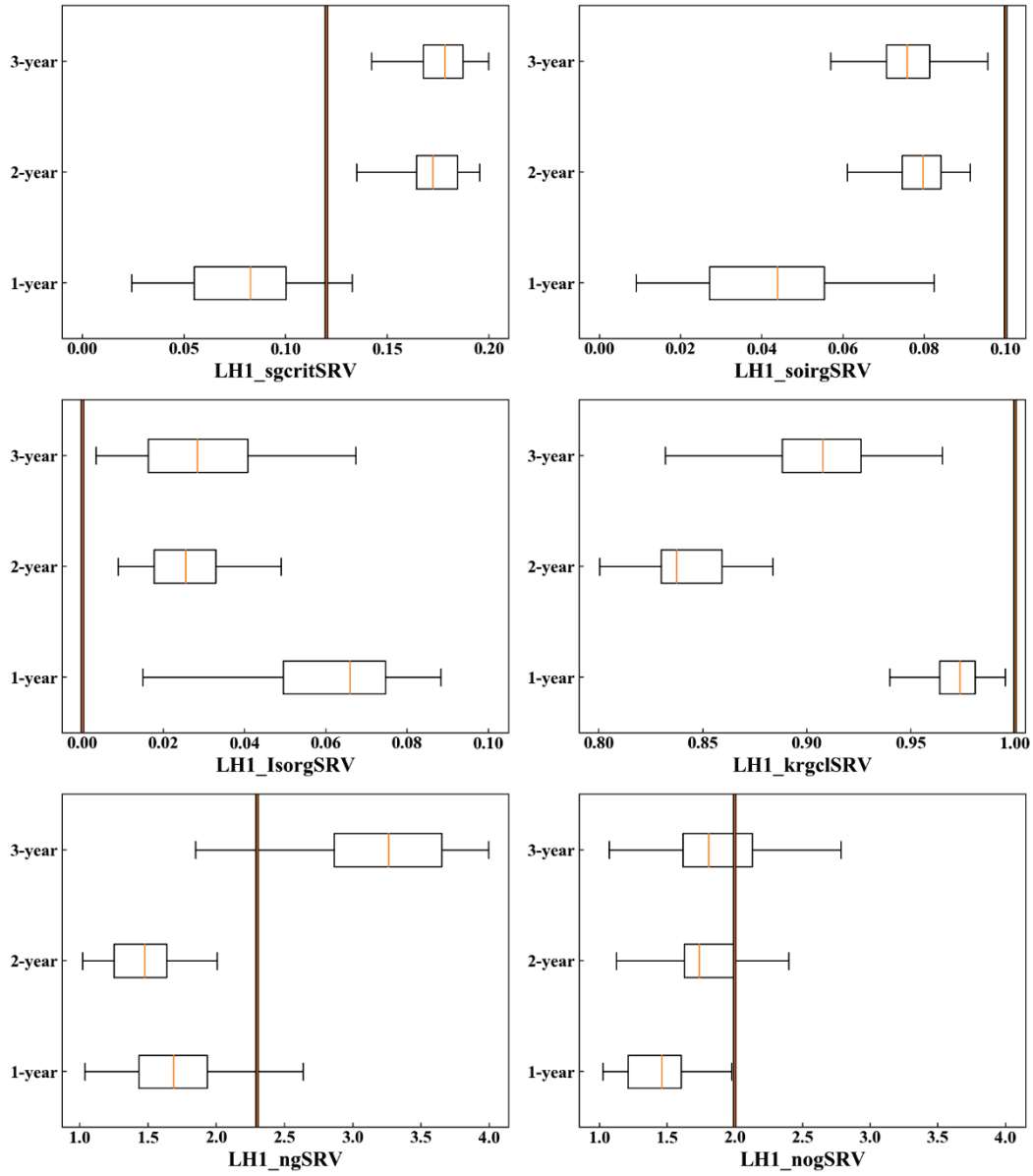

Figure 4.28 Comparison of marginal posterior distributions for the uncertainty parameters for three cases (III).

4.4.2.5 Probabilistic Production Forecasting

Production is extended from the satisfactory models for each case. Simulation conditions are the same as described in the previous section. A comparison between the predicted EUR from the three cases is summarized in the form of box plots (**Figure 4.29**). From the three cases, Case-2 seems to yield an EUR distribution closest to that truth EUR. As illustrated by the plots, the P25-P75 range for the two other cases does not enclose the truth EUR. In addition, Case-1 and Case-3 have wider distribution than Case-2. However, it will remain for future work to determine if that is an expected result for every trial or simply a random artifact.

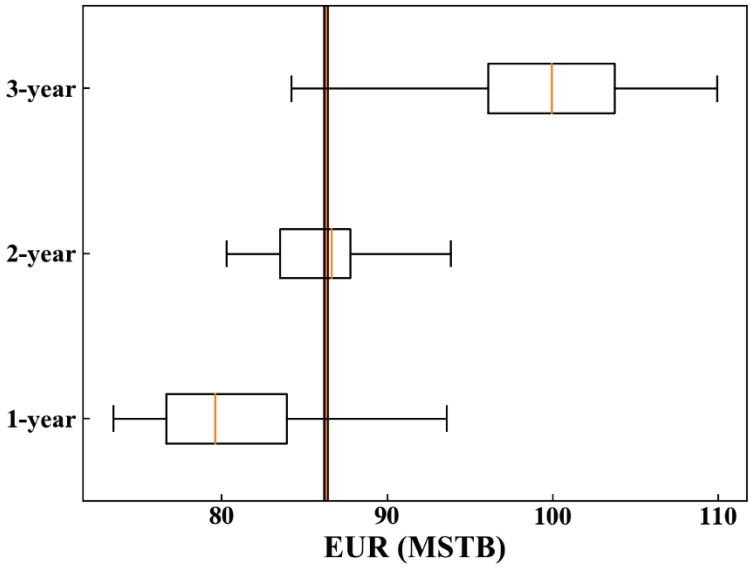

(a)

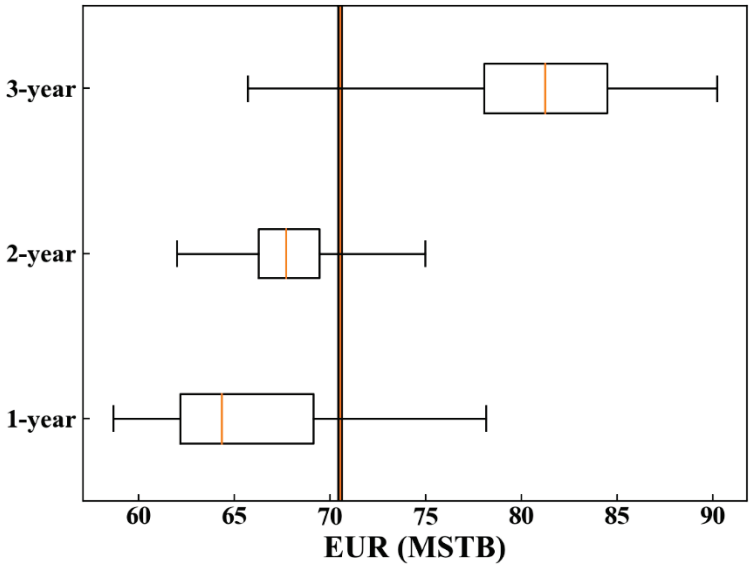

(b)

Figure 4.29 Box-plot comparison for EUR of the three cases for (a) well LH1 and (b) well LH2. The vertical line represents EUR for the truth model.

4.4.3 Bayesian Algorithm II

Using the same study conditions as Case-1 described in the previous section, we repeat the AHM experiment, now with a different Bayesian engine (Bayesian Algorithm II). Recall that this method is a variant of the Metropolis-Hastings MCMC algorithm, characterized by running relatively small number of simulations (compared to standard MCMC algorithms). For our case here, the method recommends for us to run 7260 simulation runs. We perform the same study under the same conditions, but we allow for larger number of simulations (almost 9 times greater than those run by Bayesian Algorithm I).

Run progress for the 7260 simulation runs is displayed in **Figure 4.30**. Although much larger, the total number of simulations is, the number of qualifying solutions is very modest. Only 8 candidates satisfy the predefined selection criteria (contrast that with the 68 solutions obtained by Bayesian Algorithm I). Another notable dissimilarity is that there appears to be no distinctive convergence pattern towards solutions as the algorithm progresses. There seem to be as many discarded solutions at later stages as there are in the very beginning.

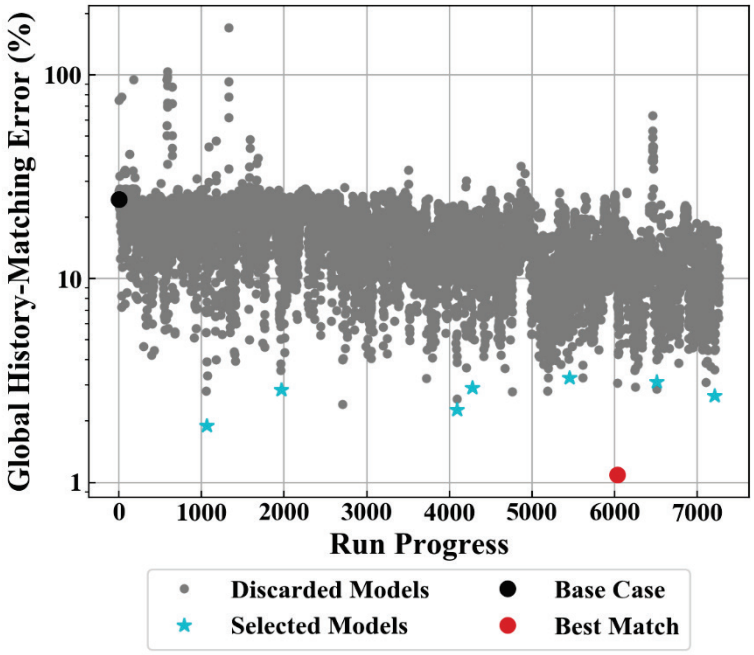

Figure 4.30 History-matching quality progress vs runs sequence for Bayesian Algorithm II covering first 1 year of observed data.

Results for LH2 BHP and water-phase matching quality are summarized in **Figure 4.31**.

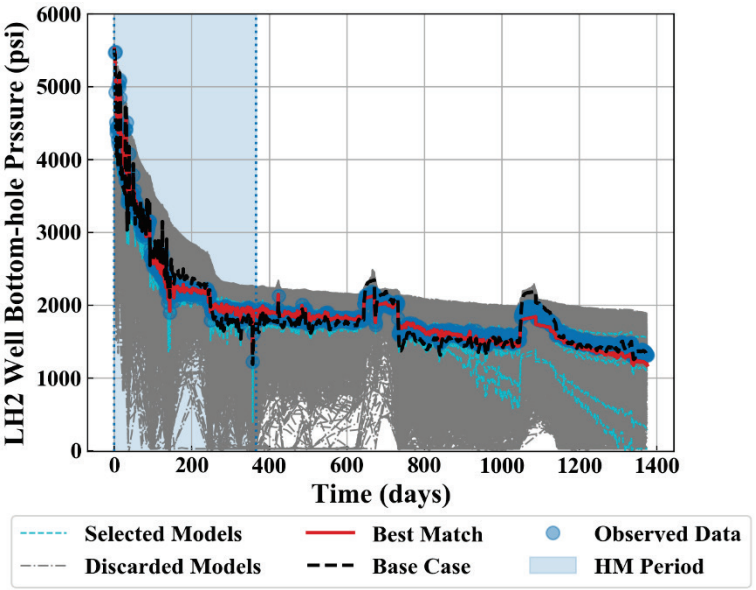

(a)

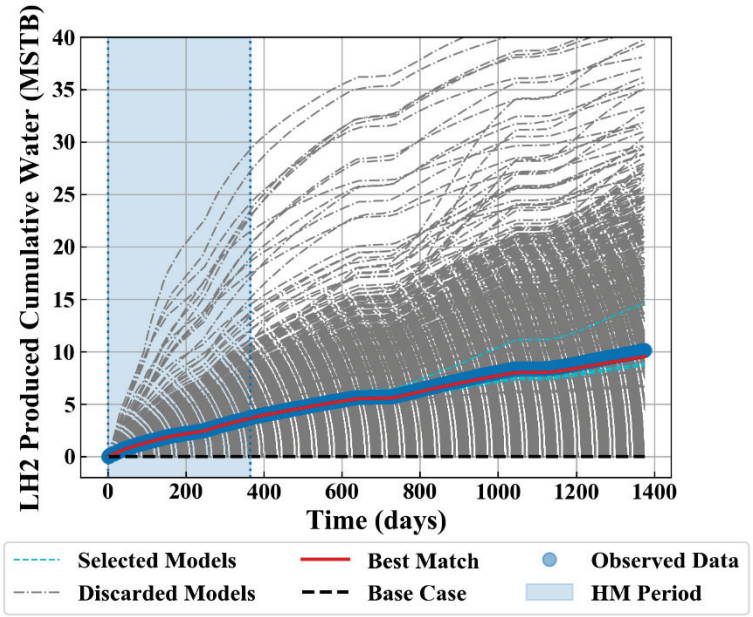

(b)

Figure 4.31 LH2 Bayesian Algorithm II results for history matching 1-year data sets of (a) bottom-hole pressure, and (b) produced cumulative water. There are 8 models selected from a total of 7620 runs.

4.4.4 DECE Algorithm

Using the same study conditions described in previous sections, we repeat the AHM experiment, now with a different optimization engine (DECE). Recall that DECE engine is a commercial iterative optimizer that runs in cycles to search for history-matching solutions. Each cycle consists of two stages: a designed-exploration stage and a controlled-evolution stage (CMG-CMOST 2017). This method yields no candidates satisfying the previously defined selection criteria after 810 simulation runs (**Figure 4.32**).

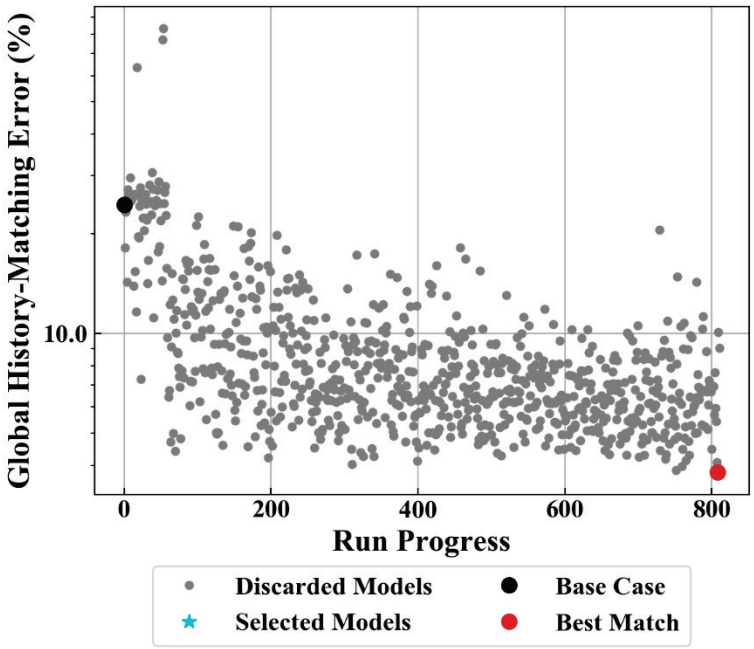

Figure 4.32 History-matching quality progress vs runs sequence for DECE algorithm covering first 1 year of observed data.

The lowest global error achieved is 3.8%, an average of 9.63% BHP error, 0.46% gas-phase error, and 1.34% water-phase error. The method is capable of separately achieving low individual errors, as there are other instances where BHP error is satisfactory while water-phase error is not. Reducing the error for all the error functions concurrently

seems to be unattainable for this case. Results for LH1 BHP and water-phase matching quality are summarized in **Figure 4.33**. The match for the best case is decent for water rates but is not satisfactory for BHP. On the other hand, although not displayed here, there is a decent match for LH2 BHP and water-phase data for that best case.

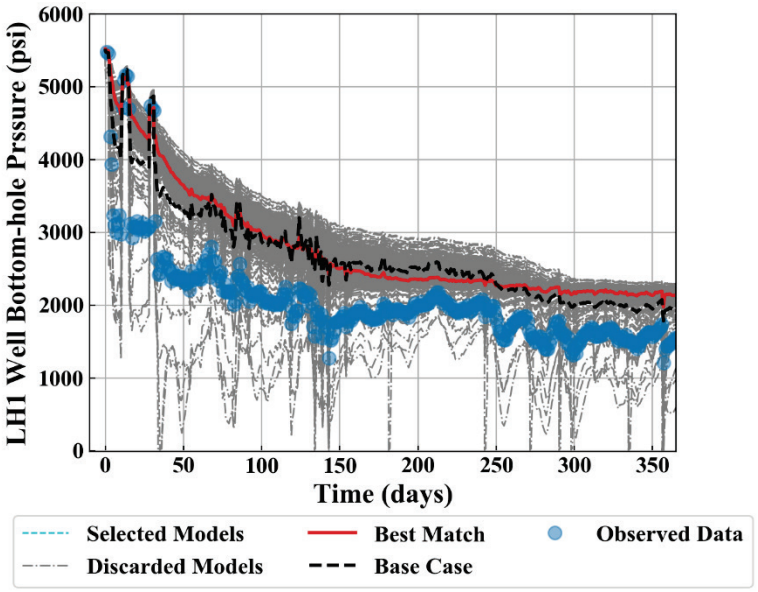

(a)

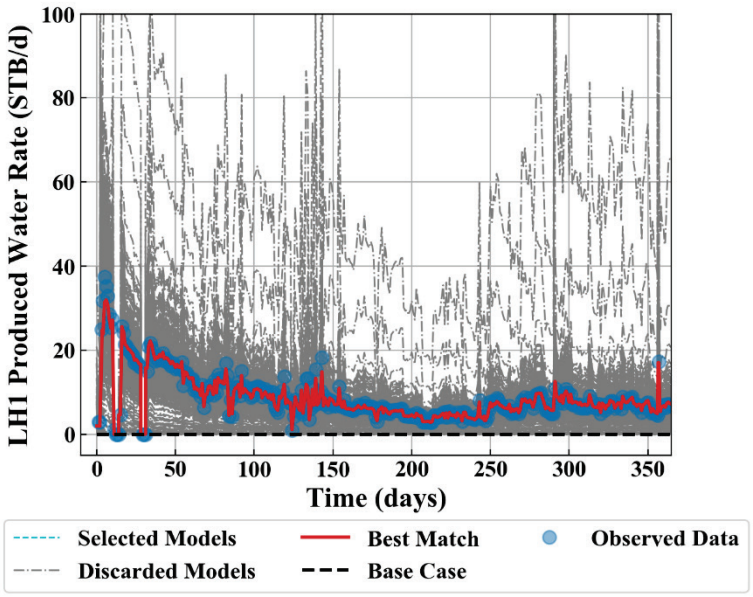

(b)

Figure 4.33 LH1 DECE algorithm results for history matching 1-year data sets of (a) bottom-hole pressure, and (b) produced cumulative water. There are no models selected from a total of 810 runs.

4.4.5 PSO Algorithm

Recall that particle swarm optimization (PSO) is a derivative-free stochastic optimization algorithm. This method comprises of a swarm (population) that consists of particles (solution candidates). As the algorithm progresses, the particles keep switching their positions in the swarm in pursuit of finding better solutions. In every iteration, each particle is assigned a velocity that is calculated based on the history of its own and its neighbors' performance.

As described in the previous chapter, the choice of PSO settings has a major impact on the optimization performance. In this work we implement two different settings for PSO to tackle the same AHM problem (PSO Take 1 and PSO Take 2). In the two settings, PSO parameters are kept the same and they are based on parameter set 2 from Trelea (2003). We set PSO parameters as: inertia term $\omega = 0.7298$, cognition and social components $\varphi_p = \varphi_g = 1.4962$. Between the two settings, we only vary the total number of simulations and the population size S. For PSO Take 1, the population size S is 20 and we allow a maximum number of 810 simulation runs. Whereas for PSO Take 2, the population size is 40 and we allow a maximum number of 1620 simulation runs, twice as much as Take 1.

4.4.5.1 PSO Take 1

This method yields 2 candidates qualifying as solutions (**Figure 4.34**). The best match in this case does not fully satisfy the selection criteria, even though it has the lowest the global error. Note that, in this case, noticeable convergence towards objective-function minima does not occur until later in the progress (the last 200 simulation runs, or roughly

the last 25% of runs). This observation motivates us to increase the maximum number of simulation-runs in anticipation to obtain more solutions.

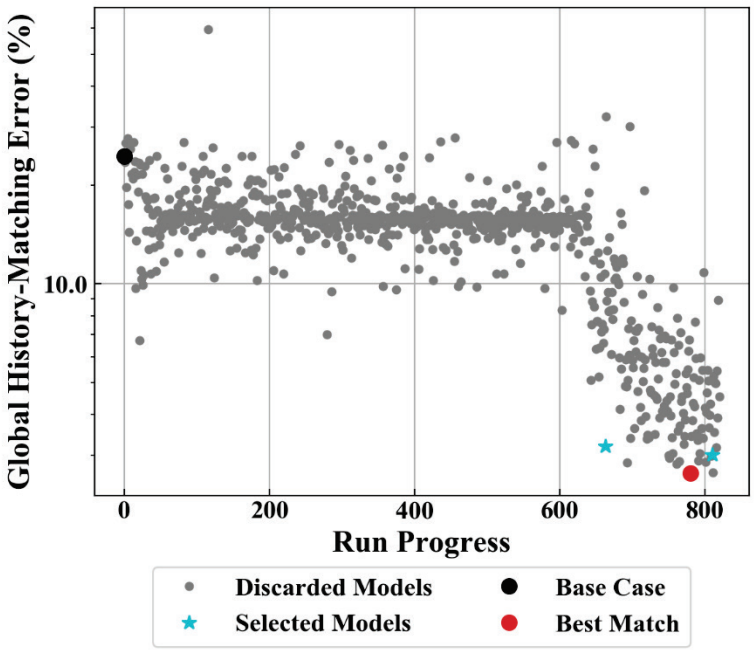

Figure 4.34 History-matching quality progress vs runs sequence for PSO Take 1 covering first 1 year of observed data.

Results for LH2 BHP and water-phase cumulative production matching quality are displayed in **Figure 4.35**.

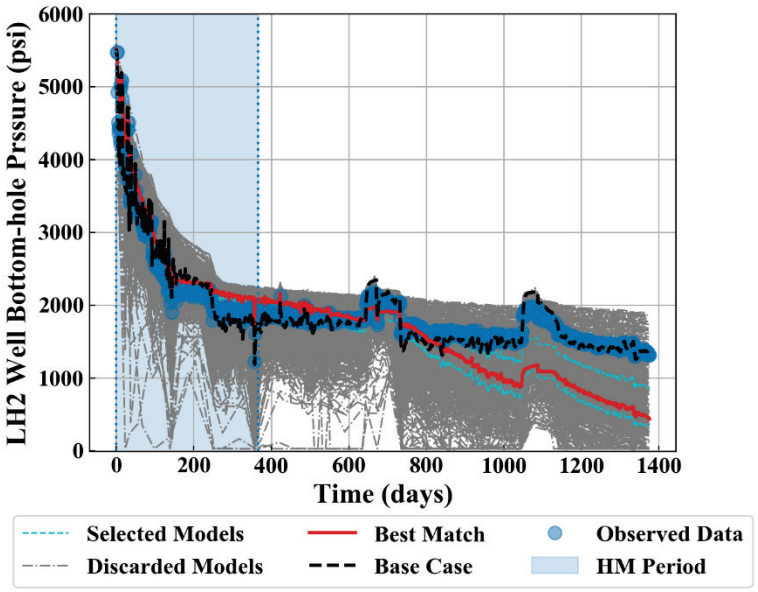

(a)

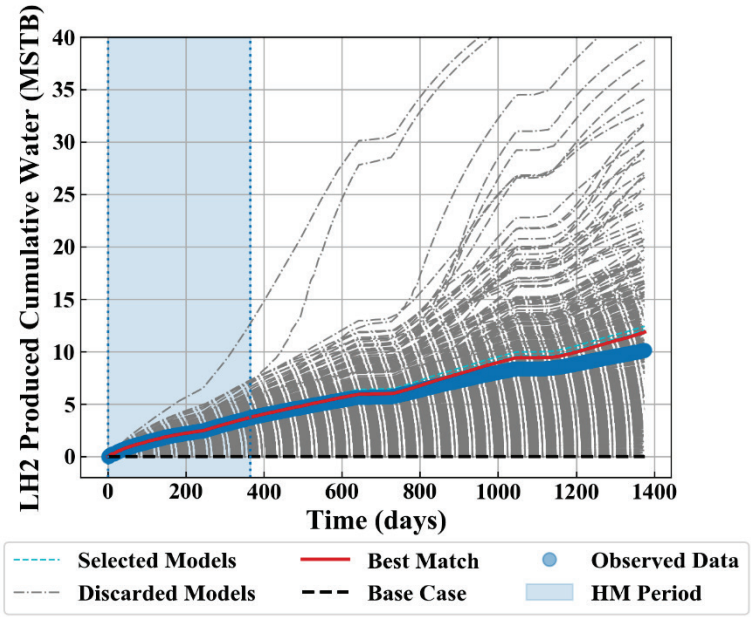

(b)

Figure 4.35 LH2 PSO Take 1 algorithm results for history matching 1-year data sets of (a) bottom-hole pressure, and (b) produced cumulative water. There are 2 models selected from a total of 810 runs.

4.4.5.2 PSO Take 2

Recall that PSO Take 2 has the same PSO parameters as Take 1, and the difference lies in that here the population size and the maximum number of simulations are the double. Such a change results in significantly larger number of match-satisfying candidates (**Figure 4.36**). The number of accepted solutions for Take 2 is 77 (compare that to the 2 solutions obtained by Take 1). Still the behavior of the algorithm is similar; the algorithm does not start to reach solutions until late during its run progress. Almost all selected models are among the last 400 simulation runs (or, the last 25% of runs, similar to Take 1). This implies that, for PSO algorithm to converge, the recommended minimum of simulation runs should be proportional to the population size.

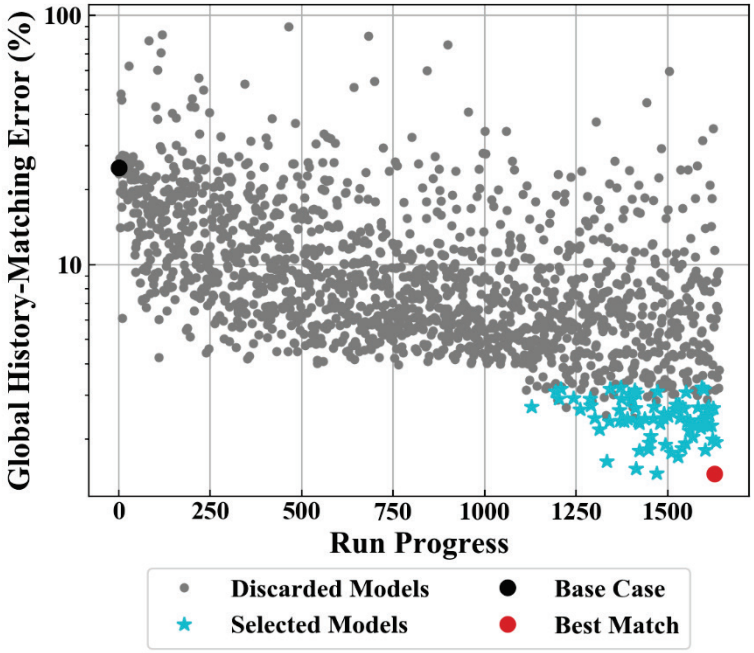

Figure 4.36 History-matching quality progress vs runs sequence for PSO Take 2 covering first 1 year of observed data.

The algorithm behavior here is more preferential, though, as the larger population sample results in greater exploitation of parameter space. Such greater exploitation results in achieving states with lower errors early on in the algorithm progression, and achieving more solutions (compare **Figure 4.36** to **Figure 4.35**). Results for LH2 BHP and water-phase cumulative production matching quality are displayed in **Figure 4.37**.

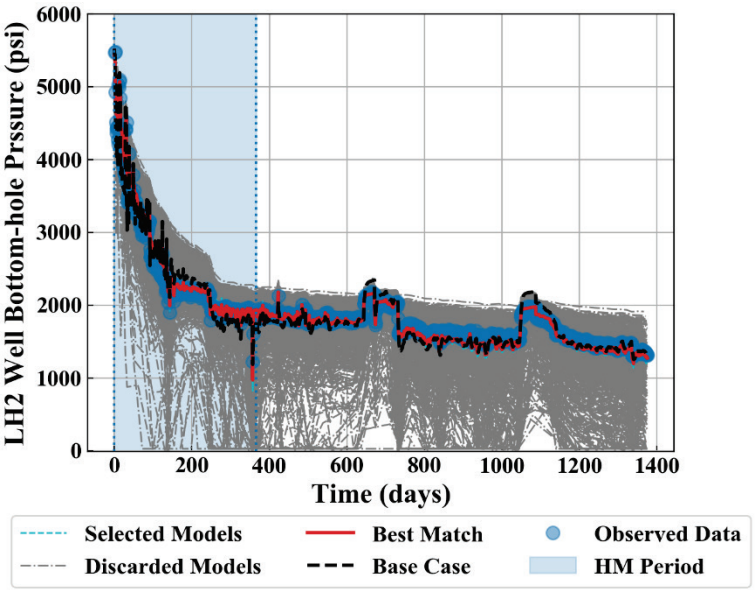

(a)

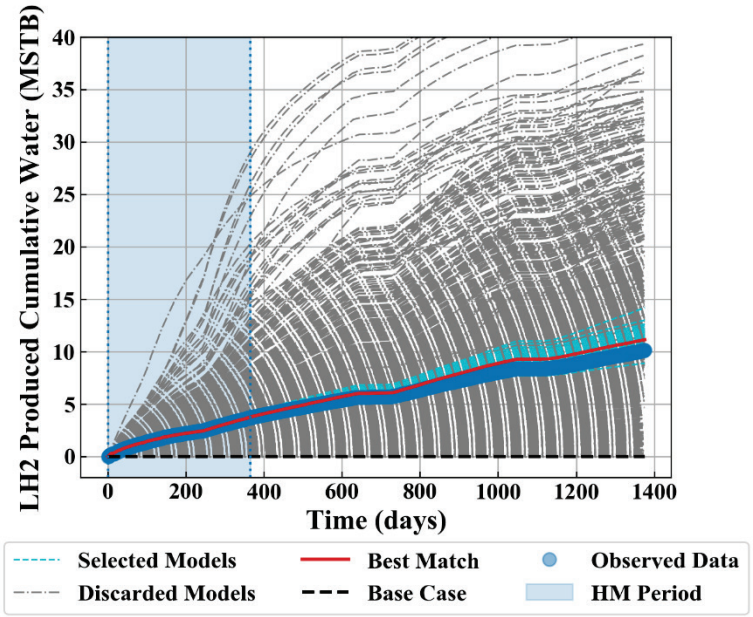

(b)

Figure 4.37 LH2 PSO Take 2 algorithm results for history matching 1-year data sets of (a) bottom-hole pressure, and (b) produced cumulative water. There are 77 models selected from a total of 1620 runs.

4.4.6 Benchmark Comparison

Now, we present a comparison between all the AHM methods utilized in this chapter. The benchmarking metrics are: selected sample size; total simulation runs; marginal posterior distributions; and EUR ranges.

4.4.6.1 Selected Sample Size vs Total Simulation Runs

One way to measure AHM performance is to measure the size of the obtained sample. This quantifies the method's capability to converge to history-matching solutions; the larger the sample size, the higher the performance. A large sample size, however, does not guarantee accurate sampling from the posterior PDF; obtained solutions might be picked from one narrow portion of the exact posterior. Another performance metric is the amount of full simulation runs required to obtain the sample of solutions. This metric is useful to measure the algorithm's computational requirement, which is a rather important aspect in practical problems.

Performance comparison of the methods is summarized in **Table 4.8**. Bayesian Algorithm I achieves the best performance with the lowest runs/sample-size ratio. DECE Algorithm has the poorest performance, followed by Bayesian Algorithm II. Although PSO Take 2 requires twice as much total runs as PSO Take 1, it generates far larger solution sample.

Method	Total Runs	HM Sample Size	Runs Per Sample
Bayesian Algorithm I	810	68	11.91
Bayesian Algorithm II	7620	8	907.50
DECE Algorithm	810	0	∞
PSO Take 1	810	2	405
PSO Take 2	1620	77	21.03

Table 4.8 Performance comparison of the different methods considered.

4.4.6.2 Marginal Posterior Parameter Distributions

Recall that only few AHM methods are known to converge to an exact posterior PDF (e.g., MCMC and MultiNest). In our study, application of such methods is currently not feasible because of the prohibitively large number of simulations required. Therefore, for performance benchmarking, none of the methods tested here can be assumed to converge to the exact posterior PDF. That stated, parameter posterior PDF obtained from different methods could still be plotted in boxplot form to compare the behaviors of each method (**Figure 4.38**, **Figure 4.39**, and **Figure 4.40**).

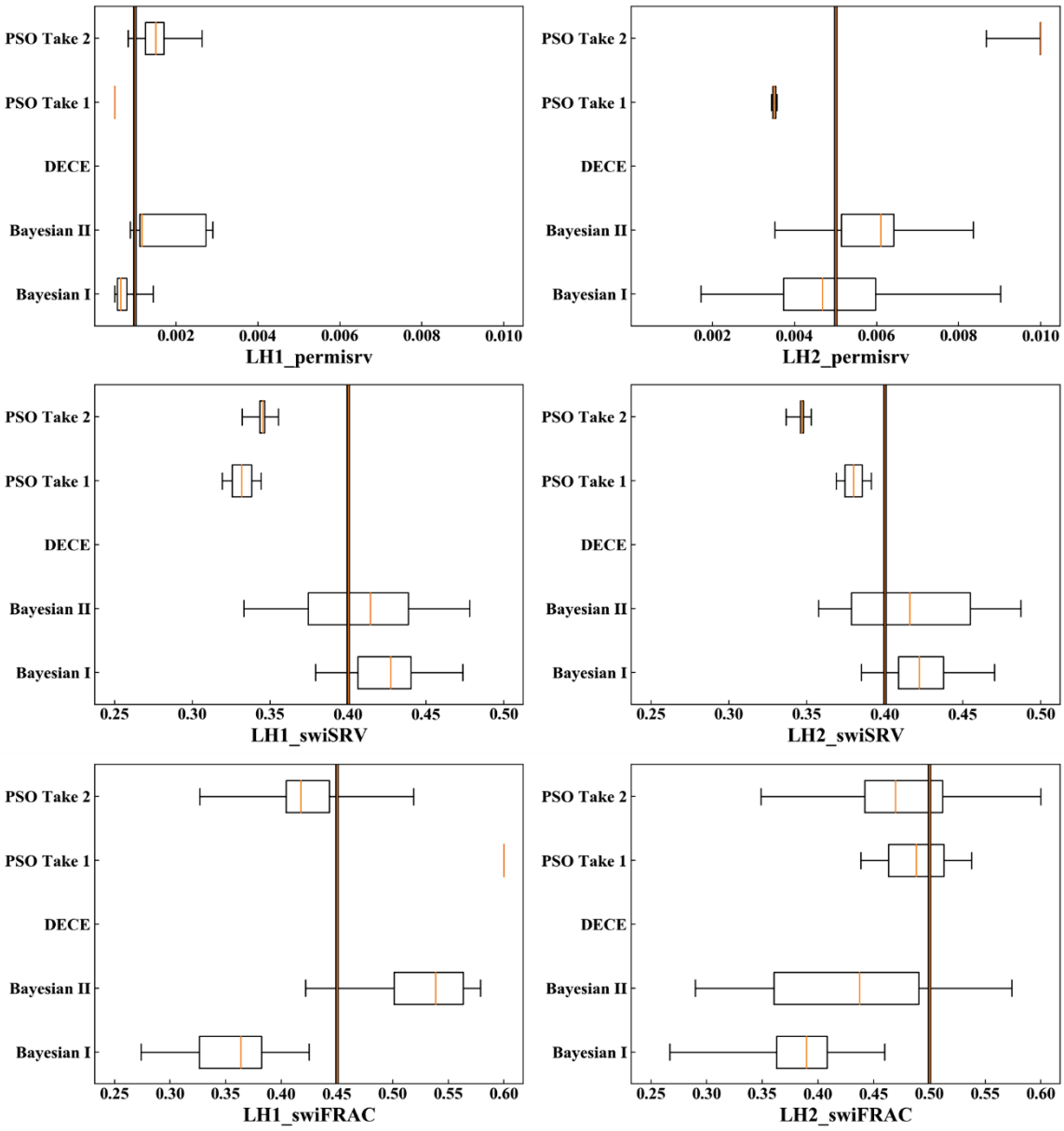

Figure 4.38 Parameter marginal-posterior-distribution comparison for the methods considered (I).

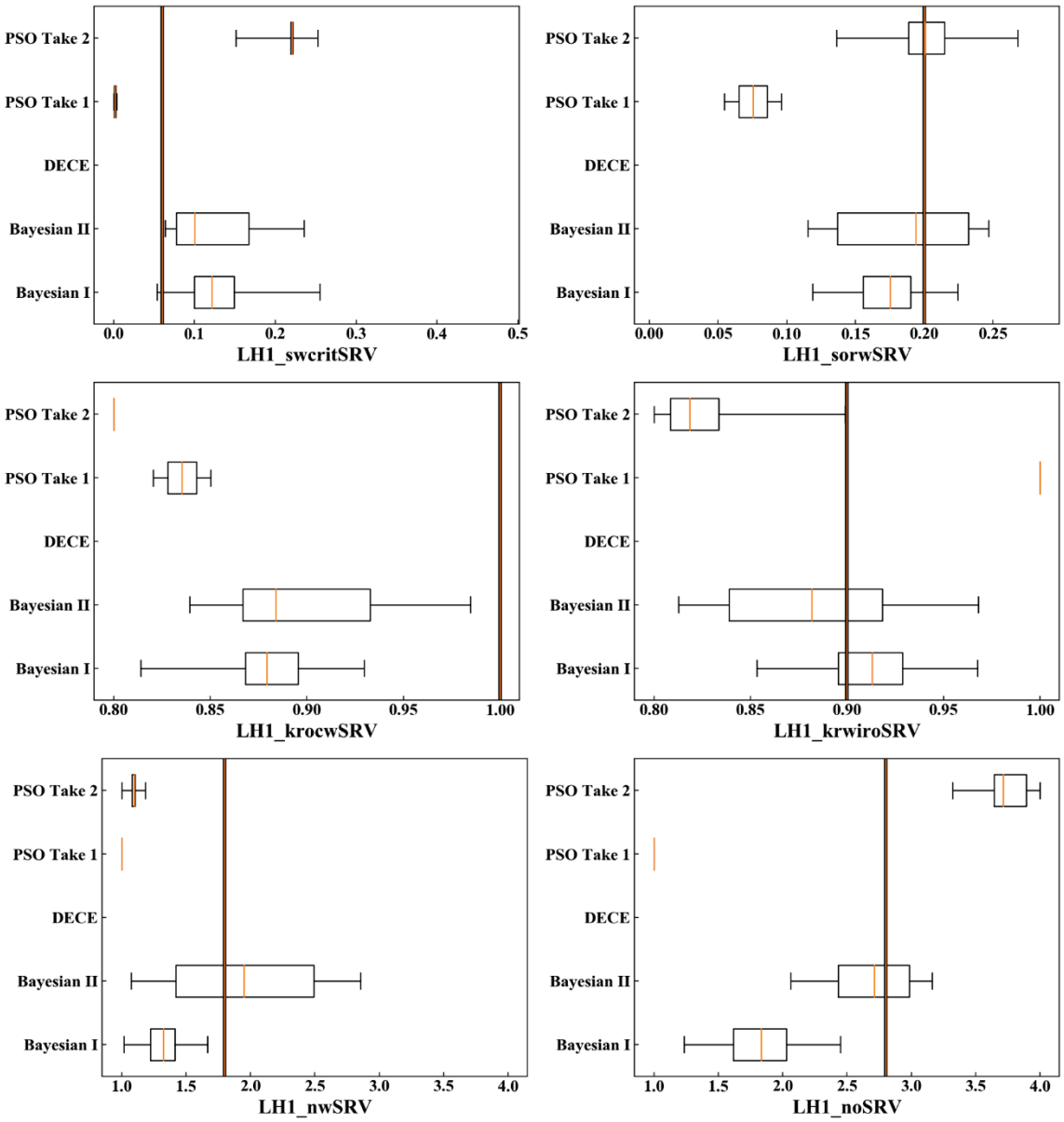

Figure 4.39 Parameter marginal-posterior-distribution comparison for the methods considered (II).

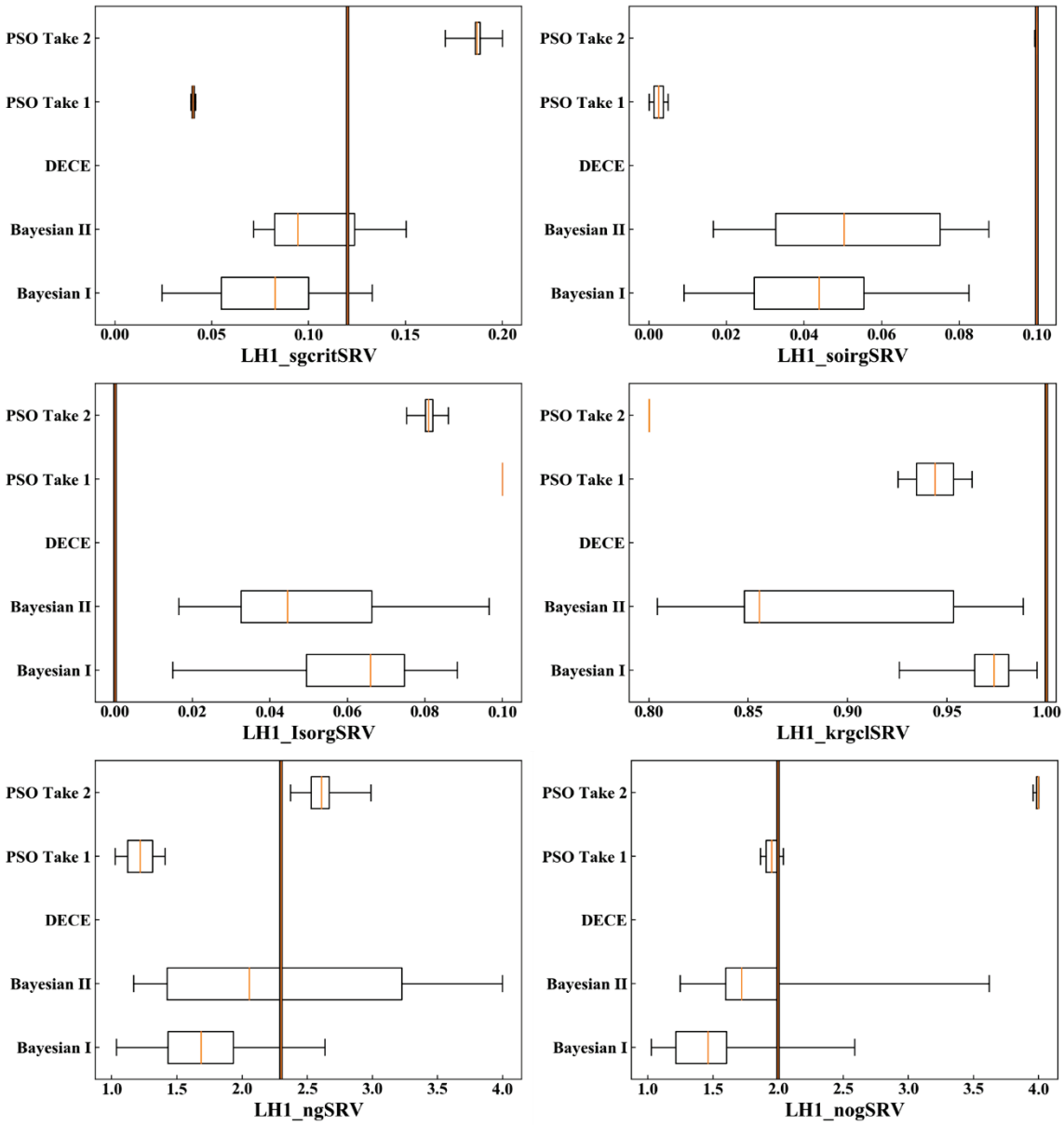

Figure 4.40 Parameter marginal-posterior-distribution comparison for the methods considered (III).

DECE distributions are missing from the plots because the method yields no qualifying candidates. PSO distributions are notably narrower than the Bayesian,

particularly for the more influential parameters. Even though PSO Take 2 generates far more solutions than Bayesian Algorithm II, PSO seems to sample only a small narrow portion of the posterior PDF. Moreover, for most parameters, the range for PSO posterior parameters fails to enclose the truth. Bayesian Algorithm II appears to have the widest range of posterior parameters, even for the influential ones. The prior and the likelihood are defined correctly in this synthetic case, and hence we expect that posterior ranges for influential parameters should enclose the truth-values. Bayesian Algorithm II has better sampling of the posterior than Bayesian Algorithm I. For example, the posterior distributions for permeability and initial saturations are clearly better spread around the truth for Bayesian Algorithm II.

Another insightful comparison can be inferred from examining the trends of relative-permeability curves of the selected models. **Figure 4.41**, **Figure 4.42**, **Figure 4.43**, and **Figure 4.44** stack relative permeability curves for selected models obtained by different algorithms. PSO methods clearly don't sample correctly from the posterior; the selected curves could lie further away from the truth (**Figure 4.43**) and could be condensed around a certain spot in the parameter space (**Figure 4.44**). The Bayesian algorithms are clearly superior in sampling from the posterior. Bayesian Algorithm II provides better coverage around the truth than Bayesian Algorithm I (compare **Figure 4.42** to **Figure 4.41**).

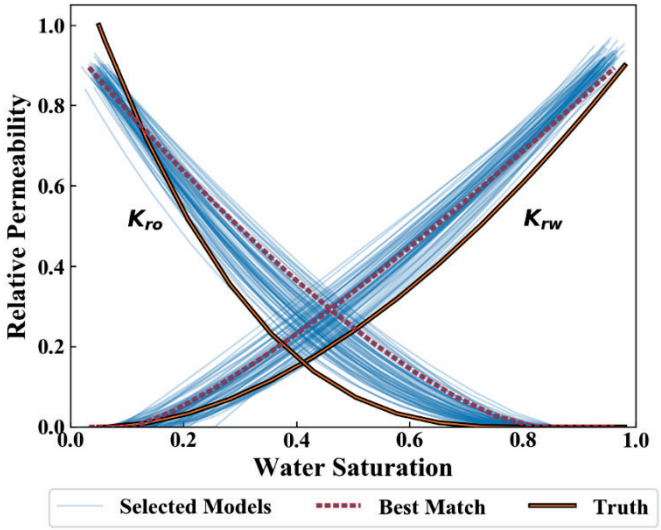

Figure 4.41 Relative permeability curves for selected models (Bayesian Algorithm I).

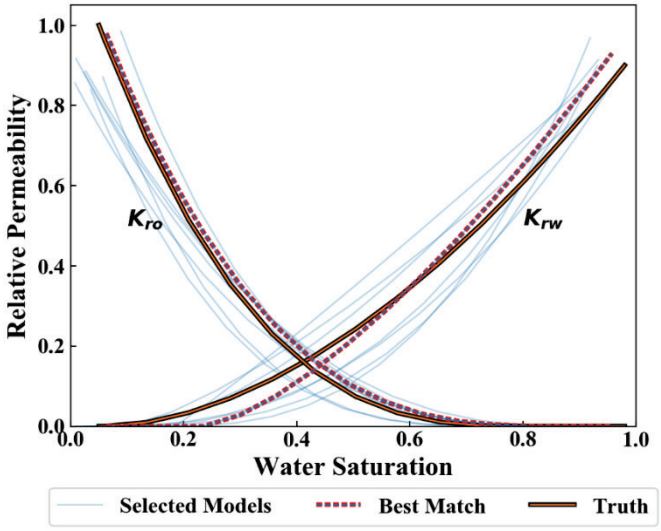

Figure 4.42 Relative permeability curves for selected models (Bayesian Algorithm II).

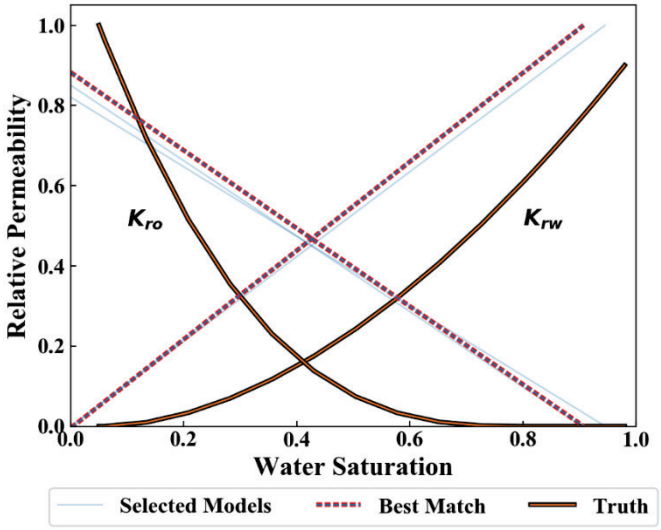

Figure 4.43 Relative permeability curves for selected models (PSO Take 1).

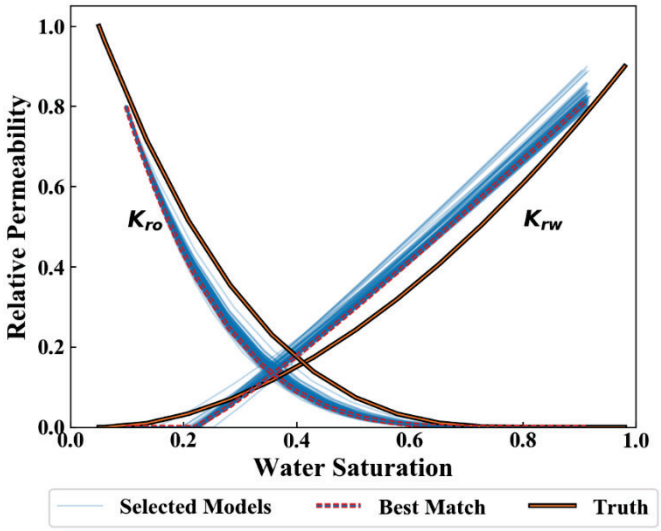

Figure 4.44 Relative permeability curves for selected models (PSO Take 2).

4.4.6.3 Probabilistic Production Forecasting

Production is extended from the selected models for all the methods. We quantify uncertainty by assessing the range of EUR obtained from forecasts of the selected ensemble. Simulation conditions for forecasting period are the same as described earlier in the chapter. A comparison between the EUR ranges from the five methods is summarized in the form of box plots (**Figure 4.45**).

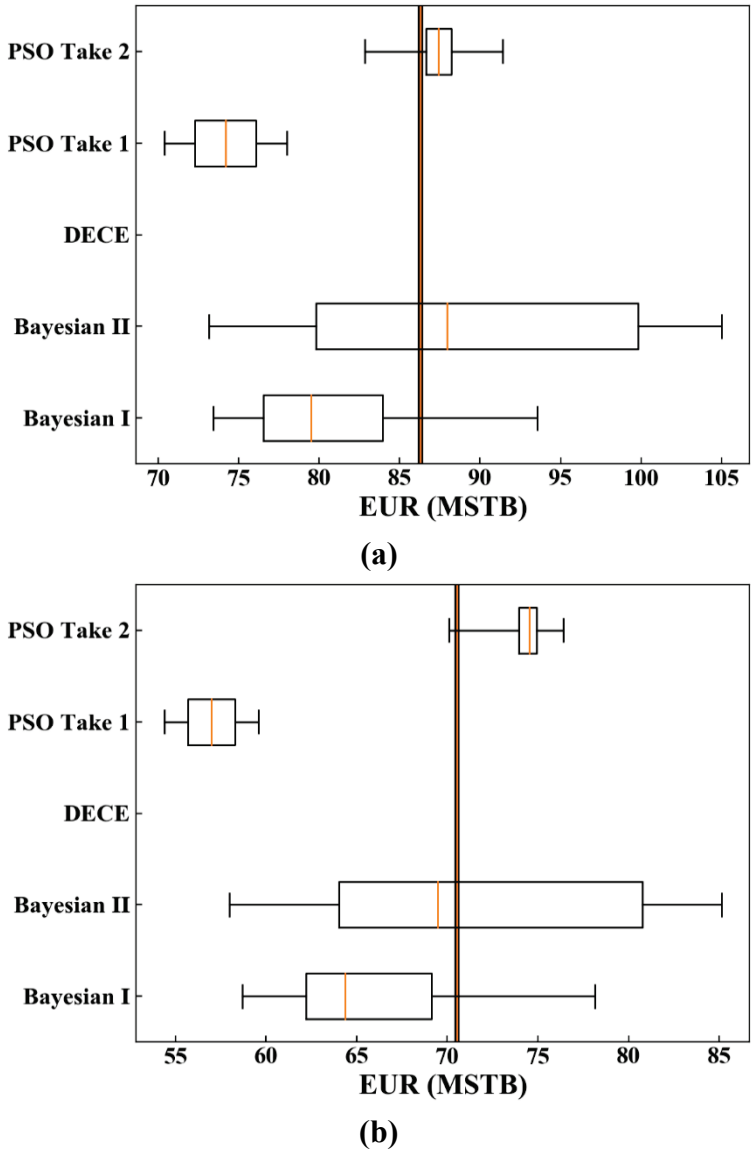

Figure 4.45 Box-plot comparison for EUR uncertainty obtained by the different methods for (a) well LH1 and (b) well LH2. The vertical line represents EUR for the truth model.

Recall that none of the methods tested here can be assumed to converge to the exact posterior. Nevertheless, we can infer insightful information by examining the uncertainty

ranges produced by each method. Bayesian Algorithm II has the widest range of uncertainty, even though the sample comprises of only 8 qualifying candidates. Such a small number of candidates may not be representative of true uncertainty, but it is worth noting that the truth EUR is enclosed in the P25-P75 range for Bayesian Algorithm II only. For the rest of the methods, the truth EUR lies either outside the inter-quartile range or outside the whole uncertainty range. For that, we have reason to believe that the rest of the methods fail to correctly capture uncertainty, at least when compared to results obtained from Bayesian Algorithm II. As expected, PSO forecasts are condensed around a certain EUR. In other words, the interquartile range is significantly narrower than the Bayesian methods, even though, for example for PSO Take 2, solution sample size is the largest. Bayesian Algorithm I seems to produce pessimistic forecasts (P50 and P75 predictions are smaller than the truth). However, Bayesian Algorithm I still preserves larger portion of the true uncertainty when compared to PSO, and hence presents a better choice for uncertainty quantification.

4.5 CONCLUSIONS

In this study, we exploited the capabilities of the developed workflow for multi-well AHM problems with large number of dimensions (20 uncertain parameters). The case study considered in the chapter is motivated by typical unconventional reservoir encounters but is based on a hypothetical model with synthetic data. This gives the opportunity to meaningfully test and compare different AHM sampling algorithms. From the various numerical experiments entailed in the chapter, we draw the conclusions:

- AHM solutions, generated by Bayesian Algorithm I to minimize data mismatch for the first-year data records only, establish an acceptable match for the remaining 2-year period for BHP and water-phase rates. Gas-phase rates significantly diverge

after history-matching period because gas relative-permeability curve does not turn out to be influential to the likelihood until after the first year.

- Relative permeability curves for solution candidates can vary significantly from the truth. For real field-case problems, we shall expect similar non-unique results.
- Among relative permeability curves, the water curve is the most influential one to the likelihood in our case.
- Bayesian Algorithm I is the most efficient with the smallest runs/sample-size ratio. PSO would rank second in efficiency, followed by the Metropolis-Hastings MCMC variant Bayesian Algorithm II. DECE ranks last as it fails to generate any solution candidates (as in **Table 4.8**).
- Parameter posterior distributions formed by Bayesian Algorithm II have better conformance with truth parameters. Evidently, Bayesian Algorithm I seems to pick up bias towards certain areas of the posterior as the run progresses, resulting in an under-sampled posterior.
- PSO results in sampling a far narrower range from the posterior, even for non-influential parameters. The parameter posterior for obtained samples fails to include the truth for some influential parameters. Relative permeability samples for PSO follow more-or-less the same trend.
- PSO produces forecast samples with significantly underestimated uncertainty range. Bayesian Algorithm I produces broader uncertainty range but seems to be inclined towards pessimistic forecasts. Bayesian Algorithm II produces the broadest uncertainty, and, therefore, we rank it as best for quantifying uncertainty.

As explained earlier, obtaining the exact posterior is currently not affordable. Therefore, in our case, there is no point of reference we may compare results to. However, we can attempt to make recommendations based on comparing results to each other and to

the truth. From the available commercial algorithms, DECE is inadequate for a problem with a modest number of dimensions, as it fails to generate any qualifying candidates. PSO seems to get trapped around certain areas of the parameter-space, which makes it less attractive for AHM/UQ applications. Bayesian Algorithm I offers an acceptable compromise between computational robustness and results accuracy. Therefore, we endorse Bayesian Algorithm I for use in similar problems with the understanding that the resulting posterior might be ill sampled and/or inaccurate. If running thousands or tens of thousands of simulations is not a limitation, Bayesian Algorithm II would be more attractive, as it seems to produce more accurate posteriors.

Findings from this case study may be generalized to other cases, because the numerical experiments were conducted under the same constraints and conditions. However, because of the random nature of most of the samplers, differing behaviors might be encountered.

Chapter 5: Assessing the Effect of Natural Fractures in the Bakken – An AHM Study

5.1 MOTIVATION

As characterization of natural fractures remains a challenge, EDFM reservoir simulations can still assist in locating and describing natural fractures. We can investigate different natural-fracture scenarios. For each scenario, multiple simulations may be run and stacked up against production history. By comparing results, we cannot fully characterize the natural-fracture network, but we can at least favor one scenario over another. Regardless of our certainty of the fracture network, EDFM simulations may provide insights about the contribution of natural fractures in hydrocarbon production from unconventional reservoirs. Moreover, we can assess the effect of natural fractures on our portrayal of other reservoir properties. This is investigated later in the chapter by introducing random natural-fracture distribution in the near-well-bore volume.

5.1.1 Natural Fractures in Unconventional Reservoirs

Natural Fractures has been thought of to play an important role in production from shale reservoirs, as production has been historically larger than the expectations (Gale et al. 2014). However, it is not yet fully understood how existing natural fracture networks contribute to overall permeability of the shale reservoir after a hydraulic-fracture treatment. Recent work suggests linking between the induced fractures and natural-fracture systems. Such an access to natural-fracture systems increases the effective surface area available to wellbore. The increased surface area will contribute to increasing linear flow, the dominant flow regime in low-permeability shale (Gale et al. 2014). Although several studies have been published as well as models have been developed to account for these interactions, a

full quantitative model that describes the contributions of the natural fractures in shale plays has not yet been established.

Information about the fractures that naturally occur near the producing reservoir is difficult to obtain. As seen in **Figure 5.1**, there is a large uncertainty inherent to fractures occurring naturally, particularly in shale formations. Techniques, such as microseismic imaging and imaging logs, can be practical for detecting natural fractures in the subsurface (Gale et al. 2014). However, much of these data is not readily available for many wells because microseismic imaging is still expensive to run, may be poor in resolution, and has uncertainty in processing. Well-testing analysis is rarely conducted in shale gas wells because it typically requires shutting in the well for a long time. In the lack of direct data, most of characterization work relied on examinations of core plugs and outcrops. While they give us valuable insight, they may, in many cases, be misleading (Gale et al. 2014). As being retrieved from the subsurface, formation cores undergo secondary fractures due to stresses and changes in pressure. Therefore, it becomes difficult to distinguish natural fractures from core partings.

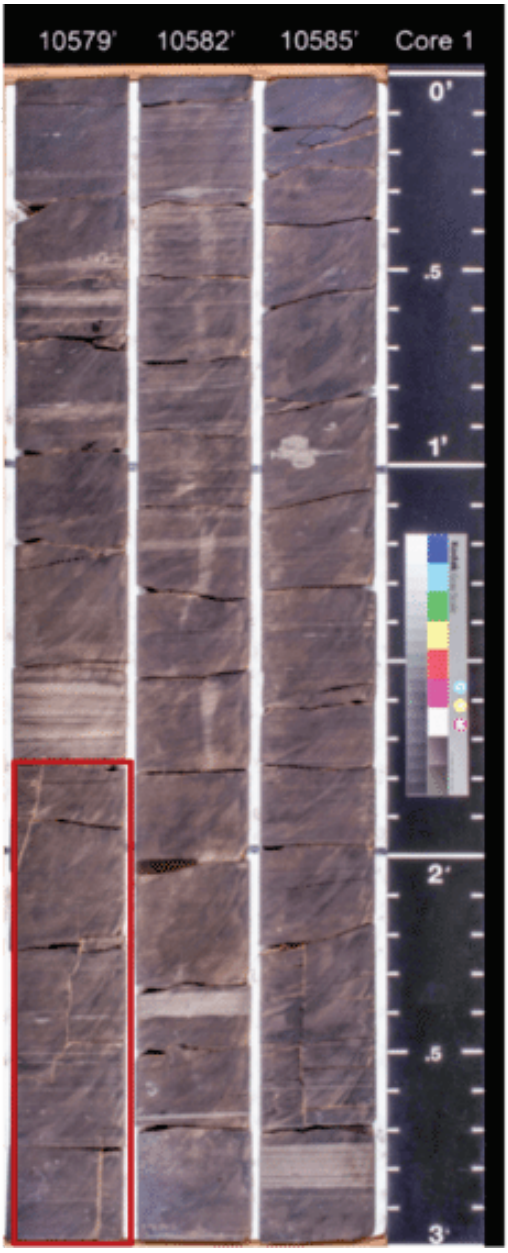

Figure 5.1 Core images taken from the Upper Bakken Shale. Note the vertical natural fractures inside the red box (from Xu and Sonnenberg 2016)

Outcrops are the one source that provides us with effective measurements of the lengths and orientation of fractures. We may interpret this information as an analog for the

undersurface. However, shale rock usually undergoes weathering, and therefore outcrops of shale formations are not as common as other sedimentary rocks (Gale et al. 2014). While these outcrops may be used as a representation to the deep reservoir, they can sometimes give a misleading interpretation. Outcrops are subject to weathering and precipitation of minerals that do not necessarily occur in the subsurface.

If sufficient characterization of natural fractures is available, one may use a method proposed by Shakiba and Sepehrnoori (2018) to construct a realistic discrete fracture network (DFN) from the recorded microseismic events. The produced DFN is then incorporated in an EDFM grid as described before.

5.1.2 Modeling Scenarios

Consider two initial modeling scenarios shown in **Figure 5.2**. If we are to take natural fractures into account when modeling production from unconventional reservoirs, we ought to expect that it shall affect main reservoir properties, particularly hydraulic fracture geometry and conductivity and matrix permeability. If we allow those properties to be history-matching conditioning parameters, we expect history matching solutions in each case to be significantly different than the other (as exaggeratingly presented in **Figure 5.2**).

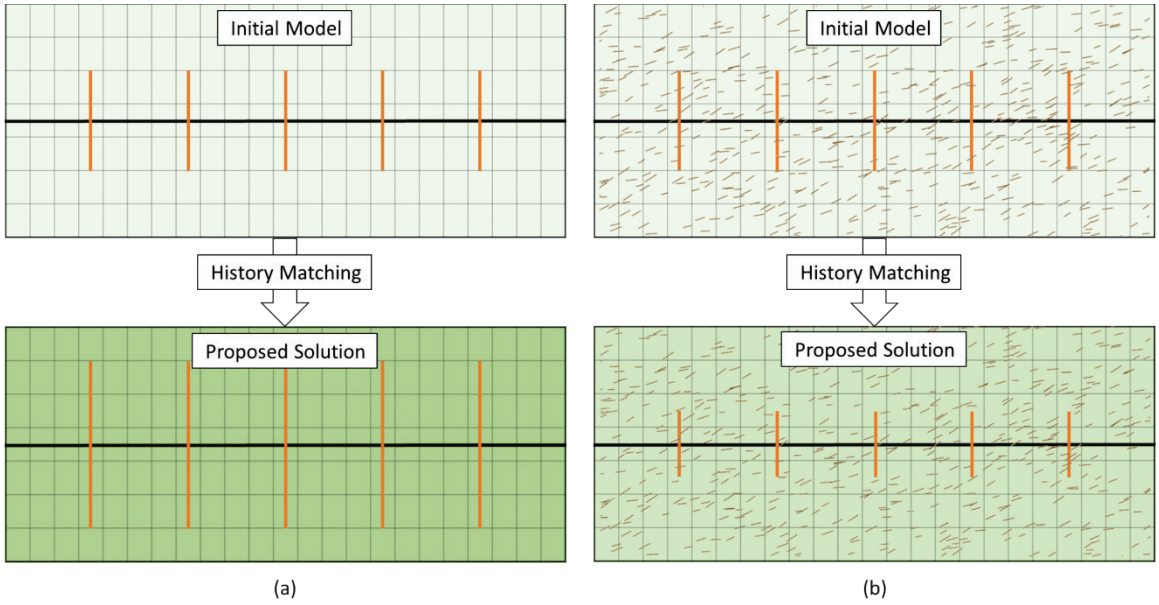

Figure 5.2 Schematic plan-view models of a horizontal well with planar hydraulic fractures (represented by vertical orange lines). A darker green indicates larger permeability of a grid block. Sample production history–matched solutions are obtained for (a) a model without natural fractures and (b) the same model after including natural fractures.

Even though the number of uncertain parameters is relatively small (matrix permeability, fracture half length, height and conductivity), manual tuning to achieve history matching is difficult. The problem is still multi-dimensional and highly non-linear. Furthermore, as has been shown, various configurations could produce the same history but does not guarantee reliable prediction (Li et al. 2011). Therefore, we must consider the non-uniqueness of history-matching solutions.

5.2 SIMULATION SETUP

We test our history-matching workflow on a single horizontal well drilled in the Middle Bakken formation. The numerical-model configuration is adopted from Wantawin et al. (2017a). **Table 5.1** summarizes the properties of the reservoir model used in the study. We use a black-oil simulator in this example. Fracture clusters in a single stage are represented by multiple effective planar fractures and then integrated discretely using EDFM. In all simulations presented in the paper, we use two effective fractures per stage.

Parameter	Value	Unit
Model dimensions (x × y × z)	10502 × 2640 × 50	ft
Number of gridblocks (x × y × z)	178 × 43 × 1	-
Initial reservoir pressure	7800 psi	psi
Reservoir temperature	245	^{o}F
Total Compressibility	1×10^{-6}	psi $^{-1}$
Bubblepoint pressure	2500	psi
Oil density	50.86	lbm/ft^3
Gas density	0.92	-
Matrix porosity	0.056	-
Horizontal well length	8828	ft
Number of stages	15	-
Cluster spacing	118	ft
Fracture width	0.01	ft

Table 5.1 Reservoir and fracture parameters for the simulation setup

We investigate uncertain parameters for two main scenarios: one incorporating only hydraulic fractures intersecting matrix cells and another incorporating both discrete hydraulic and natural fractures (**Figure 5.3**). **Table 5.2** lists the assessed prior range for four uncertain parameters we vary for both scenarios. Note the following flexibility in fracture properties introduced by EDFM: fracture height may now be added as a variable regardless of layer thickness (layer thickness remains constant for all simulations), and fracture half-length is now independent of grid size and may vary continuously rather than discretely. Prior-probability distributions for all uncertain parameters are assumed uniform

because information about the distribution is not available. However, different probability distributions, such as triangular and normal, could be applied in future implementations.

Uncertain parameter	Unit	Type	Base Case	Minimum	Maximum
Matrix permeability	μd	Continuous	49.42	1	50
Fracture conductivity	md-ft	Continuous	500	5	500
Fracture half length	ft	Continuous	92.1	90	400
Fracture height	ft	Continuous	50	20	50

Table 5.2 Predefined ranges for the uncertain parameters

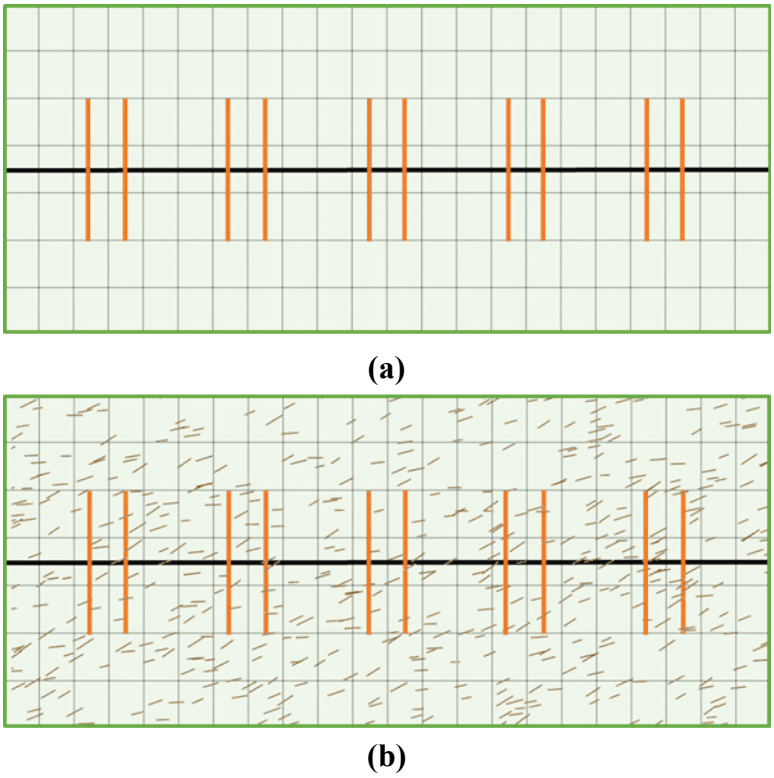

Figure 5.3 Schematic showing a plan view of the two modeling scenarios considered: (a) hydraulic fractures only; and (b) hydraulic and natural fractures. The horizontal well is represented by the solid black line, whereas hydraulic fractures are represented by the perpendicular orange lines. Natural fractures are randomly distributed in the subsurface.

We omit uncertainty for parameters that were previously recognized uncertain, such as initial water saturation, wettability, and effective-fracture count. Based on the findings from Wantawin et al. (2017a) we assume an initial water saturation of 50% and oil-wet rock with the relative permeability curve shown in **Figure 5.4**. Capillary-induced flow-drive forces are trivial here; thus, we do not account for capillary pressure data.

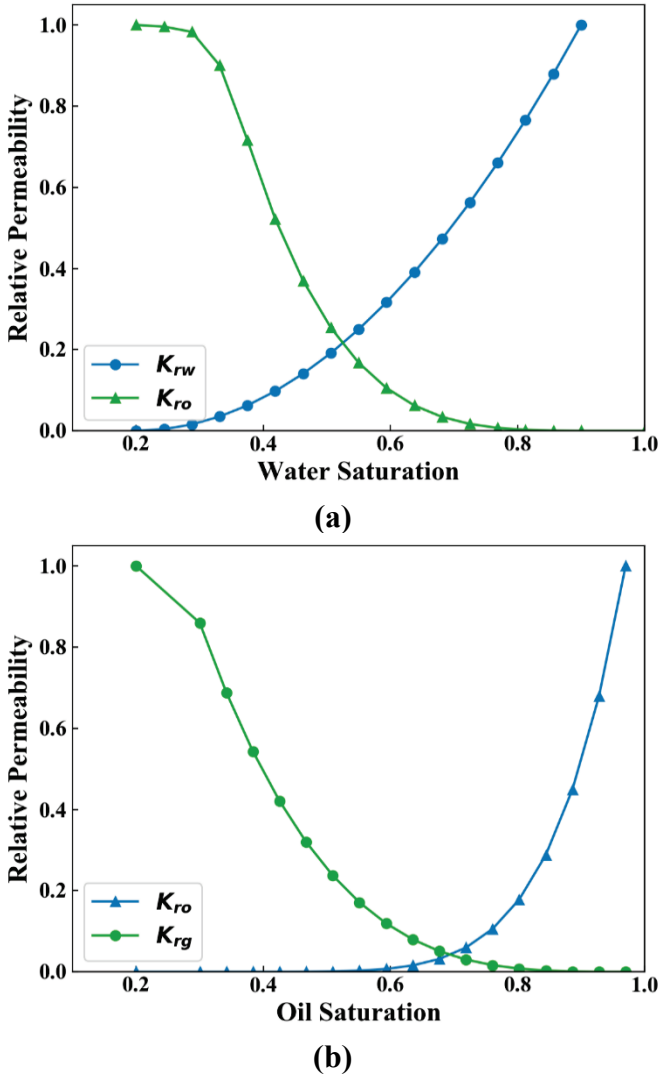

Figure 5.4 Relative permeability curves for the oil-wet rock adopted in the reservoir (from Wantawin et al. 2017a).

In the second scenario, we surround the wellbore with natural fractures. An ensemble of 1000 natural fractures are randomly scattered in the subsurface using the best-match realization, obtained from history matching the first scenario, as a base case. Connections between natural fractures and the well are disabled because the horizontal

lateral is cased and cemented. Natural fractures are created with uniform properties; each natural fracture has 100-ft length, 0.001-ft width, and 3000-md permeability. We assume vertically dipping fractures that cut across the whole reservoir thickness (50 ft).

Varying natural-fracture locations and properties is not considered here because we are interested in the effect of natural-fracture presence on the characterization of induced-fracture network. However, we can address natural-fracture uncertainty in future work once we become confident enough about other subsurface and completion properties.

For each scenario, we are interested in obtaining realizations that satisfy a history-matching criterion; the cases yielding a history-matching error smaller than 5% are accepted as possible solutions. Oil-production data are set as constraints for simulation over the recorded period, and history-matching error is calculated based on the bottom-hole pressure (BHP) and gas-production rate data. Each data type is equally weighted for the purpose of error calculations yielding an objective function we refer to as the global history-matching error. Water-production rates were not reported in the original study and we make the same assumption for water rates to be 25% of oil production rates. For all the AHM studies presented in this chapter, we use the DECE engine.

5.3 RESULTS AND DISCUSSION

Now we present and discuss history-matching and subsequent production forecasting results from all scenarios.

5.3.1 First Scenario – Without Natural Fractures

For the first scenario, after running 500 simulation experiments, the workflow generated 412 realizations qualifying as solutions. Moreover, the global error for the optimal case was 4.15% (**Figure 5.5**). This error is significantly smaller than that for the

base case (5.15%) which is based on previously published history-matching results (Wantawin et al. 2017a) The parameters for the optimal case are: 0.0375 md for matrix permeability; 448 md-ft for hydraulic-fractures conductivities; 155.1 ft for fracture half length; and 35 ft for fracture height.

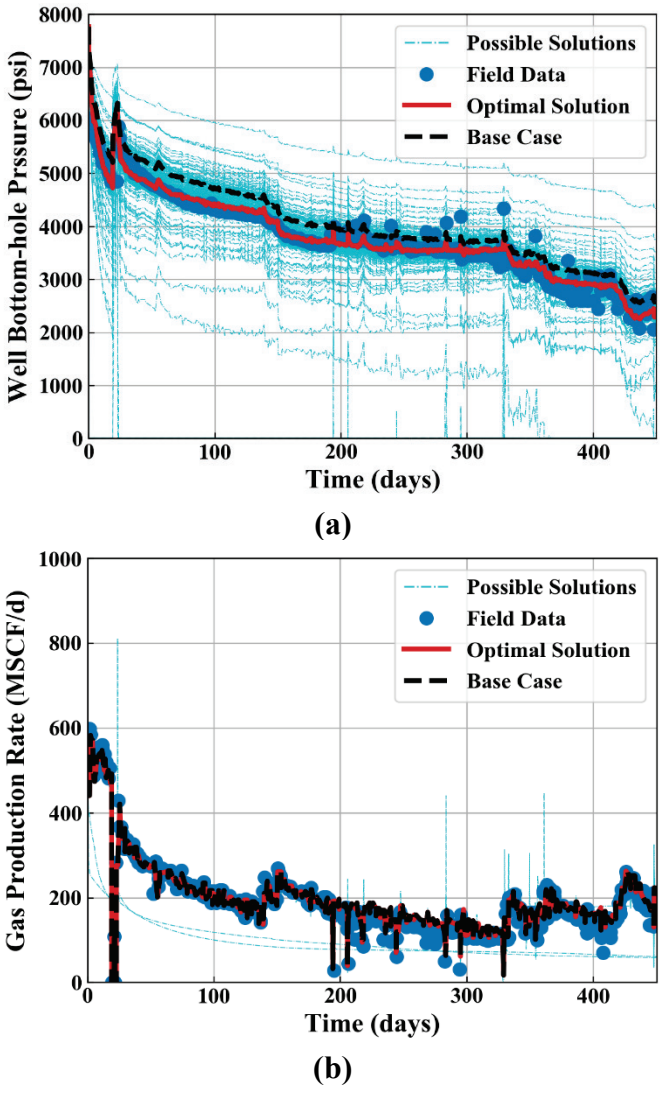

Figure 5.5 History-matching results for scenario 1. (a) BHP response for base case, general solutions and optimal solution; and (b) gas-production-rate responses. Parameters for the base case are listed in **Table 5.2**.

We affiliate this improvement in history-matching quality with the added capability of varying fracture dimensions on a continuous level rather than discrete, which was previously limited by the basic gridblock dimensions of LGR models. This flexibility also

resulted in generating realizations that more closely match our expectations and the reported data for the Middle Bakken (Nojabaei et al. 2013; Cherian et al. 2013).

5.3.2 Second Scenario – With Natural Fractures

Next, we include natural fractures in the optimal solution obtained from the previous step and we repeat history matching. A 3D construction of one subsurface realization is displayed in **Figure 5.6**. In this second scenario, the global error reduced further from 4.94%, for the base case, to 4.12%, for the optimal solution. History-matching results for BHP and cumulative-gas production are shown in **Figure 5.7**. For the optimal realization, matrix permeability decreased to 0.0332 md. Hydraulic-fracture conductivity contracted to 266 md-ft; its half-length slightly increased to 161.5 ft; and its height shrank to 31.5 ft.

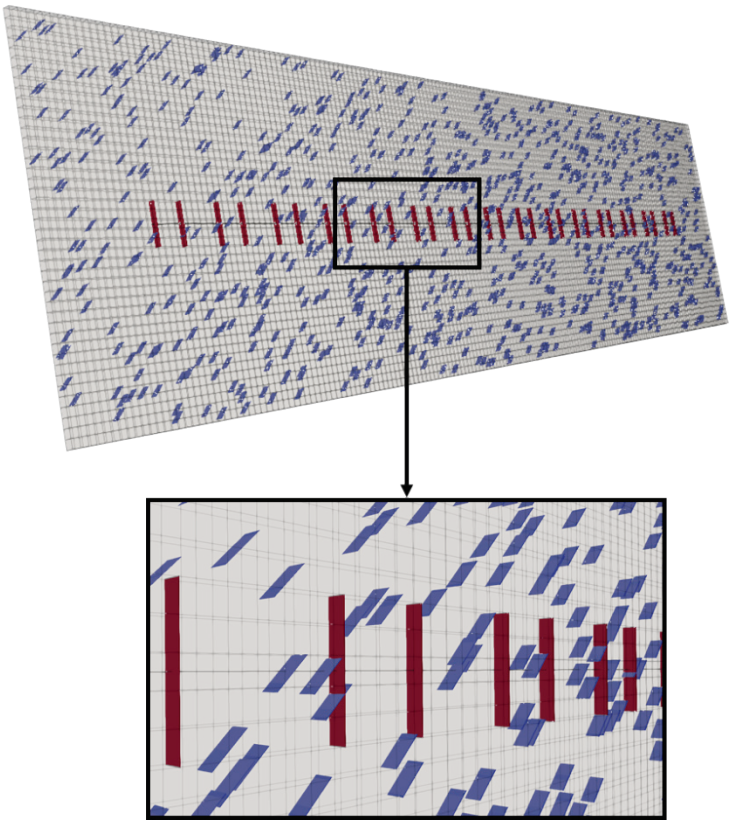

Figure 5.6 3D visualization of the grid for one of the history-matching realizations for the second scenario. Dark red represents EDFM hydraulic fractures, whereas blue represents EDFM natural fractures. Picture is drawn to scale.

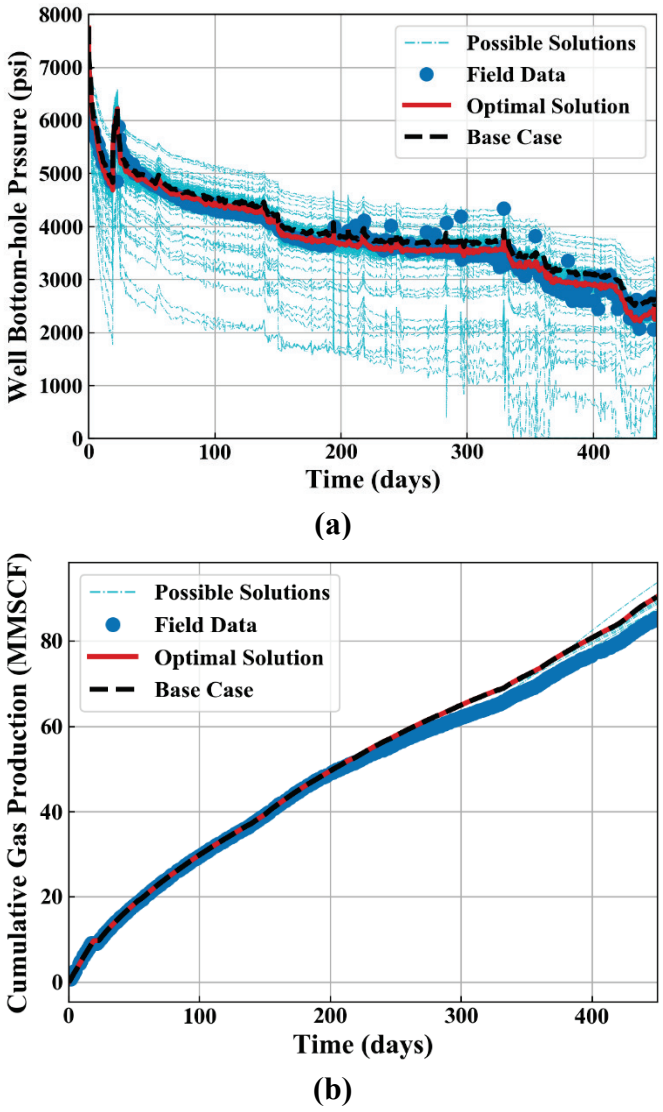

Figure 5.7 History-matching results for scenario 2. (a) BHP response for base case, general solutions and optimal solution; and (b) gas-cumulative-production responses.

5.3.3 Sensitivity Analysis

As demonstrated earlier, this method can be applied for uncertainty and optimization problems beyond history matching. Here, we conduct a simple one-factor-at-a-time (OFAAT) sensitivity study for uncertain parameters on the second scenario. Although we believe that the uncertain parameters are not independent and their combined effects on the objective function are strong and cannot be neglected, an OFAAT analysis still provides valuable insight on single effects (**Figure 5.8**). Results from this analysis are consistent with the findings we will infer from the posterior parameter distributions.

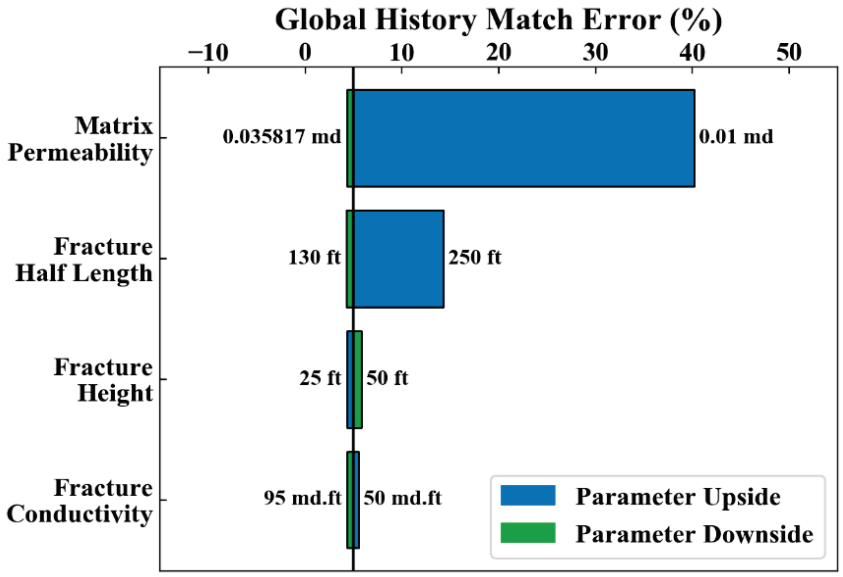

Figure 5.8 OFAAT sensitivity analysis for the second scenario. Ranges for uncertain parameters are the same as **Table 5.2**.

5.3.4 Comparison between the two Scenarios

Figure 5.9 compares the posteriori frequency for uncertain parameters between the two scenarios. After adding natural fractures to the subsurface, matrix-permeability distribution slightly shifts towards decreasing permeability on a logarithmic scale. This observation is consistent with our expectation; natural fractures act as linear-flow pathways from the matrix to the effective wellbore. The presence of natural fractures must be subsidized by decrease in matrix permeability to deliver the same amount of fluid. In addition, the narrow distribution suggests that the history-matching-error response is highly sensitive on matrix permeability; and there is probably distinctive small region of matrix permeability for accepted realizations (here it ranges from 0.0303 to 0.0367 md for the 2nd scenario).

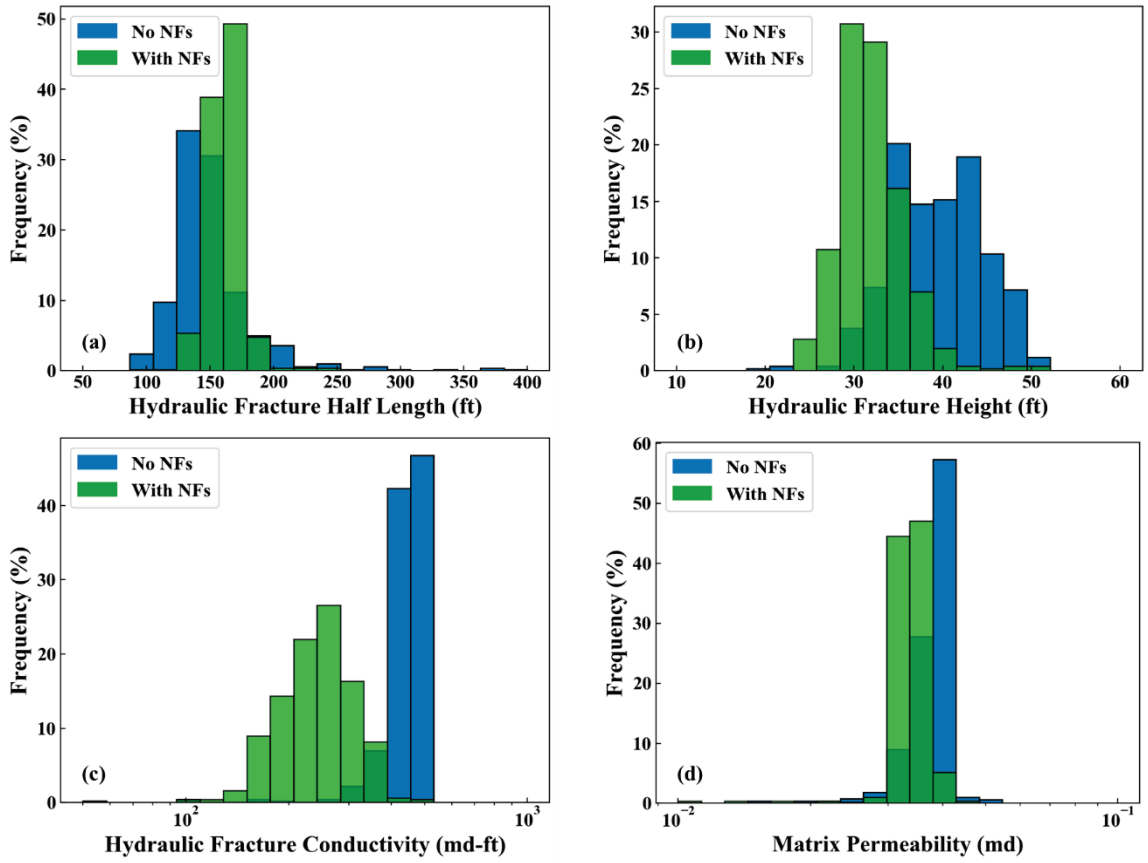

Figure 5.9 Histograms showing the posterior distribution of uncertain parameters. The data are collected from all the general realizations exploited after history matching of the two scenarios.

Conductivity of induced fractures follow the same trend of reduction that counterbalances the natural fractures influence. However, the conductivity distribution has larger dispersion suggesting smaller sensitivity. Here, the fracture conductivity ranges from 149.0 to 387.5 md-ft for accepted realizations. The conductivity distribution exhibits smaller deviation for the second scenario. This can be explained by an argument that the upper bound of uncertainty range might have been initially underestimated (as evident in **Figure 5.9.c**).

Although we expected hydraulic fractures to shrink in length in response to natural fractures, results demonstrate the opposite. Fracture half-length spans from 142.0 to 179.5 ft for accepted realizations. The increase in half-length implies more direct connections between hydraulic and natural fractures (see **Figure 5.6**); and that, perhaps, may be the reason behind the observed lengthening. This lengthening in half-length is offset by a notable decrease in fracture height (as shown in **Figure 5.9.b**). Fracture height's posterior distribution is less uniform in the case of natural fractures, suggesting that it has larger effect to the response when natural fractures are added to the model.

We make a comparison between the grid-pressure responses for the two scenarios (**Figure 5.10**). Notice how the pressure profile becomes non-uniform in the presence of natural fractures. There appears to be regions of increased pressure depletion around natural-fracture clusters. The effect is more noticeable for the natural fractures neighboring the induced fractures. This implies that the distribution of natural fractures in the reservoir is crucial for simulation results.

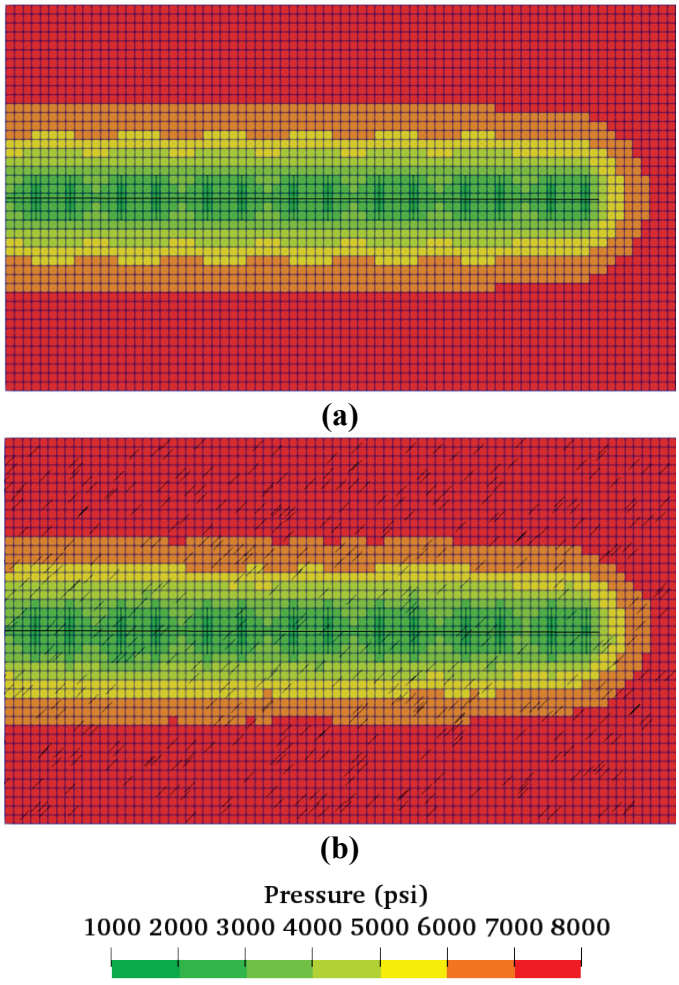

Figure 5.10 Pressure profiles after five months of production for the best-match cases of (a) the first scenario, and (b) the second scenario. Gridblocks $i = 92, \ldots, 170, j = 1, \ldots, 43$ and $k = 1$ are displayed in both figures. The long horizontal line in the middle represents the well and the black lines that intersect with the mesh represent fractures.

5.3.5 Production Forecast

We extend production for the accepted realizations for both scenarios to make future production forecasts and calculate the estimated ultimate recovery (EUR). After history period, production from the well is controlled by constraints of 500-psi minimum BHP and 250 STB maximum oil production rate. Whereas solutions' responses exhibit unnoticeable variation during history period, they undergo significant divergence afterwards (**Figure 5.11**). Calculating cumulative oil production of the well for an assumed, prolonged lifetime of 30 years assesses EUR. P10, P50, and P90 of EUR for the first scenario are 538.06 MSTB, 547.21 MSTB, and 553.44 MSTB, respectively. In this study, we define P10 as the low estimate (i.e., 90% of the estimates are larger than P10).

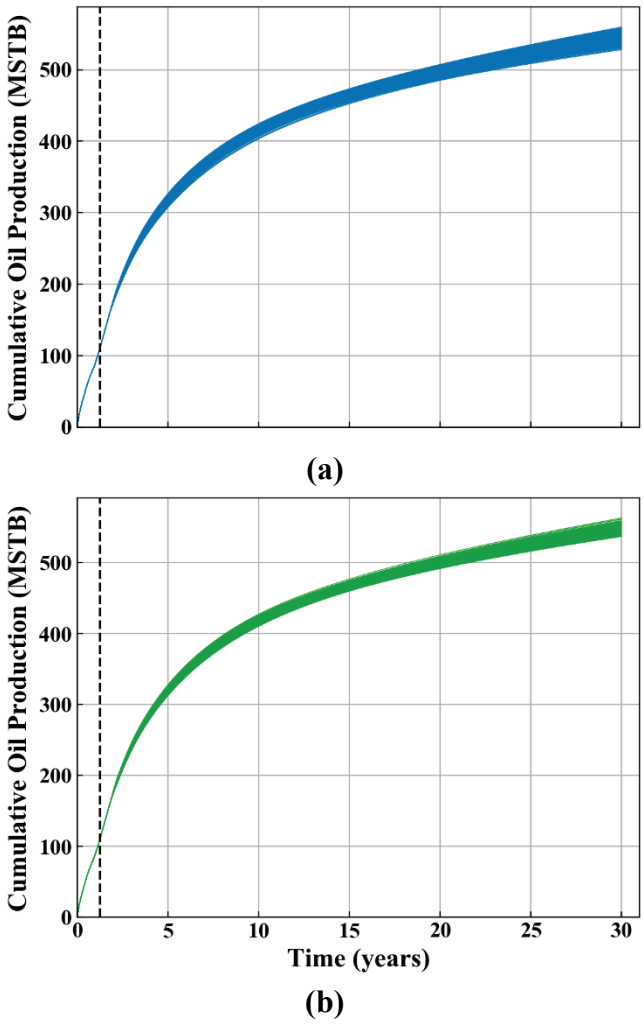

Figure 5.11 Oil cumulative-production forecast for 30 years based on accepted history-matching solutions for: (a) 412 accepted realizations with the first configuration (no natural fractures); and (b) 451 accepted realizations with the second configuration (with natural fractures). The dashed line represents the end of field-recorded period.

The recovery uncertainty band obtained here is more pessimistic than that reported by Wantawin et al. (2017a). This decline in recovery can be explained by the significant

decrease in matrix permeability for the realizations. We report about 15 MSTB variations between the P10 and P90 estimates, whereas the variation was reported to be about 41 MSTB for the previous study. Our method generates more solutions that satisfy the acceptance criterion, but we must be careful about this comparison because the number of uncertain parameters is smaller here.

Li et al. (2011) demonstrated that various configurations could produce the same production history; and that a quality match of production profiles does not guarantee reliable reserve estimation. P10, P50, and P90 of EUR for the second scenario are 541.41 MSTB, 546.78 MSTB, and 553.93 MSTB, respectively. The confidence interval of EUR is slightly wider for the first scenario (**Figure 5.12**). However, the difference between the P50 of the two cases is insignificant (less than 1%). Even though adding natural fractures to the subsurface significantly alters the history-matching realizations (as illustrated earlier), the estimated EUR appears to remain similar.

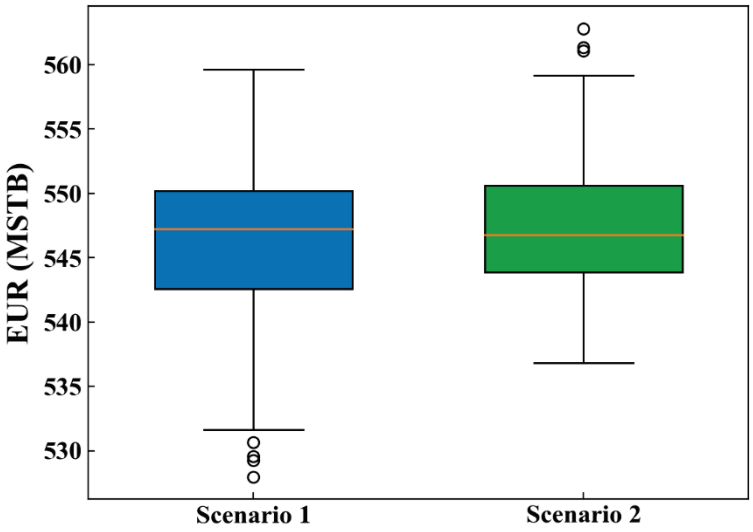

Figure 5.12 Boxplots of the EUR for accepted realizations for the two scenarios.

Although we only take in account cumulative-oil production for EUR estimates, we report similarity between predicted cumulative-gas productions for the two ensembles (**Figure 5.13**). The agreement between prediction outcomes implies that incorporating formation-matrix blocks with an effective permeability leads to similar end results as using detailed description of natural fractures. For the case considered here, we find support that justifies the selection of a simple (effective permeability) model as an analog of the complex-fracture network. However, it will remain for future work to investigate the comparability for different natural-fracture scenarios and reservoir properties.

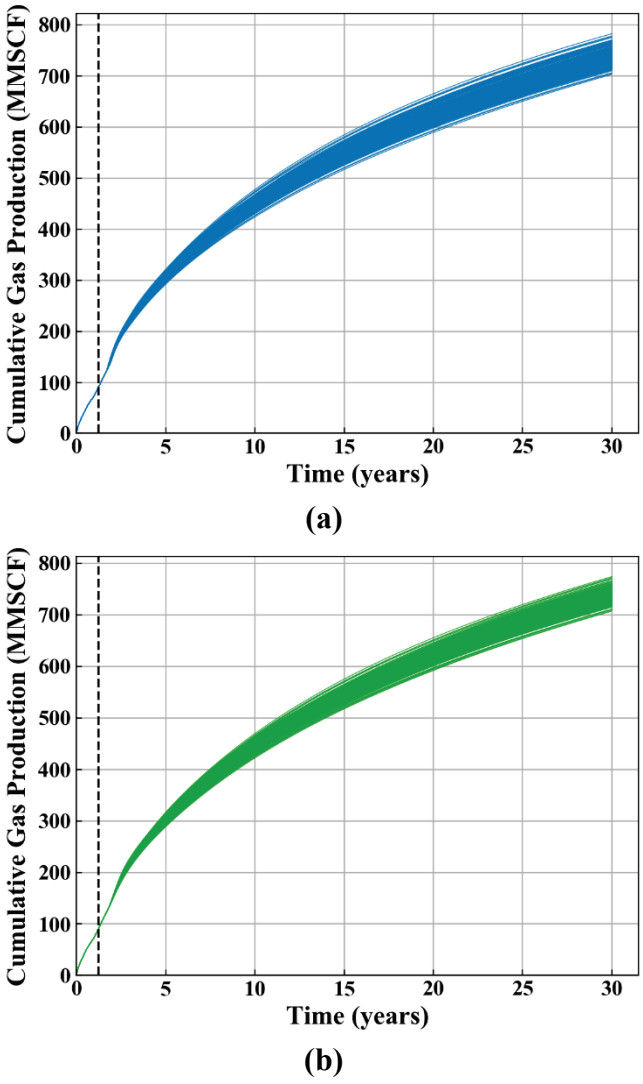

Figure 5.13 Gas cumulative-production forecast for 30 years based on accepted history-matching solutions for: (a) first scenario; and (b) second scenario.

5.3.6 Adding More Natural Fractures

To further test the observations established in the previous section, we consider two additional cases with larger natural fracture intensity. **Figure 5.14**, **Figure 5.15**, **Figure 5.16**, and **Figure 5.17** are 2D plan view of the 4 cases considered showing fractures in blue

segments.

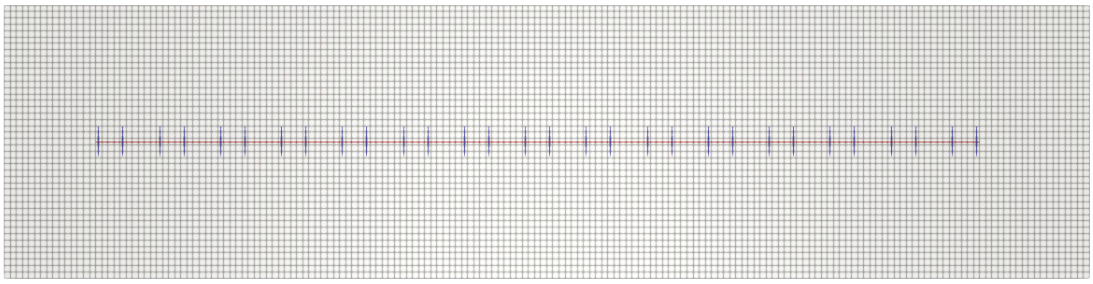

Figure 5.14 Case 1 with no natural fractures

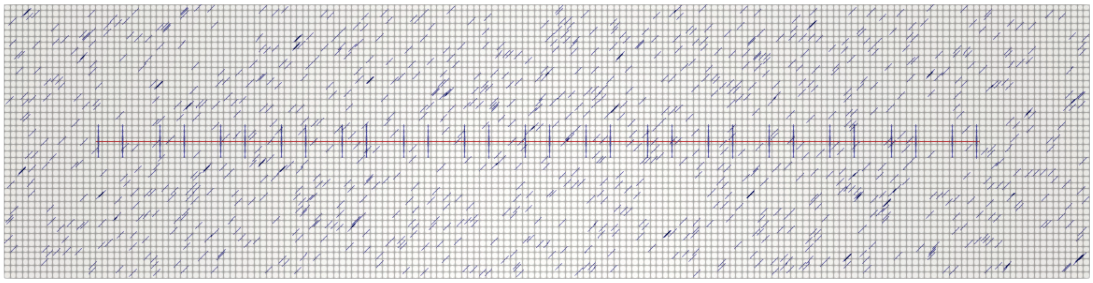

Figure 5.15 Case 2 with 1000 natural fractures

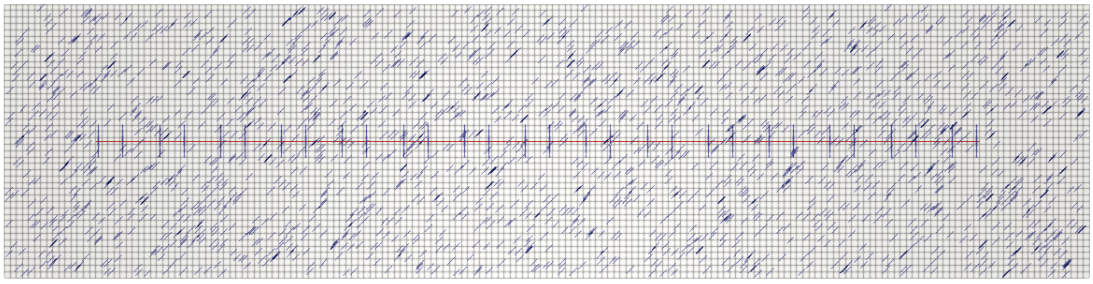

Figure 5.16 Case 3 with 2000 natural fractures

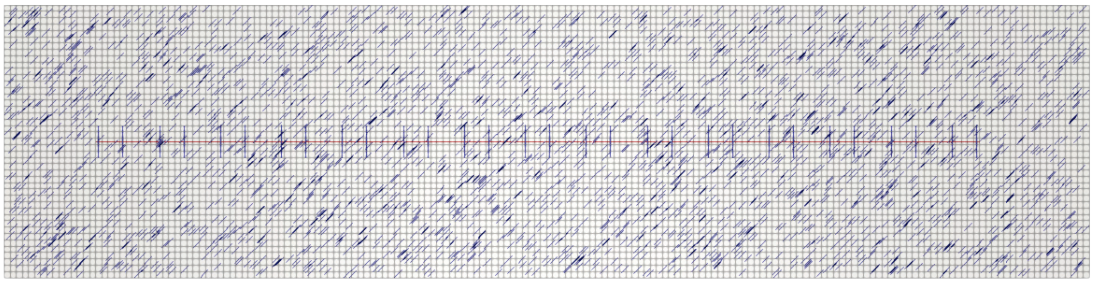

Figure 5.17 Case 4 with 3000 natural fractures

The goal for each case is to achieve history matching and calculate the EUR distribution for the accepted solutions ensemble in the same manner as described earlier in the section. The results are summarized in **Table 5.3**. A comparison-assessment of the EUR among all cases reveals no noteworthy increase in recovered oil with increasing fracture intensity. The comparison is graphically demonstrated in **Figure 5.18**. The distribution has a different variance between the cases, but it seems to be centralized around the same EUR.

Case	**Fracture Density**	**Fracture Intensity**	**EUR (MSTB)**		
	million sq. ft $^{-1}$	**ft / ft^2**	**P10**	**P50**	**P90**
No NFs	0	0	538.1	547.2	553.4
1000 NFs	36	0.0036	541.4	546.8	553.9
2000 NFs	72	0.0072	538.3	550.9	557.1
3000 NFs	108	0.0108	543.8	550.1	557.5

Table 5.3 EUR estimates (P10, P50 and P90) for modeling scenarios with varying fracture density.

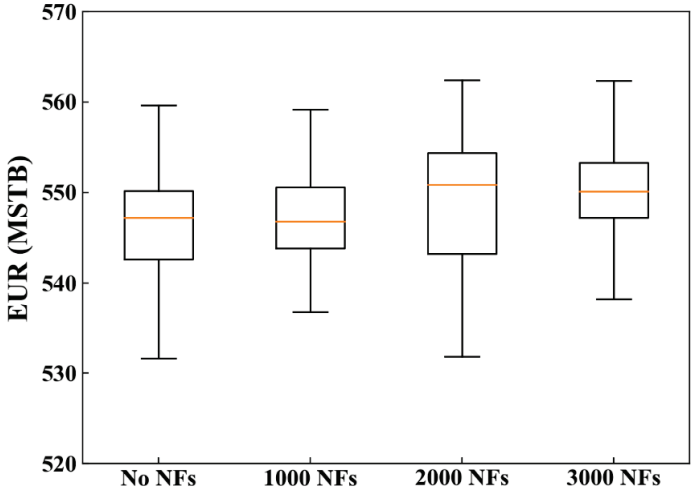

Figure 5.18 Boxplot-presentation of EUR distributions for the four modeling scenarios considered.

An investigation of matrix-permeability posterior distributions, on the other hand, indicates a decreasing shift in posterior permeability as natural-fracture intensity increases (**Figure 5.19**).

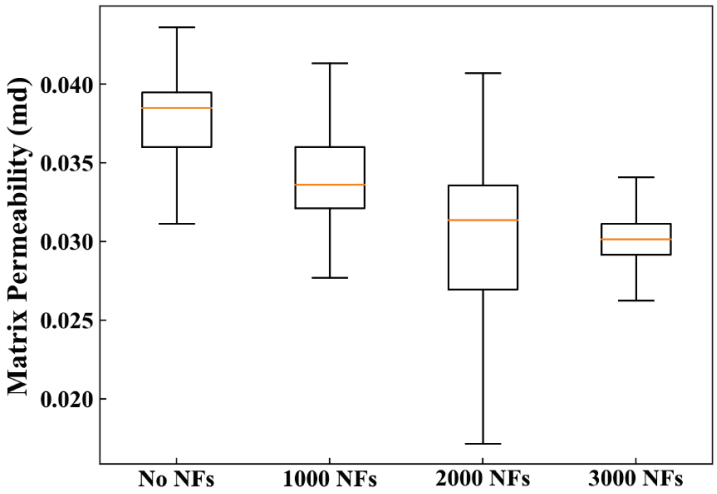

Figure 5.19 Boxplot-presentation of permeability distributions for accepted solutions for the four modeling scenarios considered.

5.4 CONCLUSIONS

In this study, we illustrate the efficiency of our workflow to assist in finding history-matching solutions when uncertainty is large and multi-dimensional. We apply it, however, to the Bakken tight-oil play that has permeability significantly larger than many active shale plays. Further investigation should be focused on applying the workflow on cases from smaller permeability shales and testing the integrity of simple bi-wing planar-fractures models.

We emphasize the importance of AHM methods to address the multi-variable uncertainty that are frequently encountered in unconventional reservoirs. After applying our automated history-matching method to a horizontal well in the Middle Bakken formation, along with taking natural fractures into account, we conclude:

- Integrating EDFM fractures into the automated history-matching workflow adds the advantage of easily adjustable fracture geometry. These new capabilities contribute to reducing the achievable history-matching error and allow for more advanced reservoir characterization.
- Matrix permeability followed by fracture half-length have the most significant effect on the history-matching error. The parameter distribution for accepted realizations have larger dispersion for fracture conductivity and height.
- Adding an EDFM natural-fracture set to the subsurface (in our case) has the following effects on parameters posterior distribution: matrix permeability recedes to smaller values; hydraulic-fracture height and conductivity shrinks; and hydraulic fractures extend to longer half lengths.
- Accepted realizations from the first and second scenarios (with or without natural fractures) bring about roughly the same projected EUR. Therefore, for the case

considered here, effective matrix permeability (that replaces natural fractures) is proven adequate to represent the subsurface.

By applying this method, we retrieve an ensemble of solutions rather than a single solution. Estimation of EUR can be probabilistically assessed from future projections of the retrieved solutions. The method is computationally robust and easily adaptable to different scenarios, and it can be extended to subsequent optimization for unconventional-resources development.

CONCLUSIONS

Chapter 6: Summary and Recommendations for Future Work

In this chapter, we summarize the work in the previous chapters and list key findings and conclusions. Subsequently, we attempt to make recommendations for future research work that takes this work further.

6.1 RESEARCH SUMMARY

The research was focused on tackling uncertainty in unconventional-reservoir models by applying assisted history matching (AHM) methods. We developed a multi-purpose AHM workflow and optimization that borrows available algorithms from a commercial optimization tool. We proposed a new modeling scheme, designed to fit practical field problems, using embedded discrete fracture model (EDFM). The scheme consists of three main zones: formation-matrix blocks, fracture blocks, and stimulated rock volume (SRV) blocks.

One advantage of the method is its capability to handle more than a single well at once. The method enables the individual assignment of parameters to each zone surrounding different wells. Another advantage is that the modeling scheme is designed in a stand-alone form. This flexibility allows us to use various AHM algorithms from a commercial simulation package (as we described in Chapter 4). The stand-alone design also allows for easy integration to other optimization tools and AHM algorithms in the future.

In this study, we applied the method to one synthetic case with the purpose of testing its capabilities and comparing between different available AHM algorithms. We considered two different Bayesian algorithms, a commercial (DECE) algorithm, and two

settings of particle-swarm optimization (PSO) algorithm. The synthetic case consists of two lateral wellbores with EDFM; each has EDFM fractures and SRV volumes surrounding it. Initial fluid-phase saturations and relative permeability curves in the three zones are part of the uncertainty. In addition, we applied the method to a simpler single horizontal well in the middle Bakken. The purpose of this latter study is to assess the effect of explicit description of natural fractures on the uncertainty of production forecasts. Conclusions and key findings from our study can be summarized as follows:

- EDFM creates the advantage of easily adjustable fracture geometry. It also allows for placing natural fractures in arbitrary shapes and orientations. The flexibility in describing fractures allows for broader uncertainty exploitation and more advanced reservoir characterization.
- In the synthetic case, relative permeability curves for solution candidates are non-unique. They can vary from each other and can vary significantly from the truth. For real field-case problems, we shall expect similar non-unique results (see for example **Figure 4.19**).
- Among relative permeability curves, the water curve is the most influential one to the likelihood (data misfit error) in our case, and perhaps shall be given high priority in history-matching studies.
- No significant difference in match quality is spotted when considering three different history-matching time periods (one, two, and three very early production years).
- Bayesian Algorithm I, a method with proxy-based acceptance criteria, is the most efficient. The algorithm produces adequate number of sample solutions at an affordable cost of simulation runs. PSO ranks second in efficiency, followed by the

Metropolis-Hastings MCMC variant, Bayesian Algorithm II. DECE ranks last as it fails to generate any solution candidates (as in **Table 4.8**).

- Bayesian Algorithm II produces the highest-quality posterior distributions for parameters. When compared to Algorithm II results and to the truth, Bayesian Algorithm I tends to be biased towards certain regions of the posterior. PSO evidently fails to correctly sample from the posterior. The distributions obtained from PSO tend to be focused around a very narrow region of the posterior.
- PSO produces significantly underestimates uncertainty range for forecasts. Bayesian Algorithm I produces broader uncertainty range but tends to be pessimistic. Bayesian Algorithm II ranks best for uncertainty quantification as it produces the broadest uncertainty, with the truth lying close to P50 of the predicted range.
- Adding an EDFM natural-fracture set to the middle Bakken case has the following effects on parameters posterior distribution: matrix permeability recedes to smaller values; hydraulic-fracture height and conductivity shrinks; and hydraulic fractures extend to longer half lengths.
- All cases with increasingly varying intensity of natural fractures resulted in comparable EUR ranges. Therefore, for the middle Bakken case considered here, effective matrix permeability is proven adequate enough to represent the subsurface.

6.2 RECOMMENDATIONS

- Most of the AHM samplers considered here are stochastic; they rely on random generators. Therefore, some observations are difficult to assess whether they are systematic or resulting from randomness. Repeating the same experiment multiple

times with different initial seed number may be useful to judge our initial evaluations.

- For the benchmarking study, we fail to obtain an exact posterior because it is currently computationally infeasible. Even though the comparisons presented here are insightful, an exact posterior obtained by traditional MCMC methods would serve as a point of reference for more meaningful comparisons. For an MCMC method to be feasible, the simulation run time must be small enough to run hundred thousands of cases. In the future, simpler models can be used to perform benchmarking studies, where exact posteriors can be obtained.
- In this work, we endorse Bayesian Algorithm I as robust and adequate enough for uncertainty quantification. However, application to other cases might not necessarily have the same robustness or accuracy. Hence, we recommend further testing to additional field scenarios.
- Bayesian Algorithm II seems to be more accurate than Algorithm I but is considerably less efficient. For that reason, we nominate Bayesian Algorithm II for the field problems where running several thousand simulations are affordable. However, research is still required to test the validity of this endorsement to other cases.
- It is clear that Bayesian-inference AHM methods are superior in uncertainty quantification for modest-sized problems (20 parameters). Of a great value is a study that extends the comparison to other Bayesian methods.
- All cases with increasingly varying intensity of natural fractures resulted in comparable EUR ranges. Therefore, for the middle Bakken case considered here, effective matrix permeability is proven adequate enough to represent the subsurface.

- In this thesis, we are convinced that PSO algorithms are inferior, when compared to Bayesian methods. However, we drew conclusions based on only two settings for PSO. Performance might improve (or worsen) if another combination of PSO parameters is used. One interesting topic is the relationship between PSO parameters and its performance.
- In Chapter 5, we drew conclusions based on a tight oil well in the middle Bakken with permeability larger than numerous active shale plays. Validity of these conclusions can be tested on cases with smaller permeability.
- The number of uncertain parameters for the Bakken case study is small (4 parameters). Such a small number might be restricting for uncertainty assessment. Conducting similar experiments under broader uncertainty may be valuable to further test the integrity of simple effective-matrix-permeability models in comparison to the explicit placement of natural fractures.

References

Aanonsen, S.I., Nævdal, G., Oliver, D.S., Reynolds, A.C., and Vallès, B. 2009. The Ensemble Kalman Filter in Reservoir Engineering—A Review. SPE Journal 14 (3): 393–412.

Abrams, A. and Vinegar, H. J. 1985. Impairment Mechanisms in Vicksburg Tight Gas Sands. Paper SPE 13883, presented at the SPE/DOE Permeability Gas Reservoirs, Denver, 19–22 March.

Agrawal, S. and Sharma, M. 2013. Impact of Liquid Loading in Hydraulic Fractures on Well Productivity. Paper SPE 163837, presented at the SPE Hydraulic Fracturing Technology Conference, The Woodlands, Texas, USA, 4–6 February.

Araujo, M., Chen, C., Gao, G., Jennings, J., Ramirez, B., Xu, Z., Yeh, T., Alpak, F.O., and Gelderblom, P. 2019. Benchmarking of Advanced Methods for Assisted History Matching and Uncertainty Quantification. Paper SPE 193910, presented at SPE Reservoir Simulation Conference, Galveston, Texas, USA, 10–11 April.

Bertoncello, A., Wallace, J., Blyton, C., Honarpour, M.M., and Kabir S. 2014. Imbibition and Water Blockage in Unconventional Reservoirs: Well-Management Implications During Flowback and Early Production. SPE Reservoir Evaluation and Engineering 17 (04): 497-506.

Birdsell, D.T., Rajaram H., and Lackey, G. 2015. Imbibition of Hydraulic Fracturing Fluids into Partially Saturated Shale. Water Resources Research 51: 6787–6796.

Bostrom, N., Chertov, M., Pagels, M., Willberg, D., Chertova, A., Davis, M., and Zagorski, W. 2014. The Time-Dependent Permeability Damage Caused by Fracture Fluid. Paper SPE 168140, presented at the SPE International Symposium and Exhibition on Formation Damage Control, Lafayette, Louisiana, USA, 26–28 February.

Carter, J.N., and Ballester, P. 2004. A Real Parameter Genetic Algorithm for Cluster Identification in History Matching. Paper presented at the Proceedings of the 9th European Conference on the Mathematics of Oil Recovery, Cannes, France, 30 August–2 September.

Cheng, Y. 2012. Impact of Water Dynamics in Fractures on the Performance of Hydraulically Fractured Wells in Gas-Shale Reservoirs. Journal of Canadian Petroleum Technology 51 (02): 143–151.

Cherian, B.V, Nichols, C.M., Panjaitan, M.L., Nochols, C.M., and Krishnamurthy, J.K. 2013. Asset Development Drivers in the Bakken and Three Forks. Paper SPE 163855, presented at the SPE Hydraulic Fracturing Technology Conference, The Woodlands, Texas, 4–6 February.

Christie, M., MacBeth, C., and Subbey, S. 2002. Multiple History-Matched Models for Teal South. The Leading Edge 21 (3): 286–289.

Cipolla, C.L., Lolon, E.P., Erdle, J.C., and Rubin, B. 2010. Reservoir Modeling in Shale-Gas Reservoirs. SPE Reservoir Evaluation & Engineering 13 (4): 638–653.

CMG, 2017. CMOST User's Guide, Computer Modeling Group Ltd.

Corey, A.T. 1954. The Interrelation Between Gas and Oil Relative Permeabilities. Producers Monthly 19: 38–41.

Dachanuwattana, S., Xia, Z., Yu, W., Qu, L., Wang, P., Liu, W., Miao, J., and Sepehrnoori, K. 2018a. Application of Proxy-based MCMC and EDFM to History Match a Shale Gas Condensate Well. Journal of Petroleum Science and Engineering 167: 486–497.

Dachanuwattana, S., Jin, J., Zuloaga-Molero, P., Li, X., Xu, Y., Sepehrnoori, K., Yu, W., and Miao, J. 2018b. Application of Proxy-based MCMC and EDFM to History Match a Vaca Muerta Shale Oil Well. Fuel 220: 490–502.

Dachanuwattana, S., Yu, W., and Sepehrnoori, K., 2019. An Efficient MCMC History Matching Workflow Using Fir-For-Purpose Proxies Applied in Unconventional Oil Reservoirs. Journal of Petroleum Science and Engineering 176: 381–395.

Deng, L. and King, M.J. 2018. Theoretical Investigation of Water Blocking in Unconventional Reservoirs Due to Spontaneous Imbibition and Water Adsorption. Paper URTeC 2875353, presented at the SPE/AAPG/SEG Unconventional Resources Technology Conference, Houston, 23–25 July.

Ding, D., 2011. Development of a Data-Partition Technique for Gradient-Based Optimization Methods in History Matching. SPE Journal 16 (3): 582–593.

Ding, Y., Basquet, R., and Bourbiaux, B. 2006. Upscaling Fracture Networks for Simulation of Horizontal Wells Using a Dual-Porosity Reservoir Simulator. SPE Reservoir Evaluation & Engineering 9 (5): 513–520.

Du, C., Zhang, X., Zhan, L., Gu, H., Hay, B., Tushingham, K., and Ma, Y.Z. 2010. Modeling Hydraulic Fracturing Induced Fracture Networks in Shale Gas Reservoirs as a Dual Porosity System. Paper SPE 132180, presented at the CPS/SPE International Oil & Gas Conference and Exhibition, Beijing, China, 8–10 June.

Eltahan, E., Yu, W., Sepehrnoori, K., Kerr, E., Miao, J., and Ambrose, R. 2019. Modeling Naturally and Hydraulically Fractured Reservoirs with Artificial Intelligence and Assisted History Matching Methods Using Physics-Based Simulators. Paper SPE 195269, Presented at SPE Western Regional Meeting, San Jose, California, 23–26 April.

Emerick, A. A., and Reynolds, A. C., 2012. Combining the Ensemble Kalman Filter with Markov-Chain Monte Carlo for Improved History Matching and Uncertainty Characterization. SPE Journal 17 (2): 418–440.

Fan, L., Thompson, J.W., and Robinson, J.R. 2010. Understanding Gas Production Mechanism and Effectiveness of Well Stimulation in the Haynesville Shale through Reservoir Simulation. Paper SPE 136696, presented at the Canadian Unconventional Resources and International Petroleum Conference, Calgary, Alberta, Canada, 19–21 October.

Fiallos Torres, M.X., Yu, W., Ganjdanesh, R., Kerr, E., Sepehrnoori, K., Miao, J., and Ambrose, R. 2019a. Modeling Interwell Fracture Interference and Huff-N-Puff Pressure Containment in Eagle Ford Using EDFM. Paper SPE 195240, presented at SPE Oklahoma City Oil and Gas Symposium, Oklahoma City, Oklahoma, 9–10 April.

Fiallos Torres, M.X., Yu, W., Ganjdanesh, R., Kerr, E., Sepehrnoori, K., Miao, J., and Ambrose, R. 2019b. Modeling Interwell Interference Due to Complex Fracture Hits in Eagle Ford Using EDFM. Paper IPTC 19468, presented at International Petroleum Technology Conference, Beijing, China, 26–28 March.

Gale, J.F., Laubach, S.E., Olson, J.E., Eichhubl, P., and Fall, A. 2014. Natural Fractures in Shale: A Review and New Observations. AAPG Bulletin 98 (11): 2165–2216.

Gao, G., Vink, J.C., Chen, C. et al. 2017. Distributed Gauss-Newton Optimization Method for History Matching Problems with Multiple Best Matches. Computational Geoscience 21: 1325–1342.

Gao, G., Vink, J.C., Chen, C., Araujo, M., Ramirez, B., Jennings, J.W., El Khamra, Y., and Ita, J. 2018. Robust Uncertainty Quantification through Integration of Distributed Gauss-Newton Optimization with Gaussian Mixture Model and Parallelized Sampling

Algorithms. Paper SPE 191516, presented at SPE Annual Technical Conference and Exhibition, Dallas, Texas, USA, 24–26 September.

Gomez, S., Gosselin, O., and Barker, J. W. 2001. Gradient-Based History Matching With a Global Optimization Method. Society of Petroleum Engineers 12 (6): 853–864.

Gong, B., Karimi-Fard, M., and Durlofsky, L.J. 2008. Upscaling Discrete Fracture Characterizations to Dual-Porosity, Dual-Permeability Models for Efficient Simulation of Flow with Strong Gravitational Effects. SPE Journal 13 (1): 58–67.

Hajizadeh, Y., Christie, M., and Demyanov, V. 2009a. Ant Colony Optimisation for History Matching. Paper SPE 121193, presented at the Proceedings of EUROPEC/EAGE Conference and Exhibition, Amsterdam, The Netherlands, 9–11 June.

Hajizadeh, Y., Christie, M., and Demyanov, V. 2009b. Application of Differential Evolution as a New Method for History Matching. Paper SPE 127251, presented at the Proceedings of the Kuwait International Petroleum Engineering Conference and Exhibition, Kuwait, 14–16 December.

Hamdi, H., Behmanesh, H., Clarkson, C.R., and Sousa, M.C. 2015. Using Differential Evolution for Compositional History-Matching of a Tight Gas Condensate Well In the Montney Formation in Western Canada. Journal of Natural Gas Science and Engineering 26: 1317–1331.

Hastings, W.K. 1970. Monte Carlo Sampling Methods Using Markov Chains and Their Applications. Biometrika 57 (1): 97–109.

Hersandi, S. 2013. Modeling of Water Behavior in Hydraulically-Fractured Shale Gas Wells. MS Thesis, Norwegian University of Science and Technology, Trondheim, Norway (July, 2013).

Jones, S.C. 1997. A Technique for Faster Pulse-Decay Permeability Measurements in Tight Rocks. SPE Formation Evaluation 12 (1): 19–25.

Kazemi, H., Merrill, L.S., Porterfield, K.L., and Zeman, P.R. 1976. Numerical Simulation of Water-Oil Flow in Naturally Fractured Reservoirs. SPE Journal 16 (6): 317–326.

Kennedy, J., and Eberhart, R. 1995. Particle Swarm Optimization. Proceedings of IEEE International Conference on Neural Networks 4: 1942–1948.

Khoshghadam, M., Khanal, A. and Lee, W.J. 2015. Impact of Fluid, Rock and Hydraulic Fracture Properties on Reservoir Performance in Liquid-Rich Shale Oil Reservoirs. Paper URTeC 2154207, presented at the SPE/AAPG/SEG Unconventional Resources Technology Conference, San Antonio, Texas, USA, 20–22 July.

Lake, L.W., Johns, R.T., Pope, G.A. et al. 2014. Fundamentals of Enhanced Oil Recovery. Richardson, Texas, USA: Society of Petroleum Engineers.

Li, J., Du, C., and Zhang, X. 2011. Critical Evaluation of Shale Gas Reservoir Simulation Approaches: Single-Porosity and Dual-Porosity Modeling. Paper SPE 141756, presented at the SPE Middle East Unconventional Gas Conference and Exhibition, San Antonio, Texas, 31 January–2 February.

Longoria, R.A., Liang, T., Huynh, U.T., Nguyen, Q.P., and DiCarlo D.A. 2017. Water Blocks in Tight Formations: The Role of Matrix/Fracture Interaction in Hydrocarbon-Permeability Reduction and Its Implications in the Use of Enhanced Oil Recovery Techniques. *SPE Journal* 22 (5): 1393–1401.

Luo, S., Wolff, M., Ciosek, J., Rasdi, M.F., Neal, L., Arulampalam, P., and Willis, S.K. 2011. Probabilistic Reservoir Simulation Workflow for Unconventional Resource Play: Bakken Case Study. Paper SPE 142896, presented at the SPE EUROPEC/EAGE Annual Conference and Exhibition, Vienna, Austria, 23–26 May.

Ma, X., Al-Harbi, M., Datta-Gupta, A., and Efendiev, Y. 2008. An Efficient Two-Stage Sampling Method for Uncertainty Quantification in History Matching Geological Models. SPE Journal 13 (10): 77–87.

Martineau, D.F. 2007. History of the Newark East Field and the Barnett Shale as a Gas Reservoir. AAPG Bulletin 91 (4): 399–403.

Mattar, L., Gault, B., Morad, K. et al. 2008. Production Analysis and Forecasting of Shale Gas Reservoirs: Case History-Based Approach. Paper SPE 119897, presented at the SPE Shale Gas Production Conference, Fort Worth, Texas, USA, 16–18 November.

Metropolis, N., Rosenbluth, A.W., Rosenbluth, M.N., Teller, A.H., and Teller, E. 1953. Equation of State Calculations by Fast Computing Machines. The Journal of Chemical Physics 21 (6): 1087–1092.

Mohamed, L., Christie, M.A., and Demyanov, V. 2010. Reservoir Model History Matching with Particle Swarms: Variants Study. Paper SPE 129152, presented at SPE Oil and Gas India Conference and Exhibition, Mumbai, India, 20–22 January.

Moinfar, A., Narr, W., Hui, M.H., Mallison, B.T., and Lee, S.H. 2011. Comparison of Discrete-Fracture and Dual-Permeability Models for Multiphase Flow in Naturally Fractured Reservoirs. Paper SPE 142295, presented at the SPE Reservoir Simulation Symposium, The Woodlands, Texas, USA, 21–23 February.

Moinfar, A., Varavei, A., Sepehrnoori, K., and Johns, R. 2014. Development of an Efficient Embedded Discrete Fracture Model for 3D Compositional Reservoir Simulation in Fractured Reservoirs. SPE Journal 19 (2): 289–303.

Mokhtari, M., Alqahtani, A.A., Tutuncu, A.N., and Yin, X. 2013. Stress-Dependent Permeability Anisotropy and Wettability of Shale Resources. Paper URTeC 1555068, presented at SPE/AAPG/SEG Unconventional Resources Technology Conference,

Denver, Colorado, USA, 12–14 August.

Nojabaei, B., Jhons R.T., and Chu, L. 2013. Effect of Capillary Pressure on Phase Behavior in Tight Rocks and Shales. SPE Reservoir Evaluation & Engineering 16 (3): 281-289.

Oliver, D. and Chen, Y. 2011. Recent Progress on Reservoir History Matching: A Review. Computational Geoscience 15 (1): 185–221.

Oliver, D.S. 1996. Multiple Realization of the Permeability Field from Well-Test Data. SPE Journal 1(2): 145–155.

Parmar, J.S., Dehghanpour, H., and Kuru, E. 2014. Displacement of Water by Gas in Propped Fractures: Combined Effects of Gravity, Surface Tension, and Wettability. Journal of Unconventional Oil and Gas Resources 5: 10–21.

Ramirez, B.A., Gelderblom, P.P., Eales, A.D., Chen, X., Hobson, M.P., and Esler, K. 2017. Sampling From the Posterior in Reservoir Simulation. Paper SPE 188892 Presented at Abu Dhabi International Petroleum Exhibition & Conference, Abu Dhabi, UAE, 13–16 November.

Rapoport, L.A. and Leas, W.J. 1953. Properties of Linear Waterfloods. Journal of Petroleum Technology 5 (5): 139–148.

Razavi, F., and Jalali-Farahani, F. 2008. Ant Colony Optimisation: A Leading Algorithm in Future Optimisation of Petroleum Engineering Processes. Springer 5097: 469–478.

Ripley, B.D. 1987. Stochastic Simulation. New York: Wiley Series in Probability and Mathematical Statistics. John Wiley & Sons.

Romero, C.E., Carter, J.N., Gringarten, A.C., and Zimmerman, R.W. 2000. A Modified Genetic Algorithm for Reservoir Characterisation. Paper SPE 64765, presented at

International Oil and Gas Conference and Exhibition in China, Beijing, China, 7–10 November.

Rossen, R.H. 1977. Simulation of Naturally Fractured Reservoirs with Semi-Implicit Source Terms. SPE Journal 17 (3): 201–210.

Shakiba, M., de Araujo Cavalcante Filho, J.S., and Sepehrnoori, K. 2018. Using Embedded Discrete Fracture Model (EDFM) in Numerical Simulation of Complex Hydraulic Fracture Networks Calibrated by Microseismic Monitoring Data. Journal of Natural Gas Science and Engineering 55: 495–507.

Skilling J. 2004. Nested Sampling. AIP Conference Proceedings 735: 395–405.

Slotte, P.A., and Smorgrav, E. 2008. Response Surface Methodology Approach for History Matching and Uncertainty Assessment of Reservoir Simulation Models. Paper SPE 113390, presented at Europec/EAGE Conference and Exhibition, Rome, Italy, 9–12 June.

Stordal, A.S., and Nævdal, G. 2018. A Modified Randomized Maximum Likelihood for Improved Bayesian History Matching. Computational Geosciences 22 (29): 29–41.

Subbey, S., Christie, M., and Sambridge, M. 2004. Prediction under Uncertainty in Reservoir Modeling. Journal of Petroleum Science and Engineering 44 (1-2): 143–153.

Sun, H., Chawathe, A., Hoteit, H., Shi, X., and Li, L. 2015. Understanding Shale Gas Flow Behavior Using Numerical Simulation. SPE Journal 20 (1): 142–154.

Tarantola, A. 2005. Inverse Problem Theory and Methods for Model Parameter Estimation; Publisher: Society for Industrial and Applied Mathematics, Philadelphia, PA, USA. ISBN: 978-0-89871-572-5.

Tavassoli, Z., Carter, J.N., and King, P.R. 2004. Errors in History Matching. Society of Petroleum Engineers 9 (3): 352–361.

Trelea, R.C. 2013. The Particle Swarm Optimization Algorithm: Convergence Analysis and Parameter Selection. Information Processing Letters 85 (6): 317–325.

Tripoppoom, S., Yu, W., Huang, H., Sepehrnoori, K., Song, W., Dachanuwattana, S. 2019. A Practical and Efficient Iterative History Matching Workflow for Shale Gas Well Coupling Multiple Objective Functions, Multiple Proxy-based MCMC and EDFM. Journal of Petroleum Science and Engineering 176: 594–611.

Vazquez, O., Young, C., Demyanov, V., Arnold, D., Fisher, A., MacMillan, A., and Christie, M., 2015. Produced-Water-Chemistry History Matching in the Janice Field. SPE Reservoir Evaluation & Engineering 18 (4): 564–576.

Wantawin, M., Yu, W., and Sepehrnoori, K. 2017a. An Iterative Work Flow for History Matching by Use of Design of Experiment, Response-Surface Methodology, and Markov Chain Monte Carlo Algorithm Applied to Tight Oil Reservoirs. SPE Reservoir Evaluation & Engineering 20 (3): 613–626.

Wantawin, M., Yu, W., Dachanuwattana, S., and Sepehrnoori, K. 2017b. An Iterative Response-Surface Methodology by Use of High-Degree-Polynomial Proxy Models for Integrated History Matching and Probabilistic Forecasting Applied to Shale-Gas Reservoirs. SPE Journal 22 (6): 2012–2031.

Xu, J., and Sonnenberg, S. 2016. Brittleness and Rock Strength of the Bakken Formation, Williston Basin, North Dakota. Paper URTeC 2460490, presented at the SPE/AAPG/SEG Unconventional Resources Technology Conference Unconventional Resources Technology Conference, San Antonio, Texas, USA, 1–3 August.

Xu, Y., Cavalcante Filho, J.S.A., Yu, W., and Sepehrnoori, K. 2017a. Discrete-Fracture Modeling of Complex Hydraulic-Fracture Geometries in Reservoir Simulators. SPE Reservoir Evaluation & Engineering 20 (2): 403–422.

Xu, Y., Yu, W., and Sepehrnoori, K. 2017b. Modeling Dynamic Behaviors of Complex Fractures in Conventional Reservoir Simulators. Paper URTeC 2670513, presented at the SPE/AAPG/SEG Unconventional Resources Technology Conference, Austin, Texas, 24–26 July.

Xu, Y., Yu, W., Li, N., Lolon, E., and Sepehrnoori, K. 2018. Modeling Well Performance in Piceance Basin Niobrara Formation Using Embedded Discrete Fracture Model. Paper URTeC 2901327, presented at the SPE/AAPG/SEG Unconventional Resources Technology Conference, Houston, Texas, 23–25 July.

Yang, C., Nghiem, L., Erdle, J., Moinfar, A., Fedutenko, E., Li, H., Mirzabozorg, A., and Card, C. 2015. An Efficient and Practical Workflow for Probabilistic Forecasting of Brown Fields Constrained by Historical Data. Paper SPE 175122, presented at SPE Annual Technical Conference and Exhibition, Houston, Texas, USA, 28–30 September.

Yang, D., Xue, X., and Chen, J. 2018. High Resolution Hydraulic Fracture Network Modeling Using Flexible Dual Porosity Dual Permeability Framework. Paper SPE 190096, presented at the SPE Western Regional Meeting, Garden Grove, California, 22–26 April.

Yu, W., and Sepehrnoori, K. 2018. Shale Gas and Tight Oil Reservoir Simulation, 1st Ed.; Publisher: Elsevier, Cambridge, USA. ISBN: 978-0-12-813868-7.

Yu, W., Tripoppoom, S., Sepehrnoori, K., and Miao, J. 2018. An Automatic History-Matching Workflow for Unconventional Reservoirs Coupling MCMC and Non-

Intrusive EDFM Methods. Paper SPE 191473, presented at the SPE Annual Technical Conference and Exhibition, Dallas, Texas, 24–26 September.

Yu, W., Zhang, Y., Varavei, A., Sepehrnoori, K., Zhang, T., Wu, K., and Miao, J. 2019. Compositional Simulation of CO2 Huff-n-Puff in Eagle Ford Tight Oil Reservoirs with CO2 Molecular Diffusion, Nanopore Confinement and Complex Natural Fractures. SPE Reservoir Evaluation & Engineering, in preprint.